STUDY OF HADRONIC JETS

PRODUCED BY

CHARGED PION AND PROTON BEAMS

INCIDENT ON

HYDROGEN AND ALUMINUM TARGETS

Thesis by

翁嘉朱

Kar Woo Yung

In Partial Fulfillment of the Requirements

for the Degree of

Doctor of Philosophy

California Institute of Technology

Pasadena, California

1980

(submitted September 19, 1979)

ACKNOWLEDGEMENTS

"Love and respect your parents is the beginning of all good doings" (百善孝為先) . I am only a bud on a small branch of an ever lasting tree.

My dear sister, Jar Fee (嘉翡), always appears in my crises. She sends me cards of Valentines even after her marriage to Prof. Chung of Northwestern University.

"Behind every successful man, there is always a woman". Dai Li (黛麗), or "Beauty of the spotless jade that shines with the soft brightness of Violets", is my Love. Her tenderness, her encouragements, and her typing assistances, are essential for the completion of this thesis. We will be married this summer.

I would like to express my graditudes and best wishes to all my collaborators, and all the personnel involved in experiment E-260. Special thanks to

"When you walk along with two others, you always learn something" (三人行，必有我師焉．）. I learn a lot from all the people that surround me.

Frank Nagy always helps me in some of my computer programmings. He is as efficient as the Tracter Beam and as logical as Mr. Spock. The FORCE is with him.

The nice thing about Caltech, at least in my case, is that "you learn so much while it pays all the fees". I WALK by all the OLIVE trees. This is my home away from the home.

The westerner regards his teacher as a supervisor, an adviser and a friend. In China, the teacher, or sometimes called as the Master, is respected as much as the parents. Parents give you life while

the teacher teaches you how to live. "If a person is not educated, It is the father's fault. If the teaching is not strict and severe, it is the laziness of the teacher" (養不教 ， 父之過 ； 教不嚴 ， 師之惰). On the other hand "when the teacher is in need, the student should serve and help his teacher to solve all the problems" (有事 ， 弟子服其勞).

Jon Mathews is my Caltech undergraduate advisor. He is a good physicist and he is probably one of the best lecturer that I ever had. We had a good time playing GO together.

Sometimes, the student reflects the teacher like a mirror. Both Geoffrey and I smile a lot. We like hats and recently we both wear dark glasses. Throughout these years, I have learnt Grossly Consistently Far more than expected from Geoffrey.

Professor G.C.Fox, who supervises me on this thesis, is my very respected Master-teacher and my very dear friend.

♡ ·······To Kathy

黛霓 ········♡

ABSTRACT

High transverse momentum ($p_\perp$) particles are
thought to reflect the underlying parton (quark or
gluon) mechanisms of hadron interactions. A
particularly simple model by Feynman, Field and Fox
(or FFF), involves hard scattering of a pair of
partons via gluon exchange (Quantum Chromodynamics
or QCD) with subsequent fragmentation of the partons
into hadrons.

We present results from an experiment (E260 at
Fermilab) on the production of jets (groups of
particles) and single charged particles, at both low
and high $p_\perp$, in 200 Gev interactions. The
experiment used a calorimeter triggered
multiparticle spectrometer. Results are presented
on the comparisons of cross sections and associated
charged particle distributions for pion and proton
beams and aluminium and hydrogen targets.

Our high $p_\perp$ proton data agree with the FFF

predictions in most cases.   However, there are signs of discrepancies.

    We define α by the equation :

$A_{AL}^{\alpha} = \sigma_{AL} / \sigma_{HY}$ where A_{AL} is the atomic weight of aluminium and σ_{AL} and σ_{HY} are cross sections for the aluminium and hydrogen targets.   The proton beam data show larger nuclear anomalies (in particular, $\alpha > 1$) than the pion beam data.   There is essentially no difference between π^+ and π^- beams.

    We compare the associated charged particle distributions for the two targets.   The observed difference between these two targets could be related to the propagation and secondary scattering of partons in the nuclear matter;   interpreting our data in this framework, we find that any secondary scattering must be coherent with the main interaction.

    E260 is the first experiment to study both high and low $p_\perp$ interactions off nuclear targets with detailed measurements of the event structure.   This is essential for understanding both nuclear effects and QCD in high energy interactions.

TABLE OF CONTENTS

LIST OF TABLES

LIST OF FIGURES

CHAPTER I

INTRODUCTION

1.1 OVERVIEW

During recent years, deep inelastic lepton-nucleon scattering has been most successfully interpreted by parton models [1.1] (see Fig. 1.1a), where it is assumed that the underlying process is the scattering of the incident leptons on constituents of the nucleon. It is supposed, in such models, that these elementary point-like constituents or "partons" are very strongly bound inside the nucleon. Nevertheless, for high energy-momentum transfers, large compared with the nucleon mass, an individual parton can be regarded as effectively independent of the rest.

This physical picture has led to the prediction [1.2], verified by experiment [1.3], that in hadron-hadron interactions (see Fig. 1.2), particles with high transverse momentum ($p_\perp$) should be produced with much higher cross section than

expected from extrapolation of the low $p_\perp$ behaviour.

Further support for this picture has been provided by the observation [1.4] of jet-structure in hadronic events from e^+e^- annihilation (Fig. 1.1b), which can be interpreted as the manifestation of the production of parton pairs and their subsequent decay into hadrons (fragmentation). A similar structure is expected to be present in events in which a high $p_\perp$ particle is produced in hadron-hadron interactions. However, in contrast with the lepton initiated reactions, it is only in the latter type of process that the effect of direct parton-parton scattering can be observed. Ultimately, this opens the possibility of inferring the properties of parton-parton interactions from the study of hadron collisions producing high $p_\perp$ particles or jets.

Experimentally, jets appear as clusters of particles going approximately in the direction of the original partons. The mean transverse momentum of particles in the jet with respect to the parton momentum vector is expected to be around 350 Mev/c.

Attempts have been made to analyse all the experimental results on the production of high $p_\perp$ particles or jets in terms of the presently existing Quantum Chromodynamic Field Theory [1.5]. In such a theoretical framework, partons are quarks and gluons. Hard scattering among these partons is believed to be dominated by gluon exchange processes. The gluon, which is the field carrier of the strong interaction (also called the color field), is very analogous to the photon in the electromagnetic interaction (see Fig. 1.2b), except it can also interact with itself. Of course the gluon quark coupling is much larger than that of the photon to quarks.

In a particular QCD model discussed by Feynman, Field and Fox (or FFF) [1.6], it is supposed that the high $p_\perp$ jet production in hadron-hadron collision is due to hard scattering between partons, one from the beam and the other from the target, via gluon exchange. The resulting scattered partons and the unaffected parts of the colliding particles are assumed to fragment into jets of hadrons. This gives rise to a four-jet structure in high $p_\perp$ hadron-hadron collision (Figure 1.2c).

The purpose of our experiment is to investigate these phenomena in hadron-hadron collision at an incident momentum of 200 Gev/c. Hopefully, our experimental results may lead to a better understanding of quarks, gluons and QCD.

1.2 THE EXPERIMENT

The experiment described by this thesis is the Fermilab Multiparticle Spectrometer experiment E260. It is a Caltech-UCLA-FNAL-UICC-Indiana collaboration. The experiment was triggered by two calorimeters which allowed us to select events containing either a single particle at high $p_\perp$ or a group of particles (jet) which together sum up to give large $p_\perp$. In both triggers, we were able to study the properties of the associated charged particles over a wide kinematic range as the spectrometer had essentially full azimuthal acceptance for the range $0° < \theta_{c.m.} < 90°$.

The experiment was performed in the M6W beamline at Fermilab with a beam energy of 200 Gev and different species (π, K, p) of beam particle

tagged by four beam Cerenkov counters.

Some initial data were taken with a beryllium target in December 1975 and January 1976. The main run was in June through September 1976. Results of the test run and part of the main run have been published [1.7]. This thesis concentrates on the discussion of the data from the main run, sketching some results from the test run whenever it is necessary. The methods and procedures described here are those used on the main run unless specified otherwise. Some of the results presented here will be published [1.8]. Further discussion of our experiment can be found in other theses [1.9].

1.3 MOTIVATION FOR OUR MEASUREMENTS

There are two major classes of measurements in our experiment:

A.   The production cross sections for :

$$bA \longrightarrow h^{\pm} X \qquad\qquad (1.1)$$

$$bA \longrightarrow Jet\ X \qquad\qquad (1.2)$$

where we observe either a single charged hadron

$h^{\pm}$ or a group of particles (jet) at high $p_{\perp}$. Here the beam $b = p, \pi^+$ or π^- has a momentum of 200 or 190 Gev/c and the target A = hydrogen or aluminium.

B.   Correlations and characteristics of the associated charged particles in regions of phase space allowed by the experiment.

Interest in the measurement of high $p_{\perp}$ production cross sections stemmed from early ISR results [1.10]. These experiments showed a much larger yield of hadrons at high $p_{\perp}$ than expected from a naive $\exp(-6p_{\perp})$ extrapolation of the low $p_{\perp}$ data. This yield also increased with energy at fixed $p_{\perp}$. These single high $p_{\perp}$ particle cross sections can be parametrized by the scaling law:

$$E\ d^3\sigma/d^3p = f(x_{\perp})\ p_{\perp}^{-N} \qquad (1.3)$$

where $(E\ d^3\sigma/d^3p)$ is the invariant cross section and $x_{\perp} = 2p_{\perp}/\sqrt{s}$.

For a proton beam and a pion final state, the observed $p_{\perp}^{-1}$ power N is approximately 8. This was in fact predicted by the CIM model (Constituent Interchange Model) where the typical scattering is $\pi q \rightarrow \pi q$ and the π is a "constituent" of the proton. However the simple CIM model, without

substantial modifications, also predicts jet
production at about the same cross section as for
single particles. Our earlier analysis (mainly by
Fox) clearly indicates [1.7] that the jet cross
section is at least five hundred times that for a
single hadron. This suggests that our jet trigger
is probably directly observing the quarks and gluons
predicted naturally by QCD. Although the Born
scattering graphs of QCD give the incorrect
prediction of a $p_\perp^{-4}$ behavior for the cross section,
there are many corrections to this in a realistic
calculation. An analysis of QCD by Field [1.5],
which includes all the effects which are currently
known, suggests QCD is capable of describing all
presently existing high $p_\perp$ single hadron and jet
measurements. Our new results on the jet cross
section can be used for further comparison with the
QCD predictions.

The event structure is an important extra
constraint for theoretical models of high
$p_\perp$ processes. For instance, the original
Constituent Interchange Model [1.11] which fitted
the single particle cross section data well, failed
completely for both the event structure and cross

section for the jet events [1.7]. Studies of
associated multiplicity and correlations are hence
essential for understanding such rare (the high
$p_\perp$ cross section is very small) processes. Our
experiment enables us to study the associated
charged particles in the following three regions
which correspond approximately to those populated by
three out of the four jets shown in Fig. 1.2c :

A.   The Trigger Side

     This mainly includes those particles associated
directly with the trigger jet. If QCD is correct,
the distribution of momenta for charged particles
making up the jet cluster in hadron scattering
should be similar to the analogous distribution in
lepton process. This momentum distribution for
particles in the jet is usually called the
fragmentation function. The quantum number
distributions of particles on the trigger side
should also reflect the flavour of the original
triggered parton.

B.   The Away Side

     This includes particles opposite to the trigger
jet. Theoretically we expect a jet here which is

directly opposite to the trigger jet in the center
of mass frame of the colliding partons after the
deep elastic scattering. In practice, it is hard
experimentally to determine this parton center of
mass frame on the event by event basis as it does
not coincide with the beam target center-of-mass
frame. It is more convenient to understand the away
side "jet" in a statistical sense. There is
evidence for clustering of particles (or a "fan"
structure) on the away side for the case of single
high $p_\perp$ triggers [1.10]. Our experiment enables us
to make similar studies for the jet trigger, and
compare results with different incoming beam types.
Our earlier analysis [1.7] has already shown that
the jet away side is very similar to the single
particle away side, indicating that comparable
dynamics were probably behind both triggers. Please
refer to our previous publications for more details.

C.   The Forward Region

In this region, we expect to see fragments of
whatever remains of the beam after the parton
collision [1.12]. Particles here are also expected
to balance some of the transverse momenta of the
triggered partons. The quantum number correlations

between the trigger jet and the forward region should be stronger than those between the away side and the trigger jet (this is only true in QCD, and is not predicted in the CIM model).

For both cross section and correlation studies, the comparison between beam types is especially interesting. Theoretically, the pion is made of a valence quark-antiquark pair embedded in a sea of soft quarks and and gluons; on the other hand the proton has 3 valence quarks. Significant differences between these two beam types are thus predicted. Experimentally, there is little known about the pion beam high $p_{\perp}$ events. Most of the published results [1.3, 1.10 and 1.12] in this field are from proton beam measurements. Our group is one of the first to report results on high $p_{\perp}$ pion beam interactions; some of the publications by other groups on pion beams are listed in [1.13].

So far, I have been summarizing some of the general physics involved in jet productions mainly in the framework of a popular model (QCD model by FFF). Other models do exist, they are either

similar to the FFF implementation of QCD or they are much less promising. In this thesis, I shall present some new data in jet physics, emphasizing the differences between proton and pion beams. Qualitative comparisons with FFF will be given throughout this thesis as a motivation for some of our analyses. The detailed comparison of the FFF model with our data will be given in Jim Rohlf's thesis.

1.4 ATOMIC WEIGHT DEPENDENCE OF THE HIGH $P_\perp$ CROSS SECTION

An unexpected piece of physics that was discovered when we were analysing our E260 jet data concerns the effect of a nuclear target on jet production. This was not mentioned in our original E260 proposal. Our aluminium target is really the vacuum jacket for our main liquid hydrogen target. It was only after the discovery that our aluminium target jet cross section is much larger than expected that we realized that we had enough statistics to study the effect of a nuclear target on the jet production. This in fact is the main

topic in this thesis.

During the past three years, several groups
[1.14, 1.15] have studied the production of single
high $p_\perp$ charged hadrons in proton-nucleus
collisions. These experiments cover the
ranges $2 \leqslant A \leqslant 184$, $1 \leqslant p_\perp \leqslant 7$ Gev/c,
$28.5 \leqslant p_{INCIDENT} \leqslant 400$ Gev/c, all six outgoing charged
particle types, and different interaction length
targets. Although, of course, not all combinations
of these parameters have been explored, it is found
in all cases that the A-dependence of the cross
section with all other parameters fixed is well
described by a power law: σ (target of atomic
weight A) is proportional to A^α. α however
depends on the kinematic variables. At low
$p_\perp$, α becomes .7 as expected from Glauber theory
[1.16] and found from total cross section
measurements. As $p_\perp$ increases, α increases rapidly
until at the highest $p_\perp$ measured so far it is
significantly larger than 1. This phenomenon has
been called [1.17] the anomalous nucleus enhancement
(ANE). In this thesis I shall discuss α $(p_\perp)$ for
various triggers. The ANE is seen in our data for
both the single high $p_\perp$ trigger and the jet trigger.

1.5 ATOMIC WEIGHT DEPENDENCE OF PARTICLE DISTRIBUTIONS

The distribution of particles in hadron-nucleus collisions can be very interesting. This may give us a clue to the underlying dynamics of the ANE mentioned above. It is commonly believed that this physics is related to topics such as the space-time development of particle production, the interaction of resonances with nucleons, and perhaps even to the interactions of almost free quarks and gluons with nuclear matter. A qualitative discussion of hadron nucleus scattering in QCD has been given in Ref. [1.18]. Although the theoretical predictions are not firm, it seems clear that the hadrons nucleus scattering amplitude is fundamental. Namely it cannot be predicted, independent of the particular strong interaction theory, from a knowledge of the hadron hadron scattering amplitude and the make up of the nucleus in terms of hadrons.

There have been many attempts to understand the various qualitative features of hadron-nucleus collisions, at both low and high $p_\perp$, in terms of models of hadron-hadron interactions. However, as

far as we know there is still no quantitative
description that can explain all the nuclear effects
observed in high energy hadron collisions [1.19].

Experimentally, the data on low p nuclear
interactions have 3 characteristic features:
(A) In the central rapidity region ($Y_{c.m.}$ roughly
between 0 and 1) the particle production ($\frac{1}{\sigma}\frac{d\sigma}{dY}$) is
independent of nuclear number. Here rapidity, which
is denoted by $Y_{c.m.}$ in the c.m. frame, is defined by
the equation: $Y = .5 \ln((E-p_z)/(E-p_z))$ where $E =$
particle energy and $p_z =$ z component of the
particle momentum.
(B) In the forward region, the number of produced
particles decreases with the nuclear number.   In
some heavy nuclei, this reduction can be factor of
two compared with the hydrogen measurements.   The
data in this region are still very ambiguous.   The
reduction at the very forward rapidity values is
most plausibly interpreted as the the attenuation of
the "beam jet" as it transverses the nucleus.
(C) In the target fragmentation ($Y_{c.m.} < 0$) region,
there is a general increase with A (the nuclear
number) of the number of particles in collisions off
nuclear targets.   This could be due to nucleons

knocked out from the target nucleus; central region
fragments of a second scattering of the beam jet can
also populate the region $Y_{c.M.} < 0$.

The general experimental observation is that
the multiplicity of particles produced in low
$p_\perp$ collision with a nucleus of nuclear number "A" is
significantly less than the multiplicity expected
off a cluster of "A" independent quasi free
nucleons. These observations indicate that there is
very little (if any) intra-nuclear cascading by the
"intermediate" state produced in the hadron-nucleus
collisions. Some people have suggested that the
large α observed in high $p_\perp$ scattering could be due
to additional hard scattering of the "intermediate"
state (quasi free parton state?) before it was
transformed into the observed hadronic state. In a
recent paper [1.20] it has been pointed out that the
larger gluon hadron than quark hadron cross section
expected in QCD could enhance gluon production in
nuclear target experiments. Other possibilities
have also been suggested. For reviews of existing
data on nuclear effects and further discussions on
various models please refer to Reference [1.19].

16

Above we have described previous data on the particle distributions in low $p_\perp$ interactions off nuclear targets. We have also discussed some of their implications which may be useful in interpretating the high $p_\perp$ data. Our experiment also has a low $p_\perp$ minimum bias trigger which will be defined precisely in Chapter II. Our minimum bias data off aluminium show a event structure similar to that seen in the earlier experiments. However we have been able to observe the two particle correlations with a nuclear target for the first time.

In our high $p_\perp$ events, we observe not only the ANE, or large α, in the jet cross section but also some interesting features of the distributions of the associated charged particles both inside and outside the jet. We compare these distributions for the two targets. Observed difference between these targets could be related to the behaviour of partons as they propagate through the nuclear matter.

CHAPTER II

APPARATUS AND TRIGGERS

2.1 APPARATUS

The data described here come from the main run
of the Fermilab Multiparticle Spectrometer (E260) in
the summer of 1976. The apparatus is shown
schematically in figures 2.1 and 2.2 . Details of
the hardware are discussed in Ref. [2.1] . I shall
only give an overview of the apparatus here.

We define our coordinate system by taking the
z-axis as the incoming beam direction, and the
y-axis as the direction pointing up. The positive
x-axis side is called the left side (looking in the
increasing z direction) .

The experiment used the M6W secondary beam in
the Meson Area which can be run at momenta up to 200
Gev/c. The intensity was around 2×10^6/sec, during a
1.75-second spill while the cycle time was
approximately four times per minute. Most of the

analyzed data in this thesis were taken at 200
Gev/c, with about 20% at 190 Gev/c.   A list of beam
polarities and energies for all the data in the main
run (including the 130 Gev data which have not been
analyzed yet) is presented in [2.2].   The beam
composition has been determined to be [2.3a] :

	-200 Gev	-190 Gev
π^-	.949	.946
K^-	.043 ± .004	.044 ± .004
$\bar{P}$	.008 ± .001	.010 ± .001

	200 Gev	190 Gev
π^+	.180 ± .020	.206 ± .020
K^+	.023 ± .002	.026 ± .003
P	.797 ± .020	.768 ± .020

We shall now describe the various parts of the
apparatus in the order that they are transversed by
the beam as it passes through our spectrometer.

A.   Beam Cerenkov Counters
These counters which are used for pion-kaon-proton
separation are not shown in figures 2.1 and 2.2.

Further discussion of the beam particle
identification is presented in Ref. [2.3b].

B.   Beam PWC's (BA and BB)

These are proportional wire chambers (PWC) used to
define the beam direction (only the station BB,
nearer to the target, is shown in Fig.   2.1).
The BA chambers have two x-y modules and are located
about 20 meters upstream from the target.   Each
module consists of an x-y pair with each view having
56 wires which are spaced 13/inch.
There are 5 BB chambers just upstream of the target;
BBV and BBW are similar to BA, with 56 wires, which
are spaced 13/inch and they are rotated at angles of
30° and 120° relative to the horizontal
respectively.   BBX, BBY and BBU are 64 wire planes
with spacing at 26/inch and they have similar
construction to the A chambers discussed below.

C.   Target

This a 12-in long, 1-in radius liquid hydrogen
target enclosed by an aluminium jacket which is
about .03-in thick.

D.   ABC-station

These are PWC's used to find tracks before the
magnet.

The A station consists of two modules: an x-y
module and a 45° rotated u-v module. The x-y module
consists of two x-planes staggered for higher
resolution, while the two y-planes were also
intended to be staggered but due to assembly errors
they were not. The u-v module is a separate module,
assembled like the x-y module but containing only 2
planes (one x and one y), and rotated 45°. Each of
the six measuring planes in the A station consists
of 256 wires spaced at 26/inch.

The B and C station PWC's are a total of 5 planes of
similar construction, divided into B' (vertical
wires only), B (x and y in one module) and C (x and
y, configured so as to fit into the magnet as
shown). The apertures of all these modules are 40
inches horizontally by 26 inches vertically. Each
vertical (x coordinate) set has 512 wires at 13
wires per inch and each horizontal (y coordinate)
set has 320 wires at 13 wires per inch.

E.   Magnet

This is a superconducting magnet for momentum
analysis of our tracks. For the measurements

reported here, the field was run at about half the maximum value which corresponds to a transverse momentum kick of .379 Gev/c imparted by the magnet. The field was deliberately set low even though this led to poorer momentum resolution. A higher field would lead to a greater bias in our calorimeter $p_\perp$ trigger.

F.   D-station

This station consists of 4 planes: Dx, Dy, Du and Dv where Du and Dv are at angles of 15^0 and 105^6 respectively relative to the vertical. Each plane has 320 wires at 5.5 wires/inch. These PWC's are used for track finding after the magnet. Although their resolution is poor compared to the spark chambers they do have much better time resolution and are not sensitive to interactions other than the trigger one that occur within the memory time of the spark chambers.

G.   E-station

These are magnetostrictive read out spark chambers with better spatial accuracy than the PWC's. There are 4 modules in the E station. Each module consists of a y-y gap and x-u gap. The chamber size

is 8' (horizontal) by 4' (vertical). The chambers
use .005" thick aluminium wires spaced at 32/inch.
The signal is read out with magnetostrictive wands
which have pickups at both ends. The complete
system has 6 signals (2 each for x,y,u) per module
or a total of 24. The wires in the u-plane are at a
angle θ given by $\tan\theta = .1$ with respect to the x
wires. The signals are amplified, discriminated and
fed into MTD's (Multi-Time Digitizer. Reference:
B. Bertolucci, SLAC-PUB-1177).

The spatial resolution, which depends on the
accuracy of determining the centroid of the signal,
is found to be around .7 mm.

The pair resolution which indicates how well we can
separate two distinct tracks was determined to be
around 5.5 mm in a detailed analysis which I have
described in a memo [2.4]. Obviously the poor pair
resolution reflects the intrinsic width of the
magnetostrictive pulse; the resolution of .7 mm
shows that one can find the mean of a pulse to a
much better accuracy than its width. No correction
has been made for tracks which have been lost
because they were so close to another track as to be
within the pair resolution. The problem is most
serious in the y view where 5% of the tracks are

affected. However we do correctly identify
particles as distinct those which although together
in the y view are separate in the x view. As the
magnet bends oppositely charged particles apart. We
see that the pair resolution only affects particles,
or matched tracks, that have the same charge,
comparable momenta and are close in both x and y
views. Less than 0.1% of particles fall into this
category.

H.   C1

Gas Cerenkov counter C1, with 22 cells, can be used
for final state particle identification. The data
reported here do not use information from this
counter. Analyses using C1 and C2 will be reported
in other theses [1.9].

I.   F-station

These are spark chambers which are of similar
construction to the E-station spark chambers, but
larger in size (12'X6').

J.   F'-station

These are two x-plane PWC's covering the faces of
the calorimeters. They are constructed similarly to

the D chambers but with 4 wires/inch and only 130 vertical wires per module. Their use is as for the D station to provide good time resolution information on tracks entering the calorimeters.

K.   Calorimeters

Two large calorimeters, placed at approximately $90°$ in the center-of-mass frame, are used for triggering on high $p_\perp$ events. Each calorimeter is divided into 4 modules which are each divided longitudinally into two sections. The front section is a lead-scintillator sandwich shower counter containing 15 radiation lengths of lead. The back section is a iron-scintillator sandwich designed to measure hadronic energy. This back section contains 30" or 4.5 absorption lengths of steel. By using the ratio of the top and bottom phototube pulse heights, the mean vertical position of particles entering the module can be determined with a resolution of 10cm at E = 25 Gev. This resolution scales like $1/\sqrt{E}$ with energy. It is $.33/\sqrt{E}$ for the front section, and $1.03/\sqrt{E}$ for the hadronic section. Further descriptions of the hardware and the response of the calorimeter are discussed elsewhere ([2.5] to [2.8]).

L.   F''

This x-plane PWC is also called the F'-center.   It
is placed in the center of the xy-plane
perpendicular to the beam line, covering the central
regions that are missed by the F'-station mentioned
above in section J.   Its construction is the same as
the D chamber.   This chamber is particularly
important because of the large density of fake
tracks in the sparks chambers near the beam region.

M.   C2

This is our second gas Cerenkov counter for
identification of the final particle.   It has 16
cells and it is also not used for the data reported
in this thesis.

The time required to read in an event is
dominated by the time it takes to read in data from
the spark chamber which is approximately 20 msec for
reading in the 48 channels with 16 words/channel.
Thus the data collection system is limited to around
50 events per 1-sec spill with 1200 to 1500 words
read in per event.   In the actual E260 run, due to
high event multiplicity and beam intensity, we ran
the spark chamber with 50 msec dead time and we take

in around 10 to 15 events per 1.75-sec spill. The
data are read into the computer and buffered to the
disk during the beam spill. After the beam spill,
the data on the disk is written onto the tape and
also made available to our on-line software program
(MULTI) for histograming event attributes and making
event displays.

2.2   TRIGGERS

        Our experiment has 3 major triggers:

A.   Minimum Bias or Interacting Beam Trigger

        If an incident beam particle is observed before
the target and no count is recorded by a 2"x 2"
scintillator counter placed along the beam line just
downstream of the F-station (see Fig. 2.1), then a
pretrigger was generated. This was the prerequisite
for firing the spark chambers, manipulating the
calorimeter pulses, recording all the information
onto the magnetic tape and so on; therefore every
E260 trigger is associated with a pretrigger. For
every 9 calorimeter triggers a pretrigger was also
recorded as a trigger. This selected pretrigger,

also called the interacting beam trigger, gives an
essentially unbiased sample of high multiplicity low
$p_\perp$ events but is inefficient for elastic and
diffractive scatterings.

B.   Single Particle Trigger

   The pulse heights in the 4 modules of the
calorimeters are attenuated relative to each other
by amounts proportional to the mean laboratory
angles of the modules to give signals proportional
to $p_\perp$. If this $p_\perp$ (as defined by the attenuated
pulse) in any one of the 4 modules (in either
calorimeter) is greater than the trigger bias (set
at nominal values of 2 and 3 Gev/c), then a high
$p_\perp$ single particle trigger is generated.

C.   Jet Trigger

   This trigger requires the summed calorimeter
$p_\perp$ of the 4 modules (in either calorimeter) to
exceed the preset trigger bias (set at nominal
values of 3 and 4 Gev/c).

   For both single particle and jet triggers, the
exact hardware trigger bias setting varies slightly
from run to run. These settings are listed in

Ref. [2.2].

Although we have 3 types of triggers, there are
really 5 triggers (2 thresholds for both single
particle and jet triggers) in our hardware
triggering system.   They have been called in our
experiment as the INTBM, MEDPT, HIPT, LOJET, and
HIJET triggers.   All these triggers could be
generated simultaneously during the data taking.
The lower threshold triggers (MEDPT and LOJET
triggers) were "divided" before the online hardware
logic decided whether to fire the spark chambers.
When I say "divided", I mean that only one out of a
certain number of triggers (this number is also
called the hardware division factor) could be
accepted as a real trigger.   In cases when we were
taking in more than one type of divided trigger, the
real division factor used for computing cross
section is smaller than the hardware division factor
due to a nonzero probability for satisfying both
triggers simultaneously (see [2.9] for more detail).
All these hardware division factors are again listed
in Ref. [2.2].

CHAPTER III

PROCEDURE

3.1 Track Finding and Clean Up

Track reconstruction in front of the magnet was
done entirely with PWC's; behind the magnet it was
done with a combination of large PWC's and spark
chambers. There were four stages to the procedure
(see References [3.1] and [3.2]) :

(1) Tracks were fitted in the x view before the
magnet and in the y view all the way through the
spectrometer. The best of these x and y tracks were
selected to determine the vertex position in three
dimensions. In the case that the above algorithm
failed (about 5% of the finally analyzed events), a
second attempt was then made to find the vertex with
the beam chamber information. An event with a
successful vertex was then passed through the
following three stages. These stages only used the
vertex information from the first stage; this
vertex point was used for all the y tracks (stage 2)

and the x tracks before the magnet (stage 3). The
vertex constraint made the track finding much easier
and allowed us to disentangle tracks that were
impossible without this constraint.

(2)   We found all the y view tracks and the x view
tracks after the magnet.   These x and y tracks were
then matched together using the stereo-angle spark
chambers.

(3)   These matched sets of tracks were linked to
tracks in front of the magnet, requiring that tracks
in front of the magnet must go through the vertex.
A set of matched tracks was called a "particle".
The difference in the slope of the x view tracks
before and after the magnet defined the momentum of
the "particle".

(4)   We deleted some spurious particles that shared
tracks , in either the x or y view, with other good
particles.   This selection was based on the
chi-squared probability of matching and the number
of sparks used in the matching.   Note that each
stage was run with rather loose constraints so as to
be very efficient.   As described later, we cleaned

up the sample by using cuts based on information
from all the stages of track finding.

Our vertex distribution is shown in Fig. 3.1a
and it will be discussed further in Chapter V. The
target is clearly seen with very little background.
The measurement resolution for the z coordinate of
the vertex, which can be estimated from the width of
the aluminium peak, is around 2 mm.

The momentum resolution of a particle is
related to the spatial resolution of our chambers;
the quantity $\Delta p/p^2$, which is proportional to the
angular resolution in the x view in front of the
magnet, should be a constant in the laboratory
frame. By runing beams of known energy through the
spectrometer, we determined the momentum resolution
for the charged particle to be around $\Delta p/p =$
.0007p (p in Gev/c) [3.3].

Due to the high event multiplicity and sparks
that were not associated with the triggered event,
we were concerned about spurious particles generated
by our track finding method. These bad particles
contain both incorrect tracks and real tracks that

were incorrectly matched. We removed some particles whose track momentum is significantly larger than the calorimeter signal. For particles that do not hit the calorimeter, we cannot apply such cuts. Fake particles in the forward region are therefore much harder to handle. In order to handle these and other spurious particles, we devise the procedure described below.

We construct a quality factor Q for each particle from the number of PWC hits on all its tracks and the chi-squared for its tracks in front of the magnet. We remove those candidate particles with very low quality Q. However the density of fake tracks in the forward region is so high that special treatment is needed here. First we remove all particle with $P_{LAB} >$ 200 Gev/c and those that hit the 2X2 counter. We also remove some of the poor quality particles , with low values for Q (but above the previous cut), that are either very close to the 2X2 counter or have at least one track that hits the 2X2 counter. We remove about 10% of all particles with these cuts. The majority of the particles removed have large momenta and are in the forward region where the track finding is most ambiguous.

After all these cuts, we make further physics plots
with yet more stringent cuts and find no significant
differences. We conclude that our quality cuts have
given us a clean data sample. A detailed
description of the quality factor studies and these
clean particle cuts are presented in Ref. [3.4].

Two approaches have been used to estimate our
overall track finding efficiency. They are
described in the following:

(1) We histogram the number of PWC hits (N_p) used
by each track. We observe results typified in Fig.
3.2a. The sharp edge at the lower end of the curve
is mainly due to the minimum hit requirement for
accepting a track in our chi squared fit. By
extrapolating (as indicated by the dotted line) from
this edge to the zero point, we can estimate the
track finding efficiency by calculating the ratio of
the area underneath the dotted curve to the total.
This fraction usually turns out to be around 95%.
The problem with this scheme is that we still do not
understand the various smearings of the edge due to
our complicated software cuts used in our track
reconstruction scheme and we also do not know
exactly how to extrapolate (we do not know the

slope) ;   although we do expect that the hit

distribution should be very similar to a binomial

distribution.

(2) D_X and D_Y are probably the best two chambers

after the magnet.   The fact that I was involved in

building these chambers is probably irrelevant.   We

found that there is almost no noise in these

chambers during most of our data taking.   I define

the fraction f_D by the equation

$$f_D = \frac{\text{No. of particles that have hits in the D chamber}}{\text{Total no. of D hits}}$$

A plot of f_D (for the average of D_X and D_Y chambers)

vs.   the the mean event multiplicity (N_p) is shown

in Fig.   3.2b.   If each D hit can be used only once

in the track reconstruction, then f_D essentially

gives the fraction of the total D hits that are

used.   Events with large values of f_D are events

that are very efficient in finding all the tracks.

In real situation, f_D can be greater than 1 due to

sharing of sparks between tracks.   The dip at the

lower f_D end is due to tracks missed because of the

inefficiency of other chambers.   The plateau above f_D

=.75 seems to indicates that our $f_D > 1$ values are

not due to extra spurious particles that share D
hits with some real particles, but rather due to the
sharing of D hits by real particles. This happens
quite often due to the crude spatial resolution of
the D chambers. We propose that the true mean event
multiplicity is that given by the plateau value $\langle N_p \rangle$
$> \sim 10$ for $f_D > 0.75$. Then the overall track finding
efficiency can be estimated by dividing the observed
mean event multiplicity for all events by the true
mean estimated as above. This efficiency turns out
to be 93% for that particular run shown in Fig.
3.2b.

From these studies, we believe our track
finding efficiency is between 90 TO 95%. Most of
these estimates are based on results for a group of
few selected runs. Although it would be better to
use all runs, our current analysis is sufficient for
the physics discussed in this thesis.

3.2 CALORIMETER ANALYSIS

A good understanding of the calorimeter is
essential for any calorimeter-triggered jet

experiment.   Since we are measuring a steep
$p_\perp$ spectrum, the jet $p_\perp$ will be most likely to be
overestimated due to bad calorimeter resolutions.
Some experiments assume that the real jet $p_\perp$ is just
the calorimeter $p_\perp$ (calculated from the pulses)
minus some constant number that represents
fluctuations.   This ,we believe, is not a very
satisfactory approach.   In our experiment, we can
measure the charged tracks very accurately within a
large kinematic acceptance (Fig.   3.1b) .   Our
calorimeter is used mainly, in the final analysis,
for checking the charged energies and estimating
neutrals.   In this thesis, we avoid the study of
mainly neutral jets for which one has to rely
heavily on the calorimeter.   Our jet $p_\perp$ used here is
almost independent of the calorimeter fluctuations.

    The analysis of our calorimeter consists of
following steps [a] :

1.   We first calibrate our calorimeter by runing
the beam directly into the calorimeter .   Beam
energies from 10 to 40 Gev were used.   This process
determined all the pulse height to energy
proportionality constants, the attenuation lengths

and any calorimeter constants used in our neutral
analysis (e.g. the average fraction of energy
deposited by a charged hadron in the electromagnetic
calorimeter).

2.   We then take the real data, using only tracks
opposite to the trigger side (called away side in
this thesis). We only select events that we believe
have very little or no neutral energy entering the
calorimeter (see Ref. [2.8] for a detailed
description of these neutral cuts). We confirm our
beam calibration in step 1 by comparing the total
detected calorimeter energy with the track energy.
By plotting the calorimeter energy in the hit module
over P_{LAB} versus distance of the track from the
center of the hit module (this distance is named as
"$D_{HIT} - D_{MOD}$" in Figure 3.3), we generate an energy
distribution shape [2.8b] which tells us the mean
energy deposited by a single charged particle in the
hit module as a function of "$D_{HIT} - D_{MOD}$".

3.   Now, we shall describe how we analyse the
calorimeter signals on our jet and single particle
data. The basic idea is to use the energy
distribution shape derived above to predict the

energy deposited by all the charged particles
entering the calorimeter. We compare our predicted
energies with the actual calorimeter pulse heights.
If the calorimeter signals do not agree with the
predictions, we shall then try to find neutral
particles that correspond to the energy discrepancy.
To illustrate our neutral extraction scheme, we
shall go over the whole procedure in detail for the
following simplified case.

Let us assume we have only one module. A
charged particle of energy Eq entering the
calorimeter will deposit

$f_h * Eq_h$ in the hadronic section,

$(1-f_h) * Eq_e$ in the electromagnetic section;

Where:

f_h is the fraction of energy deposited in
the hadronic section,

Eq_h is the amount of energy that it will
deposit in the hadronic section, according to the
known pulse shape, if it loses all its energy in the
hadronic section,

Eq_e is the similar response prediction for
the electromagnetic section.

We also define the neutral energy

$$E_n = E_\hbar + E_e - f_\hbar Eq_\hbar - Eq_e (1-f_\hbar)$$

We fit with the chi squared sum:

$$\chi^2 = \frac{(E_\hbar - f_\hbar Eq_\hbar)^2}{\sigma_\hbar^2} + \frac{(E_e - Eq_e(1-f_\hbar))^2}{\sigma_e^2}$$

where $E_\hbar$, E_e are the energies detected in the hadron and electron sections of the calorimeter. If $\chi^2 <$ 5, we say the event fits with the pure charged energy only. For $\chi^2 > 5$, we fit again with neutrals plus the charged energies; first with additional pure hadronic neutrals only (FIT2 in Fig. 3.4 on the next page), then with additional pure electromagnetic neutrals only (FIT3 in Fig. 3.4). We pick the best fit (among FIT2 and FIT3). If all fits mentioned fail, we assume that both electromagnetic and hadronic neutrals are present. We find their energies by a simple subtraction that assumes $f_\hbar = .8$ which is the mean value of $f_\hbar$ seen in our beam calibration. The whole procedure is summarized by the following chart (Figure 3.4):

START

$\checkmark$ = Yes
$\times$ = No

Any charged particle seen in the calorimeter?

Any acceptable calorimeter signal ?

FIT1:
Track momentum = calorimeter response ?

Is the energy involved very little ?

$E_n > 0$?

FIT2:
Fit with pure hadronic neutral plus charged particle

FIT3:
Fit with pure E.M. neutral plus charged particle

At least one good fit ?

Pick the best fit

Assume FH=.8, get neutral by subtraction

$E_n > 0$?

ACCEPTED CHARGED PARTICLE

REJECTED or IGNORED

ACCEPTED NEUTRAL

Fig. 3.4

In the real analysis, we have more information than mentioned. Each calorimeter module has 2 TOP and 2 BOTTOM pulses, which means we have 4 inputs for both the hadronic and the electromagnetic sections, and we have 3 free parameters: Eq, Yq (Y_q is the y coordinate of the charged particle) and f_h in step FIT1 (see Fig. 3.4). The real formula of the chi squared sum used is also more complicated, it includes correlation coefficients (between TOP and BOTTOM pulses) obtained in our beam calibration studies. Also in our fitting, f_h is forced to lie between 0 and 1. Our fitted f_h in FIT1, which is a free parameter, is found to be around .8 and has a very similar shape to that in our beam calibration run.

Cases where χ^2 is large and E_h is large and negative are rare. If this does happen, large momentum tracks that contribute to Eq_h and Eq_e are removed. This calorimeter comparison cut has already been mentioned (in section 3.1) previously in our track quality discussions.

For events accepted by our FIT1, i.e., ones for which no neutral was generated; we found $\langle En \rangle = 0$ on

the away side, and <En> greater than 0 on the

trigger side.   The trigger side <En> > 0 can be

understood as the high $p_\perp$ trigger favours the

upward fluctuation of the calorimeter signal.   These

also indicate our chi squared fitting procedure

takes into account the calorimeter trigger bias

automatically on the trigger side, and our cut for

the chi squared sum is reasonable as indicated by

the <En>=0 on the away side.   We justify further our

neutral scheme by applying the scheme on some Monte

Carlo data.   The derived neutrals agree very well

with the theoretical neutrals used in the Monte

Carlo generation program.

FOOTNOTE [a]   Steps 1 and 2 are discussed in more detail in references [2.7] and [2.8] (see also [2.5] and [2.6]).

FOOTNOTE [b]   There are differences in responses between hadrons and electrons entering our electromagnetic calorimeter section.   Such a difference is included in our response predictions.

CHAPTER IV

JETS

4.1   JET DEFINITION

Our calorimeters trigger on the part of a jet contained within a particular solid angle. Study of both Monte Carlo and real data showed that it was possible to improve the jet definition by including particles that missed the calorimeter. We now describe the technique developed. Details may be found in Jim Rohlf's long paper [4.1].

A jet is defined here as a cluster of particles going together in a certain direction. We add up all particles (charged particles from tracks and neutrals extracted from the calorimeter signals) within a 45 degree cone of the calorimeter vector

STEP 1

(a)
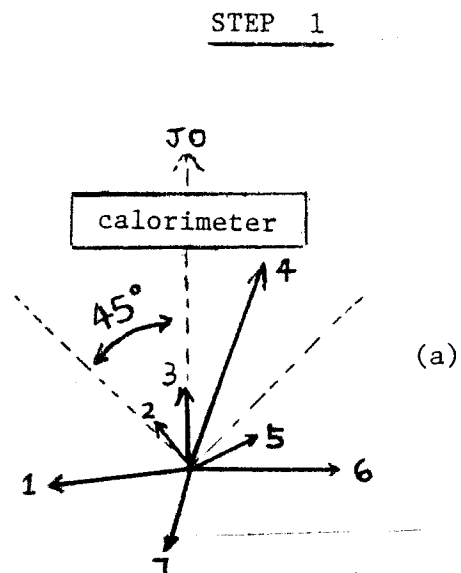
Figure 4.1

(vector JO in Figure 4.1a).
The latter is defined to
be the vector that points
to the center of the calo-
rimeter in the center of
mass frame. The vector
sum (vector J1 in Figure
4.1b) of all the parti-
cles in the cone defines a
direction which we use as
the axis of a new cone of
40 degrees. All particles
within this new cone are
considered to be parts of
the final jet (see Figure
4.1c). The 4-vector of
the jet is the vector sum
(vector J2 in Figure 4.1d
) of all particles in the
jet. The second step in
our jet definition can be
considered as an iteration
of the first. It is in-
tended mainly to reduce
the bias by the initial

(b)

STEP 2

(c)

Accepted
Jet

(d)
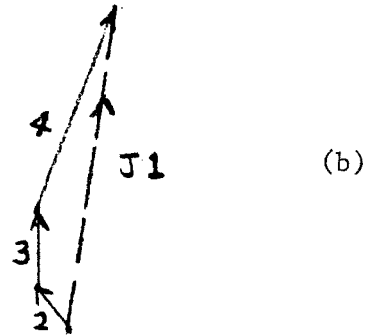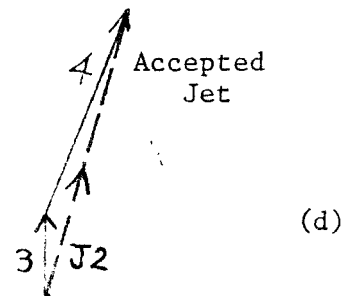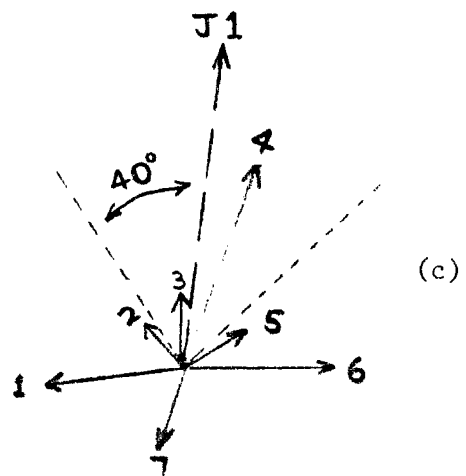
Figure 4.1

condition in our jet definition.

We only study jets that satisfy the following fiducial cuts (on J2) :

$$|C.M. \text{rapidity}| < .2$$

$$|\phi| < 20^{\circ} \quad \text{or} \quad |180^{\circ} - \phi| < 20^{\circ}$$

$$\text{where} \quad \tan\phi = (p_Y / p_X)$$

The cone angles used in our jet definition are defined essentially by the calorimeter size. They are picked after a Monte Carlo study using a quark-gluon jet model developed by FFF [1.6]. In this model, a jet going at $X_{\parallel} = 0$ ($x_{\parallel} = 2p_Z / \sqrt{s}$) in the C.M. frame fragments into a cluster of particles of various energies E. Our Monte Carlo study with this model shows that high energy jet fragments (E > 1.0 Gev) will almost always be included in our empirically defined jet discussed above. For lower energy fragments, the number of particles in the real jet that are missed by our empirical jet is almost equal to the number of outside particles (i.e. members of beam, target and away side jets) that are included in our empirical jet. Low energy particles are hard to handle both in theoretical

models and experimental analyses. Fortunately, such
particles can always be shown to be unimportant in
most jet physics. Despite this low energy fragment
uncertainty, the mean derived $p_\perp$ of our empirical
jet agrees very well with the real jet $p_\perp$ input
into our Monte Carlo program. This study convinces
us that we have a reasonable jet definition. It can
be used to test many theoretical ideas.

4.2 JET SELECTION

Our jet consists of 3 components: charged,
electromagnetic neutral, and hadronic neutral. The
hadronic neutral component includes track finding
inefficiencies and non-vertex associated charged
tracks (e.g., $K_S^{\bullet}$, Λ^o decays) as well as real neutral
hadrons (K_L^o and neutrons). This component has the
biggest uncertainty and unless handled carefully
would be dominated by the background of fake
hadronic neutrals produced by the upward
fluctuations in the calorimeter energies deposited
by charged particles in the hadronic section. This
is enhanced by the trigger bias due to the sharply
falling high $p_\perp$ spectrum. A study of hadronic

neutral fraction versus jet $p_\perp$ indicates that most of our $p_\perp > 7$ Gev/c jets have large hadronic neutral components. This indicates that especially at high $p_\perp$ most of our hadronic neutrals are fake neutrals. This is, in fact, the main headache of all presently existing calorimeter triggered jet experiments. In this thesis, we avoid this headache by selecting jets with a hadronic neutral fraction less than .4. This is suggested by our study that if we make a hadronic neutral fraction cut of .5 or less on both sides , the away side neutral fraction agrees with the trigger side. A cut of .4 is in fact reasonably conservative. We will justify this cut further in chapter V.

Another background, that had worried us, is caused by events with a beam halo particle going into the calorimeter simultaneously with an ordinary interaction in our target. Such events should be rare, because we do have shieldings against halo particles (the magnet and some other shielding near the beam). Unfortunately the cross section for high $p_\perp$ events is also very small. Such a background could be serious at high $p_\perp$. Scanning through some data, we found such a halo background could be as

high as 10% for $p_{\perp} > 6$ events before any hadronic

fraction cut. For $p_{\perp} > 7$, it could be occurring 50%

of the time in some runs. All these halo events

typically consists of one beam halo going parallel

to the z-axis with its track clearly seen in our

spectrometer going together with a low $p_{\perp}$

interaction in our target. Such a halo track is

usually missed by our track finding as we only look

for tracks coming from the vertex. Therefore, this

background will almost always be defined as a pure

neutral jet event by our jet definition. Our

hadronic neutral fraction cut removed almost all of

this background. We make a further cut by requiring

the total neutral fraction to be less than .9 . We

also ignore jets with $p_{\perp} > 6.5$.

We cut away about 23% of our jet triggers

(becoming as high as 50% at high $p_{\perp}$) with these

neutral fraction cuts. Most of these events which

are removed are probably junk; in any reasonable

model our neutral cuts should remove very few real

high $p_{\perp}$ jets. We are studying here a particular

class of jets, but we believe our specially selected

jets are clean and their $p_{\perp}$ value is very well

determined. Our results presented here are

therefore quite independent of the poor calorimeter resolution.

4.3   JET CROSS SECTION

Although I try to discuss here only the results of certain selected jets, one can try to correct for the cuts made in getting a clean sample. The total Jet cross section is computed by using a Monte Carlo correction for losses from neutral cuts (10% to 15% loss in models like FFF) and apparatus acceptances (around 50%) . Jim Rohlf has written such a Monte Carlo program using the FFF quark-gluon jet model mentioned above. All his work is discussed in his thesis [1.9] but some of his preliminary results are presented here (Figures 4.2 and 4.3) without further detailed discussion. Most of the other results presented in this thesis do not involve his Monte Carlo corrections. Therefore my results are not sensitive to the theoretical assumptions used in our Monte Carlo program which may affect the cross section results slightly.

CHAPTER V

COMPARISON OF HYDROGEN AND ALUMINIUM

CROSS SECTIONS

5.1 DEFINITION OF α

In a conventional way, we define α by

$$A_{AL}^{\alpha} = \frac{\sigma_{AL}}{\sigma_{HY}} \tag{5.1}$$

where σ are cross sections per nucleus and A_{AL} is the atomic weight of aluminium.

In fact, we use the formula

$$\alpha = C_2 \ln \left(C_1 \frac{N_{AL}}{N_{HY}} \right) \tag{5.2}$$

where $\quad C_1 = \dfrac{A_{AL}}{A_{HY}} \dfrac{\Delta Z_{HY}}{\Delta Z_{AL}} \dfrac{D_{HY}}{D_{AL}} \dfrac{R_{HY}}{R_{AL}} \tag{5.3}$

A = atomic weight

ΔZ = target length used

R = beam attenuation in the target

D = density of the target

N = number of events

$C_2 = 1/\ln(A_{AL}) = .303$

Our hydrogen target is about 30 cm long. In
order to reduce nuclear contaminations due to caps
at both tips (see Figures 2.2 and 3.1) , we make a
fiducial cut by removing 1-cm off each ends in our
analysis (Fig. 3.1a) . This makes $\Delta Z_{HY} = 28$ cm.
Our aluminium target is measured to be: $\Delta Z_{AL} =$
.031"$\pm$.005". The uncertainty in ΔZ_{AL} is the main
systematic error in our α computation. Other
uncertainties, such as the acceptance difference
between the two targets, can be estimated by looking
at the slope of vertex distribution (see next
section 5.2) or using a Monte Carlo simulation of
the data. Another possible systematic shift is the
difference in the trigger efficiency caused by the
different $p_\perp$ kicks from the magnet for the different
target z positions. This effect is only important
for $p_\perp$'s near the trigger threshold. This and any
other threshold related bias can be checked by
computing α's for different trigger thresholds. We
shall always ignore data far below the thresholds.

Our total systematic error in α is estimated
to be around $\sigma_\alpha = .05$. It is included (in addition
to the statistical error) in our α versus $p_\perp$ plots,
while it is not included in most of the other plots.

R_{HY}/R_{AL} is calculated with the known absorption cross section. It is around 1.024 for proton beam and 1.016 for pion beams. This is a very small effect compared to other uncertainties in α. We include such corrections just for completeness. Our final values of C_1 used are:

255.1 for proton beam

252.8 for pion beam

5.2 ACCEPTANCE STUDY

The Aluminum and proton target data come from two slightly different target positions. Any dependence of the acceptance on the target position will affect our results. We do not need the absolute acceptances for both targets in our present study. What we want to show here is that there is essentially no difference in the value of the acceptances between our hydrogen and aluminium targets.

Our Monte Carlo study shows there is no such difference. We pursue this problem further using our real data. As shown in Figure 3.1a, we have a

long hydrogen target and our very thin aluminium
target is very close to the lower tip of the
hydrogen target. Any serious acceptance bias as a
function of position will appear when we look at the
slope of our hydrogen vertex distribution (Figures
5.1a to 5.1c). We do not have enough statistics for
jets above threshold to determine the slope very
accurately. It agrees with the zero slope, but it
agrees even better with the expected beam
attenuation (Figure 5.1d). We have more statistics
for lower $p_\perp$ (2 to 3 Gev/c) jets which are however
just below the threshold. The vertex distribution
for this biased sample has about the same slope as
the high $p_\perp$ unbiased jets'. A more careful fit
indicates there could be a maximum acceptance
difference of about 2%, for lower $p_\perp$ jets, which
corresponds to $\sigma_\alpha = .006$ which is small compared to
other uncertainties in our computation of α. One
possible source for this tiny difference is the
trigger bias caused by the magnet which we shall
discuss further in section 5.5.

The vertex distribution for minimum bias data
is flat for all beam types. This means we also have
an acceptance difference of about 2% (the value of

the estimated beam attenuation) for our interacting
beam triggers. However this difference has the
opposite sign to the corresponding difference for
the jets discussed above. This can be explained by
the difference in the geometric efficiency of the
2X2 veto counter which is again sensitive to the
different effective magnet kick. This will be
discussed in section 5.5 .

This study of the hydrogen target vertex
distribution confirms that we do not have any
serious acceptance problem within the expected
accuracy of our target comparison results. The
uncertainty in the slope determination is used to
estimate the systematic error in α due to
acceptance uncertainties. This was added in
quadrature to the total systematic error in α .

5.3 RESULTS

In figures 5.2a to 5.2c, we plot α versus
$p_\perp$ for jets, single charged particles and
double-jets for different trigger biases. The
definition of a jet has been discussed in Chapter

IV.   I shall describe the other trigger types in the following:

A.   Single Charged Particle

This sample comes from the calorimeter single particle trigger. This trigger was in fact not very clean-being contaminated by calorimeter fluctuations and multiparticle triggers. However we were able to select true single particles very cleanly in the offline software. We impose the same fiducial window cut (described in section 4.1) as for the jets on these particles. We use both the calorimeter energy comparison and track quality factor to clean up the tracks entering the calorimeter. Particles included in this data set are very clean.

B.   Double-jets

A double-jet event is defined as an event in which 2 back to back jets (one in each calorimeter) are found by our jet definition (see section 4.1) and the absolute $p_\perp$ difference between these 2 jets is less than 1 Gev/c. This happens about 10% of the time for all our single jet events.

C.   Minimum Bias

The minimum bias trigger has already been described in section 2.2. We in fact distinguish two different selections of this data sample which are denoted "jet" and "single particle". In the "jet" minimum bias plots, we include the whole minimum bias data sample. The $p_\perp = 0$ bin includes events in which no jet is found, i.e. in which there is no calorimeter signal. On the other hand, for the single charged particle plots , we require at least one charged particle incident on the calorimeter within our $x_{||} = 0$ fiducial window defined above in Chapter IV.

The data shown in figures 5.2a to 5.2c show that our α values are quite independent of the trigger thresholds. This is another indication that our results are not affected by the crude resolution of the calorimeter or any other threshold dependent trigger biases. We do not have enough statistics to say anything very conclusively about double-jets. There is no strong indication of decreasing α at large $p_\perp$ for these events. This is in contrast with the results for double single particle events [5.1]

which show an α that lies lower than that for single particles. This does not contradict our jet data because we show in chapters 6 and 7 that the make up (in terms of charged particles) of both the trigger and the away side jets are different for Aluminum and proton targets.

In Figure 5.3, we combine all the interesting results for α. Some general observations are:

(1) α seems to be larger for the jet trigger than the single charged particle trigger. For both triggers α is greater than 1 for $p_\perp > 1$ Gev/c.
(2) For both minimum bias and single particle data sets, α is independent of the beam types. For the jet trigger, the value of α for a proton beam is significantly larger than that for a pion beam, especially when $p_\perp > 3.5$. There is no difference seen between π^+ and π^- beams.
(3) α does not approach the expected value of .7 as $p_\perp$ approaches 0.

The significance of these observations will be discussed further in later sections.

We try to compare our data with the published single particle results from the Chicago-Princeton collaboration [1.15]. We take their proton and Aluminum (interpolated from their Ti and Be data) cross sections at 200 Gev, and using equation 5.1, we derived α for the $p_\perp$ values of: .77, 3.08 and 4.61 Gev/c . These points are included in Figure 5.3a and they agree with our data within the estimated errors. A relative shift of .04 between the experiments leads to better agreement. This is a small shift compared to the large α values shown in these plots. The Chicago-Princeton measurement has an overall normalization uncertainty of order 20% , which corresponds to a possible σ_α of around .07 . The small shift of order .04 between the two experiments can be due to systematic uncertainties in either experiments.

5.4 EFFECT OF MULTIPLICITY ON α

The observation, that our α does not approach .7 at low $p_\perp$, was annoying. This could be an indication that our overall normalization is very wrong. We believe, as indicated by our vertex study

(section 5.2), that this is unlikely. We are now convinced that this can be due to the way we define our minimum bias sample. The anti-beam counter, defining this sample, has removed most of the low multiplicity diffractive type of interactions. Further, when we analyse our data, we require at least 2 charged particles detected before the magnet to form a good vertex. All these conditions mean we have very poor efficiency for low multiplicity events. This will not affect our high $p_\perp$ data at all since the mean charged multiplicity seen in our experiment for such events is around 10, but it does affect our very low $p_\perp$ interacting beam events. In Figure 5.4, we plot the mean charged multiplicity seen after the magnet (denoted by $\langle N \rangle$) versus α . It clearly indicates that α depends strongly on multiplicity and α approaches .7 for low $p_\perp$ as $\langle N \rangle$ approaches 1. This confirms our idea that the reason α does not approach .7 as $p_\perp$ approaches 0 in Fig. 5.3 is probably due to a loss of low multiplicity events.

It has been observed by other experimenters [1.18] and by us (see figures in Chapter VI and VII) that in general there are increases in

multiplicities in the central (C.M. rapidity around
0) and target fragmentation (C.M. rapidity < 0)
regions for low $p_\perp$ interactions off a heavy nucleus.
It is interesting to ask the question whether this
observed α dependence on the overall multiplicity
can be attributed to either the particles in the jet
or those outside the jet.

We divide the total charged multiplicity into
two parts: the charged multiplicity in the jet and
the charged multiplicity outside the jet. We plot
separately α against both of these multiplicities
in figures 5.5 and 5.6. The trigger jet is defined
to be the jet with the larger calorimeter signal in
case of double-jet events. These plots show that
the ANE ($\alpha > 1$) is enhanced by an increase in either
multiplicity. The general increase in α with
increasing jet multiplicity , as shown in Figure
5.5, is also consistent with the α increase as we
switch from the single particle trigger (which has a
jet multiplicity of 1) to the jet trigger.

In Figure 5.7, we plot α vs. the charge of
the trigger jet. We do not see any significant
difference between the positively charged and the

negatively charged jets. The larger α value for jets of larger absolute charges is probably just a reflection of the multiplicity effects shown above (i.e. large net charge implies large multiplicity).

The multiplicity is a rather crude average characteristic of the event. We shall discuss in more detail the event structure of interactions off the aluminium target in the later chapters.

5.5 TESTS FOR THE RELIABILITY OF OUR DETERMINATION OF α

A charged particle with laboratory momentum (p_x, p_z), coming from the center of our hydrogen target ($z=1.7$), will hit the calorimeter roughly at the x-coordinate:

$$X_{int} = \frac{10.8 \ (p_x \pm .28)}{p_z} \qquad (5.4)$$

The apparent p_x change (Δp_x) of order .28 comes from the momentum kick (.379 Gev/c) imparted by the magnetic field roughly at $z=4.5$.   This is illustrated in the following figure (see trajectory H1) :
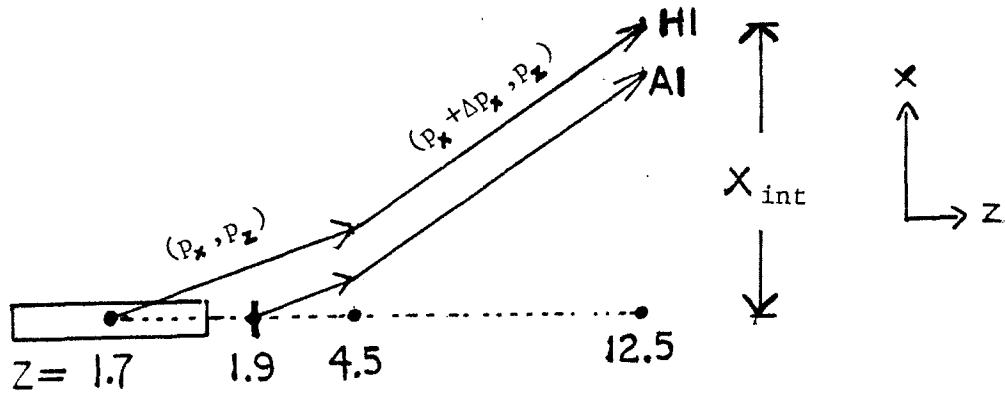
Fig. 5.8a   Trajectories of charged particles in MPS

A charged particle, with the same kinematic parameters but coming from the aluminium target, takes the trajectory Al which is parallel to Hl (see the above figure). When we trigger our experiment, we calculate our triggering $p_\perp$ at the calorimeter ($z=12.5$) using the detected X_{int} , assuming that the particle comes from the middle of the hydrogen target ($z=1.7$). This means for interactions off aluminium, the value of Δp_x mentioned above will be different by a tiny amount $.02p_x$ from $.28$. If we assume the p_x spectrum is $\exp(-3p_x)$, and let us take mean p_x = 500 Mev/c, this tiny change in

Δp_x can easily contribute a 2% acceptance
difference between the 2 targets for jets triggered
below the threshold. of course this is only a
trigger bias and will not affect data above
threshold which is analyzed offline with the correct
vertex.

In the real situation, the sign of this
apparent change Δp_x can be either positive or
negative. Since we are studying here a sharply
falling spectrum, the configuration shown in Figure
5.8a is more dominant.

In order to show that there are no serious
magnet biases, we plot, in Figure 5.9, α as a
function of the following variable:

$$f_{mk} = \frac{.379 \ (\text{JET CHARGE})}{\text{JET } p_\perp} \qquad (5.5)$$

The sign of f_{mk} indicates whether the magnet kick
favours or acts against the jet trigger. Its
magnitude is a measure of the fractional change in
p_x due to the magnet kick (The actual change in
p_x is given in (5.4)). We see no significant
difference in α between the positive and negative
values of f_{mk}. This shows that our results are not

affected by the magnet kick.

For the minimum bias data, the magnet kick has a slightly different effect on the triggering efficiency. This is illustrated in the following figure:
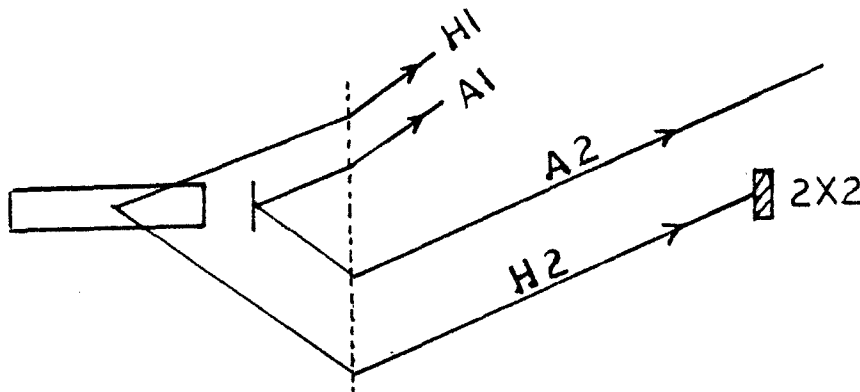
Figure 5.8b   Effect of magnet bend for
                Interacting Beam triggers

The amount of bending in the magnet for 200 Gev beam particle is negligible in comparison with the bend for other lower momentum particles and so we can assume, for simplicity, that the 2"X2" counter is centered on the beam line. Most of the particles in our interacting beam sample have momenta much less than 100 Gev/c. Therefore, the only way, that lower

momentum particles can hit the 2X2 counter is by

bending in the opposite direction to the x-component

of their momenta (trajectories H2 and A2 in Figure

5.8b). In this bend-in configuration, a charged

particle coming from the hydrogen target can be

vetoed more easily by the 2X2 counter. The order of

magnitude of this effect is related to the

difference in X_{int} mentioned above. A similar

rough estimate (like the high $p_\perp$ trigger) can easily

explain the 2% effect (for the interacting beam

trigger) observed in section 5.3. We shall talk

about the 2X2 problem again when we discuss the

forward region later in Chapter VI.

As illustrated in Figure 5.3, α increases with

$p_\perp$ for our high $p_\perp$ jet trigger. Any random

background, like that due to halo particles, should

have a smaller value for α . This means the

magnitude of α within a fixed $p_\perp$ range can be used

to indicate the cleanliness of our data. From a

study of the trigger side versus the away side, we

believe our neutral fraction cuts have already

cleaned up our data sufficiently (section 4.2) . We

justify this cut further by plotting the hadronic

neutral fraction versus α before any other cut in

Figure 5.10 . These plots clearly show our hadronic
fraction cut of .4 was a sensible choice for
removing most of the backgrounds. Thus α is flat
for neutral fraction less than 0.5 (indicating no
significant background) but dips above this.
Presumably most of the high neutral fraction data,
really come from lower $p_\perp$, where α is smaller and
is promoted by either the calorimeter fluctuations
or halo particles.

5.6 INTERPRETATION OF THE ANOMALOUS VALUES FOR α

After all these checks and justifications, we
are convinced that there is indeed a huge ANE for
high $p_\perp$ productions off aluminium. This effect is
also more prominent for the proton beam than for the
pion beam. We are not aware of any detailed
theoretical models with which we can compare our
results and use to make reliable estimates.
Instead, we shall discuss some of the qualitative
features of these theoretical attempts :

A.   Scatterings before the Main Interaction
      One possible explanation for this anomalously

high α is multiple scatterings inside the nucleus.
If it is due to scattering of the beam before the
main interaction, it has the same effect as if the
target nucleon has some kinetic motion (Fermi
motion) during the interaction. This can either
raise the effective c.m. energy ($\sqrt{s}$) or give a net
$p_\perp$ kick to the interacting system. The possibility
that effective s is increased is very unlikely,
since it has been observed (Figure 5.11 taken from
Ref. [1.15]) that the p/π production ratio increases
with A but decreases with s, at least in the case of
the single particle trigger. How about the
possibility that this is due to some additional
$p_\perp$ added for the nuclear target? As the high
$p_\perp$ cross section behaves like $\exp(-3p_\perp)$, the
contribution to α for any nuclear target will be
around $0.9 k_F^2 / \ln(A)$ where k_F is the maximum $p_\perp$, due
to the Fermi motions, that can be added to the
nucleon. If we take $k_F = 200$ Mev/c, then we shall
have $\alpha = 1.01$ for the aluminium target which is
obviously too small to agree with our results. The
p/π production ratio for the single particle trigger
also does not agree with such an explanation (see
Fig. 5.11). Let us assume that we do not know how
to estimate such effect and this large α is still

caused by some effective $p_\perp$ kick . This implies that a jet with transverse momentum $p_\perp$ produced off the aluminium target should behave like a jet with transverse momentum ($p_\perp$ - .2) produced off the hydrogen target. In Figure 5.12, we plot the charged multiplicity in the jet as a function of $p_\perp$ for both targets. We observe a large difference in <N> (mean charged multiplicity in the jet) between these 2 targets, and such a difference can not be explained by a general $p_\perp$ shift of .2 Gev/c (at least $\Delta p_\perp = 2$ is needed). There is essentially no observed difference in jet multiplicity between proton and pion interactions, while there is a significant difference in α between these 2 beams. Thus fermi motion can be ruled out as an important contribution to the anomalous value of α .

B.   Nuclear Effects During the Main Interaction

Since we are dealing with a high density of nucleons in collisions off nuclear targets, some people have suggested that many nucleons may act coherently in such interactions (see discussion of the "Coherent tube model" in Ref. [1.18a]). This means the interaction time must be of order of the size of the nucleus, and it may contradict the

general belief that the high $p_\perp$ interactions are
related to the deep underlying hard (short distance)
scatterings of the asymptotically free partons.

C.   Additional Interactions of the Final State

Some theorists believe that this $\alpha > 1$ phenomenon
is due to additional hard scatterings after the main
one.   They suggest formalisms [1.18b] like :

$$\frac{\sigma_A}{\sigma_{HY}} = A(c_0 + c_1 A^{\frac{1}{3}} + c_2 A^{\frac{2}{3}} + \ldots\ldots \qquad (5.6)$$

where c_0, c_1, ... are some free parameters and A
is the atomic weight.   Additional soft scatterings,
or multiple scatterings, of the final state after
the main interaction can also give rise to such
effects.   If such secondary scatterings can enhance
an increase in $p_\perp$ without changes in jet
multiplicity, then the large α differences seen
between jets and single charged particles will be
very hard to understand.   In a recent publication
[1.20], it is shown that multiple scattering may
enhance the high $p_\perp$ gluon production in nuclei.
Such mechanism can be used to explain the strong
dependence of α on the multiplicities and many
other observations.   Unfortunately, some of the
assumptions used in Ref.   [1.20] are not fully

justified [1.18] and therefore their quantitative
results are probably not credible. No matter how
the final forms of such models may look, we believe
it is probably still very hard to explain the large
difference in α between proton and pion beams while
still predicting that their jet multiplicities are
almost the same.

D.   Background Smearing

    It is possible that the difference in
α between the proton and pion beams is related to
the sharper slope of the proton beam high
$p_{\perp}$ spectrum. It has been observed ([1.7d], [1.13]
and Fig. 4.3a) that the relative jet production off
hydrogen by the proton beam compared to the π beam
decreases from 1.5 to .5 (a factor of 3) between
$p_{\perp}$ = 2 and 6 Gev/c. The difference $\Delta\alpha$ = .2 between
proton and pion in Fig. 5.3 corresponds to the
proton/pion ratio changing not by 3 but rather by
1.5 off an aluminium target. If one imagines that
the nuclear jet cross section is obtained by
smearing (of whatever kind) of the hydrogen data,
one will always smear the sharper cross section more
and so find a larger value of α for it.

One smearing effect in any jet experiment is due to additional low $p_{\perp}$ particles that happen to be in the cone defining jet although, in fact, they may come from the beam or target fragmentations. This smearing is more pronounced for the aluminium compared to the hydrogen target as the former has a substantially higher multiplicity at zero rapidity (see Figures 6.12 to 6.14). We investigated this effect by generating random particles in the C.M. rapidity range -.5 to .5 with equal probability to be plus, minus or zero charges. The $p_{\perp}$ distribution used for the random particles was a Gaussian with a mean $p_{\perp}$ equal to 330 Mev. We added these extra particles to our hydrogen data and analyzed these modified data just like our original hydrogen data. We repeated this "particle adding" process until the mean charged multiplicity in the jet from our modified hydrogen data agreed with the aluminium data. The addition of 2 to 3 particles gave the best fit, and the away side rapidity distribution also seemed to agree for this choice. We found that this smearing contributes about .15 to the anomalous α value reported in Figure 5.3, but it did not appear that it can explain the difference of about .5 between the jet and single particle

α values. There is some difference between proton
and pion beams in our "particle added" results, but
it is much too small.

The single particle result published by the
Chicago-Princeton group [1.15] shows that the
α value for the proton final state is usually
larger than that for pions; our data seem to
indicate that the proton beam can enhance nuclear
anomalies more easily than the pion beam (see also
later chapters on target comparisons of the event
structure and the jet composition) . These
observations could be related to the larger total
cross section for protons, or the sharper proton
beam high $p_\perp$ spectrum, while the single particle
results may be sensitive to protons knocked out of
the nucleus. However the current estimates of the
effects mentioned above are all too small to explain
the observations quantitatively. We believe that
the current theoretical models can not predict the
large enhancement of jet production off nuclei seen
in our data.

CHAPTER VI

CORRELATIONS

6.1 GENERAL FEATURES

It is generally believed that jet production interactions are related to the underlying scattering of partons in the colliding hadrons. If such underlying hard collision is truly elementary and the transverse momenta of the jet fragments are limited, then the event structure of such interactions should be very coplanar. It has been shown in our previous publications [1.7] that the structure of particle distributions in jet events is much more coplanar than that of some isotropically produced particle distributions. Without further discussion of this coplanarity problem, we define the C.M. Jet Frame to be the center-of-mass frame with its x-axis pointing along the transverse projection of the jet momentum.

TRANSVERSE COMPONENTS

TRIGGER SIDE

AWAY SIDE
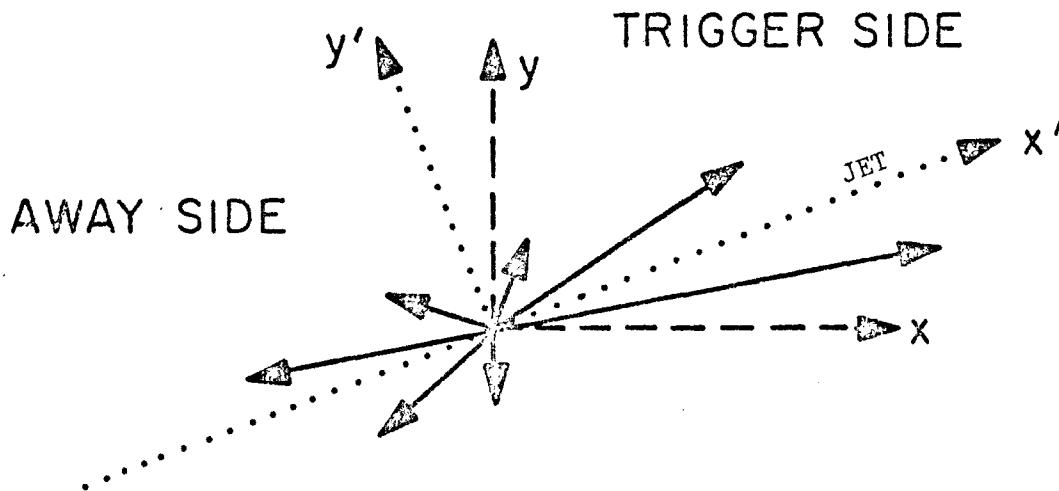
$\longrightarrow$ CHARGED (OR CHARGED AND NEUTRAL)
TRANSVERSE MOMENTUM VECTORS

$---$ FIXED AXIS x, y

$\cdots\cdots$ THE AXES x′, y′ FOUND FOR EACH EVENT

THESE AXES ARE USED TO DEFINE THE C.M. JET FRAME

We shall always present our results on the associated charged particle distributions in this frame unless it is specified otherwise.

The multiplicity density function D(X) used in this thesis is defined by :

$$D(X) = (dN_Q/dX)/(\text{number of events}) \qquad (6.1)$$

where X can be any kinematic variable, like $p_\perp$ or Y (rapidity) in the C.M. Jet Frame, and dN_Q is the number of charged particles within the kinematic region dX. D(X) is also called as ρ(X) in some references.

The first kinematic variable we would like to discuss is θ_{xz} , where $\tan(\theta_{xz})=p_x/p_z$ in the "C.M. Jet Frame". Ideally, θ_{xz} is independent of the measured energy of the particle. In reality, if we assign a wrong mass to a particle (we assume a pion mass for all particles) in the laboratory frame, our θ_{xz} which is calculated in the center of mass frame will be slightly distorted by an incorrect Lorentz transformation. We believe that this is a small effect, since most of the particles are believed to

be pions (see the Cerenkov counter studies in other theses [1.9]).

One nice thing about the θ_{xz} distribution is that it gives us an overview of particle distributions in all 3 regions: the away side region ($\theta_{xz} < 0°$), the forward region (θ_{xz} near $0°$), and the same side region ($\theta_{xz} > 0°$). The particles in the jet are in the region $50° < \theta_{xz} < 130°$, centered at $90°$.

These θ_{xz} plots are presented in Figures 6.1a to 6.1f for all charged particles with C.M. energies (E) greater than .5 Gev.

In Figure 6.2, we make a similar plot for particles with $E < .5$ Gev. It does not show any significant structure. Most of the interesting features of the jet events are probably due to higher momentum associated particles. Our $E > .5$ Gev cut seems to be very reasonable.

None of these θ_{xz} plots are corrected for acceptance. We shall present our results in terms of ratios when we compare our results for different beams and targets so that the acceptance will be cancelled out.

Our track finding efficiency is around 95%, and
from our Monte Carlo study, the 2X2 problem (which
will be discussed more later) only affects particle
around the region $|\theta_{xz}| < 15^\circ$ for $E > .5$ and is about
a 4% loss in this region. Within the uncertainty of
these effects, we can still discuss some of the
general features of these plots:

A.   There is a peak at 90°. It increases with $p_\perp$.
This was also indicated by the jet multiplicity plot
which was presented in Figure 5.12. The width of
this peak is about 20° which is smaller than the
size of our calorimeter (about 30°) and the cone
angle (40°) used in our jet definition. This is an
indication that our jets are not biased strongly on
the size of our calorimeter. We shall talk more
about particles in the jet in Chapter VII.

B.   The peak in the forward region is not centered
at 0°. It is roughly at -10°. It tends to shift
to more negative values at higher jet $p_\perp$ (see Fig.
6.1e). This phenomenon of a bias to the away side
is more pronounced for the $\bar{\pi}$ beam than the proton
beam (compare Fig. 6.1e with Fig. 6.1a). The
height of the forward peak also decreases with the

increasing jet $p_{\perp}$. The theoretical interpretation
of these observations will be discussed later in
section 6.2.

C.   There is no clear separation between the
forward peak and the "away side jet" region. For
$-60° < \theta_{xz} < 0°$, the multiplicity is higher than
the corresponding toward side $0° < \theta_{xz} < 60°$.
Further, the total multiplicity in the region $-120°$
$< \theta_{xz} < -45°$ increases with the increasing jet $p_{\perp}$;
this can be considered as an indication that the
dynamics of the "away side jet" dominate within this
θ_{xz} ($-120°$ to $-45°$) range. The general structure of
the away side is dependent on the beam and target
types as we shall discuss in the later sections.

In Figure 6.3, we also present a θ_{xz} plot for
data simulated by our Monte Carlo program. These
Monte Carlo data are analyzed identically to the
real data. Our Monte Carlo program uses the gluon
and quark scattering model developed by FFF; the
quarks and gluons are fragmented into hadrons using
a model developed by Field and Feynman [1.6].
Unfortunately, FFF does not have any detailed
prediction about the forward region. The assumption

we made in our Monte Carlo program is that the
remaining parts of the hadrons fragment like single
quarks (after the main hard collision).   The
flavours of these quarks are picked, in such way,
that on the average, the total flavour of the final
4 jets equals the flavour sum of the incoming
hadrons.   The program does not require the
conservation of quantum numbers on an event by event
basis.

A detailed comparison of the FFF with our data,
and a more thorough discussion about the Monte Carlo
program, will be presented in another thesis [1.9].
I shall only discuss some of the general features of
Fig. 6.3.   The Monte Carlo calculation shows a very
similar structure to our real proton data (Figure
6.1a).   It also exhibits about the same shift in the
peak (to about -10°) of the forward region shown in
the real data.   However, the Monte Carlo data have a
larger enhancement around -90° (on the away side)
at lower $p_{\perp}$ (2 to 3), and the forward peak also
decreases slower with increasing $p_{\perp}$.   These indicate
that we are probably observing more smearings
between the forward region and the away side than
expected in the FFF model.

6.2 FORWARD REGION

Before we discuss other correlations, we would
like to give more details on the forward region. As
we have described in Chapter II, all our triggers
have the pretrigger requirement which is defined by
the absence of charged particles in the 2X2 counter.
This creates a hole in our acceptance function in
the forward region. This hole is also shifted and
distorted by the magnet bend. The real situation is
even more messy. It is known that our spark
chambers have long memory times such that we have
"ghost" particles in the beam region left over from
the previous events. There are also "ghost" tracks
from beam particles that did not interact (remember
only 5% of the beam interact). These "ghost" tracks
can be matched easily to other good tracks around
the 2X2 region. This is mainly due to the high
density of tracks (ghost or real) in the forward
region. As we have discussed in section 3.1, the
algorithm for our track finding is to find all
tracks in the x and y views separately, then use
hits in the skew chambers (most of these are spark
chambers after the magnet) to match these tracks to
form particles. Whenever, there is a high density

of tracks, it is very likely to have tracks
mismatched (good with bad, bad with bad) to form
"fake" particles. The problem is accentuated by the
small angle stereo (tan θ =0.1) in the spark
chambers. Most of these "fake" particles have
already been removed by our preliminary pattern
recognition clean ups (see section 3.1 and [3.2]).
However, in the very forward region, we have so many
"ghost" tracks that it is necessary to make stricter
cuts for particles in the forward region. The
number of left over bad tracks can be significantly
reduced by making cuts on PWC (the PWC's have a
smaller memory time [2.1] than the spark chambers)
quality factors that are based on PWC hits only, and
by removing tracks that go into the 2X2 or close to
it. In fact, we made all these cuts [3.4] before
our final analysis. The problem is that the net
track finding efficiency in the forward region is
clearly reduced by these cuts.

In order to show that our forward region cuts
are efficient in removing these "ghosts", we plot
the particle distribution in the spatial x-y space
before and after cuts. We saw a cross shape (Fig.
6.4a) centered at the 2X2 before any cut. These are

a combination of truely "ghost" particles and real
tracks mismatched to "ghost" tracks. After some PWC
quality cuts, this cross structure vanishes and the
2X2 hole starts to appear (Fig. 6.4b). We then
just remove the remaining ghost particles that "hit"
the 2X2 and some particles very close to it.

The main problem for the forward region is in
fact how to estimate the efficiency after all these
cuts. We can, of course, avoid the problem by just
computing ratios. However, it is still very
important to know roughly the size of such losses
and which kinematic regions are affected by these
losses. Our Monte Carlo program allows all
particles in the forward region-including particles
that go into the 2X2 counter. By imposing our cuts
in the forward region on the Monte Carlo data, we
can thus estimate the fractional losses due to our
software cuts and the anti-2X2 triggering system.
In Figures 6.4c and 6.4d, we plot the fraction of
particles lost in our Monte Carlo data as a function
of θ_{xz} for all particles with $E > .5$ Gev. We find a
maximum fractional loss of around 4% in the forward
region. Our Monte Carlo program is not
sophisticated enough to be able to estimate

correctly some of the losses due to all the quality
cuts, the real loss is probably slightly higher.

We can also estimate the 2X2 losses using the
real data. This is illustrated in the following:

consider a particle with a definite value for
p_x (x-component of its momentum) in the C.M. Jet
Frame. Its acceptance as a function of p_x has a
hole roughly in the region:

$$p_{xL} < p_x < p_{xH} \qquad (6.2)$$

where $\quad p_{xL} = -.25(\ 2x\ +\ Z_1(1-Z_2 x)\ ) \qquad (6.3)$

$\qquad\quad p_{xH} = \ .25(\ 2x\ -\ Z_1(1-Z_2 x)\ ) \qquad (6.4)$

$\quad x\ =$ (laboratory momentum)/(200 Gev/c)

$\quad Z_1 =$ (charge of the particle)X(sign of

$\qquad\qquad$ the magnet kick in the C.M. Jet

$\qquad\qquad$ Frame)

$\quad Z_2 =$ (charge of the particle)X(charge

$\qquad\qquad$ of the beam)

where the quantity Z_1 indicates whether the charged
particle is bent towards the trigger side or away

from it, while Z_2 indicates whether the charge of the particle is the same as the incoming beam particle or not. The values of p_{xL} and p_{xH} also depend slightly on the vertex position as mentioned in Chapter V. A vertex z position = 1.7 is assumed in this simple illustration.

A plot of x (defined above) indicates that we have very few particles for x >.35. This is expected from the conservation of the total momentum as the maximum possible total energy in the C.M. frame, in the forward region, is around (10 - (jet $p_\perp$)) which corresponds to x =.5 for jet $p_\perp$=5 Gev/c.

The acceptance function (due to 2x2 losses) as a function of p_x in the C.M. Jet Frame is sketched in the following figure for two values of x :

Figure 6.5 Acceptance (2×2 loss only) as a function of p_x. x is defined in section 6.2.

Acceptance function

p_x in Jet Frame (Gev/C)

a) x=o.1
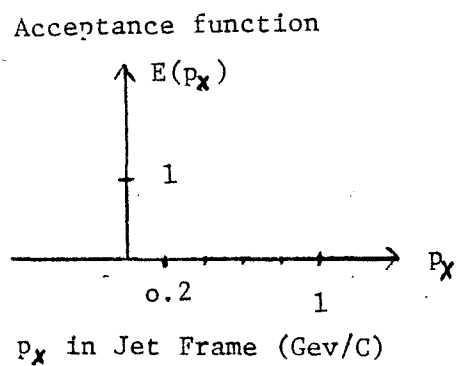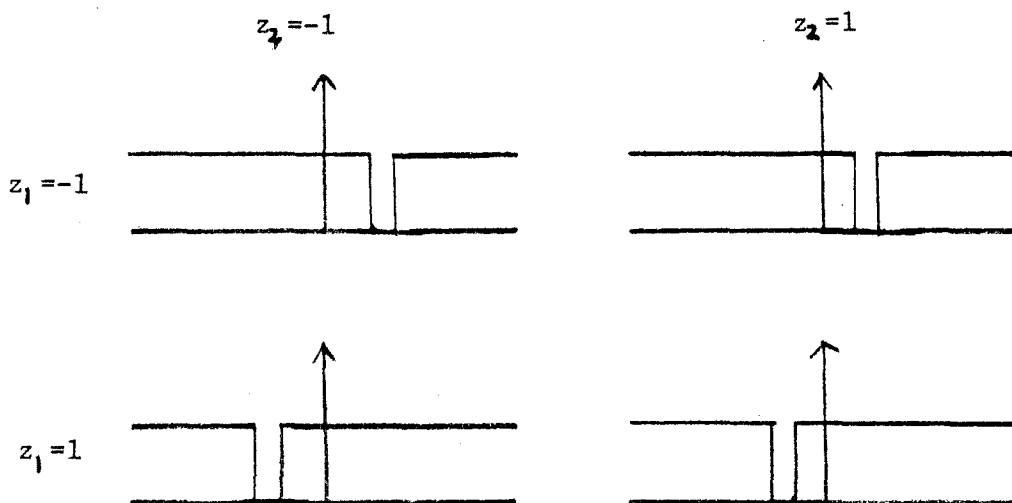
b) x=o.35
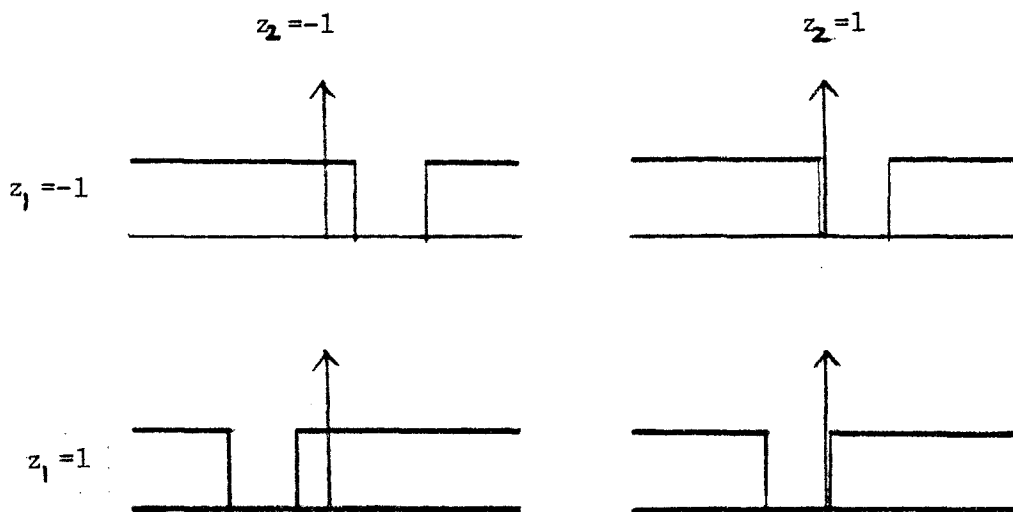
The interesting feature about the 2X2 loss is that
these holes (in the acceptance function) do not
overlap (see Figures 6.4c and 6.4d) for different
magnet kicks (different Z_1) if x is small enough and
if the charge is fixed (fixed Z_2). This means we
can also estimate our efficiency by comparing the
distributions for different magnet polarities for
the region x< 0.33 which in fact includes most of
our data. A preliminary estimate using this
algorithm indicates that the 2X2 loss is around 5%
for E > 0.5 particles. The final analysis of the
2X2 efficiency is not completed at the time of this
report.

The forward region contains a lot of
interesting physics connected with the beam jet. We
have already shown that the forward peak tends to
move away from the trigger side as $p_{\perp}$ increases.
Theoretically, such a tilt is related to the
transverse momentum of a quark or gluon inside the
hadron. A more thorough analysis will be attempted
on our data (in the forward region) in the near
future. So far, most of our results on the forward
region studies are preliminary. The current data
are however sufficient for a comparison of hydrogen

and aluminium targets. The main purpose of this
section is to discuss problems associated with the
2X2 counter and possible ways of solving it.

6.3 CHARGE CORRELATIONS

As we have shown above, the loss due to the 2X2
veto is probably around 4% level in the forward
region, and for lower x values such losses are
almost independent of the particle charge (see
Fig. 6.5a above and also $|\theta_{xz}| > 10^o$ in figures 6.4c
and 6.4d). We can therefore study the ratio of
positive to negative charged particle production
with a maximum uncertainty of order 4%. This +/-
ratio is plotted as a function of θ_{xz} in Figure
6.6 for various values of the jet charge (Q_{JET}),
where Q_{JET} is the sum of the charges of particles
in the jet, requiring that these particles must have
p_x's greater than .1 of the jet $p_\perp$. The mean $p_\perp$ of
the jets for all these plots are listed in Table
6.1. I have also plotted these ratios for various
$p_\perp$ bands (within 2 to 6.5) but I do not show them
here as the different $p_\perp$ cuts all looked very
similar.

In Figure 6.7, I make a similar plot using our
Monte Carlo data. Although the quantum number
correlation in the forward region is handled
incorrectly in our Monte Carlo program, the
correlation on the away side still represents what
is expected from the FFF model. It is believed that
there should be very little correlation between the
+/- ratio on the away side and the various values of
Q_{JET} . This comes naturally from the assumption
that the underlying scattering is elementary and the
scattered partons fragment independently. Such
assumptions also lead to large quantum number
correlations between the forward region (the beam
jet) and the triggered jet. Of course, there are
always smearings between these 3 regions due to
uncertainties in the dynamics of the low momentum
particles. Our E >.5 Gev cut should have removed
most of this smearing.

When we try to compare our proton beam data
(Figure 6.6a) with what is expected (Figure 6.7) on
the away side, we observed significant difference
(between the two plots). The theory predicts a
smaller correlation than seen in our data. For the
pion beam data, we expect some correlations on the

away side due to asymmetry of the beam target
system, while we observe about the same amount of
correlations as in the proton data. It is possible
that all these observed discrepancies between the
data and the theory are due to the approximate
handling in the model of the transverse momenta for
quarks in the hadron or the omission of other
processes. Naturally it is important to study the
origin of this correlation of the (average) quark
charges both theoretically and experimentally.

Although we believe that our data (used for the
final analysis) are very clean, we would still like
to make some more checks on our +/- ratios. As I
have discussed above, most of the ghost tracks
should have fewer hits in the PWC's. This means
their PWC quality factors should have lower values
than for the real tracks. We divided our data into
two samples based on a cut of the total PWC quality
and we plot the +/- ratios for these two samples in
Figure 6.8. We see no difference between the two
even in the forward region (Notice this is not
completely precise as the PWC quality factor can be
slightly momentum dependent and so a momentum
dependence of the +/- ratio could show up in

Fig. 6. 8). It is important to note that the ghost

particles usually have the same charge sign as the

beam particle (they "were" beam particles). Any

excess of ghost tracks should show up as larger +/-

ratio, in the forward region, for the lower quality

particle sample in Fig. 6. 8. (Note that we only use

the positive beam polarity in this plot). The fact

that there is no difference in the +/- ratio between

these 2 samples (of different qualities) for all

values of θ_{xz} indicates that our final data (after

all cleanliness cuts) are probably very clean.

6. 4   BEAM COMPARISON

In order to study the effect of incoming beam

types on the structure of a jet event, relative

$D(\theta_{xz})$ plots for different beams are presented in

Figures 6. 9 and 6. 10 . We observe no differnce

between the π^+ and π^- beams (Figure 6. 9b has very low

statistics). All these plots in Figure 6. 9 are

consistent with 1 for all values of θ_{xz} . Figure

6. 10 is much more interesting. These plots indicate

that the away side θ_{xz} distribution for the pion

beam interaction tends to shift more towards the

forward region than the proton beam interaction.

This is expected in the theory as the pion has one

less valence quark than proton, and therefore the

scattered parton from the pion is more likely to

have a higher p_z in the C. M. frame (see discussion

in Chapter I). This forward shift, for particles in

the pion beam interaction, seems to increase with

the jet $p_\perp$. This observed variation with increasing

$p_\perp$ would be obviously statistically significant if

we combine some of the bins (like those from $-80°$ to

$-20°$) to show more clearly the difference between

the lower $p_\perp$ (2 to 3) jets and the rest. One of the

amazing results from our experiment is that we see

no obvious difference between Figures 6.10a and

6.10b. If we believe this forward shift of the pion

beam relative to the proton beam is a manifestation

of the underlying QCD dynamics, then it seems that

the nuclear effects (which could a priori easily

smear such dynamics) are all cancelled neatly in

Figure 6.10b.

In Figure 6.11 , we plot the relative D(z)

distribution (proton over $\bar{\pi}$ beam) for all charged

particles on the away side ($p_x<0$). z is defined as

the absolute value of p_x in the C. M. Jet Frame

divided by the jet $p_\perp$ (or $p_\perp$ of the triggered

particle in single high $p_\perp$ trigger). We find that

the pion interaction has slightly more higher z

particles on the away side for the hydrogen target

and this effect seems to be larger for the aluminium

target. This large z enhancement for pion beams is

not completely unexpected as the scattered parton on

the away side, in pion interaction, can be detected

more easily by our spectrometer due to the forward

shift effect discussed above.

6.5 COMPARISON OF ALUMINIUM AND HYDROGEN TARGETS

For the comparison of different targets, we

will use the kinematic variable Y (rapidity) instead

of θ_{xz}, as Y is the variable used more often in

previous publications. Figure 6.12 shows some

published results taken from Ref. [1.18a]. We

make similar plots of the relative D(Y) (aluminium

over hydrogen) distributions for all charged

particles (except that in the single high

$p_\perp$ trigger, the trigger particle is excluded) for 3

different triggers (Figure 6.13). They all seem to

have very similar structures. In Figure 6.14, we

repeat these relative D(Y) distribution plots for
all charged particles on the away side only.
Figures 6.13 and 6.14 are almost identical to each
other , except maybe, for regions near Y=0. We make
no energy cut for particles included in these plots.
The shape of these relative D(Y) distributions in
the lower Y regions could be mainly due to low
momentum particles (E <.5 Gev). The effect of
energy cuts like E > .5 Gev is still to be studied.

We now make some checks on our relative D(Y)
plots. In Figure 6.15. we present the D(Y)
distributions for the aluminium target and 3
different vertex regions of the hydrogen target. We
do not see any vertex (spatial) dependence of D(Y)
for interactions off hydrogen. They are all well
separated from the aluminium target D(Y)
distribution in regions Y<.6, indicating that we do
not have any serious acceptance difference problem
in this rapidity region.

For the very forward region, the 2X2 problem
may affect D(Y) slightly. In order to justify our
results for all regions presented, we plot the
relative D(Y) distributions on the away side for the

following two classes of particles:

 (1)   not affected by the 2X2

 (2)   affected by the 2X2

    when I say "not affected by the 2X2" , I mean a
particle, on the away side, that is bent (by the
magnetic field) away from the 2X2 (see previous
figures and discussion on the 2X2 problems). If the
energy of this particle is low enough, then it will
never hit the 2X2 counter and its acceptance will
not be affected by the 2X2. The other class of
particles are those that are bent towards the 2X2,
their acceptance will always be affected by the 2X2.
These two classes of particles are labelled as
"outside 2X2" and "affected by 2X2" in Figure 6.16.
We cannot find any noticeable difference for the
relative D(Y) distributions between these two
samples. Our results on the relative D(Y)
distributions are thus probably quite independent of
any possible acceptance problems.

    It is generally believed that the shape of the
relative D(Y) distributions is related to the
propagation of the beam jet through the nuclear
matter (see discussion in Chapter I) both before and
after the main interaction. Unfortunately, there

exists no theory with which we can compare our results quantitively. I shall point out some of the general features of our plots without referring to any model:

(1) The shape of the relative $D(Y)$ (also called $R(Y)$) distributions is almost independent of trigger $p_\perp$ for events of a given trigger .

(2) There seems to be differences between the relative $D(Y)$ distributions for different triggers. $R(Y)$ in the $Y>0$ region decreases, for different trigger types, in the following order:

(all I.B.) > (single particle I.B.) > (single high $p_\perp$) > (jet)

where (A) > (B) means trigger A has the higher value of $R(Y)$ in regions $Y>0$ than trigger B.

These observations indicate that, maybe, $R(Y)$ is sensitive to the overall event multiplicity. If this is true, then we shall be wary of the multiplicity effects (like whether diffractive interactions are included) for such $R(Y)$ plots from any experiment.

In Figure 6.17, we plot the relative $D(z)$ (also called $R(z)$) on the away side for the 2 targets. We observe, in general for all $p_\perp$'s, more lower z particles on the away side for interactions off aluminium. At higher $p_\perp$'s (4 to 6.5 for jets and 3 to 5 for single high $p_\perp$ particles), interaction off aluminium seems to have less high z particles on the away side. We do not see any significant difference between the 4 plots in Figure 6.17, except may be, that $R(z)$ for the proton beam has a slightly sharper slope than the pion data at high $p_\perp$. $R(z)$, in general, decreases with increasing z. This decrease at large z is also observed for charged particles in the trigger jet as we shall discuss in the next chapter.

The observation that there is no significant difference in $R(z)$ distributions between the jet and the single high $p_\perp$ particle triggers is very interesting. Theoretically, the single high $p_\perp$ trigger is a subset of the jet trigger. We expect "similar" away side z distributions for these 2 triggers. When we say "similar", we mean they should be almost the same if the z of the single high $p_\perp$ trigger is multiplied by approximately 0.8.

This .8 factor is the mean z of the triggered single high $p_\perp$ particle in the jet whose fragmentation led to the the single high $p_\perp$ trigger particle. The similarity of R(z) for these two triggers indicates that this relation between the single high $p_\perp$ trigger and the jet trigger is not altered by the nuclear effects.

As indicated by plots presented in both this and the next chapter, interactions off aluminium have in general more low momentum particles than those off hydrogen. This leads naturally to the general expectation that there are probably additional nuclear scatterings of the final state (either hadron or parton) produced in the main high $p_\perp$ interaction . Figures 6.10 and 6.17 seem to indicate that such additional nuclear scatterings (if they exists) are probably very coherent with the main interaction , so the dynamics of the main interactions can still be seen. In our minimum bias interacting beam data, we also observe some correlations that seem to be unaffected by the nuclear scatterings. This is shown in Figure 6.18 which is a two body correlation plot from work done with the help of T. Tse [6.1] where the correlation

function R   is defined as follows :

$$R = \frac{\sigma \frac{d\sigma}{dY_1 \, dY_2}}{\frac{d\sigma}{dY_1} \frac{d\sigma}{dY_2}} \quad \text{for} \quad |Y_1| < .25 \qquad (6.5)$$

where Y_1, Y_2 are rapidities of charged particles.

Figure 6.18b is for all events, while Figure 6.18a is only for events with the total charged multiplicity greater than 6. In all cases, we observe no difference between the hydrogen and the aluminium targets. This indicate that the coherence indicated by the positive correlation (R positive) for Y approximately equals to 0 is not affected by the nucleus. It can be understood theoretically if we believe that the final hadrons are always produced outside the nucleus.

Our experiment is the first to study both high and low $p_\perp$ interactions off a nuclear target with a large kinematic acceptance. We have observed many interesting nuclear effects that were not predicted theoretically. This could be the starting point of a deeper understanding of nuclear effects in high energy collisions.

CHAPTER VII

JET COMPOSITION

7.1 RELATIVE Z DISTRIBUTIONS

As we have already shown in Figure 5.12, jets produced off aluminium are composed of more charged particles than jets off hydrogen. In this chapter we are going to make a further comparison of the jet structure between hydrogen and aluminium targets, and also between different beam types. The distribution function that we are going to discuss here is:

$$D(z) = (dN/dz)/N_{JET} \qquad (7.1)$$

where $z = (p_x$ of charged particle in the jet in the C.M. Jet Frame) / (jet $p_\perp$).
This $D(z)$ function has already been defined previously. z is also called as x_e in some publications.

For particles in the jet, $D(z)$ is usually interpreted as the parton (mainly quarks, with some gluons) fragmentation function in models (like that

due to FFF) where jets are produced by constituent
scattering. $D(z)$ is expected to approximately
scale, that is, be independent of $p_\perp$, although QCD
does predict a small $p_\perp$ dependence that has not yet
been seen experimentally.

In our previous analysis [1.7], $D(z)$ is found
to scale as a function of $p_\perp$ within the experimental
uncertainty. This scaling, especially at high $p_\perp$,
however, can be sensitive to the scheme of neutral
extractions. If we use the old neutral analysis
scheme as developed for our early data in [1.7],
such scaling is observed [7.1]. However, with the
present neutral scheme and "neutral cuts" described
in this thesis, scaling is no longer observed. This
indicates that details of neutral analysis
(especially the neutral cuts) may affect this $D(z)$
scaling in a non-trivial way. Whether this scale
breaking is really due to QCD corrections (or some
other theoretical effect), or is mainly an artifact
of the neutral cuts, is still to be studied.

Our Monte Carlo data, in general, have higher
$\langle z \rangle$ values than the real data, indicating that the
real data have probably more low z particles than

predicted by the FFF model.

With all these ambiguities about the absolute
magnitude of $D(z)$, we can still make a meaningful
study of the relative $D(z)$ for different beams and
targets.

We show the ratio of $D(z)$ for the π^+ beam over
that for the π^- beam in Figure 7.1 and $D(z)$ for the
proton beam over the π^- beam in Figure 7.2. The
ratios presented in all these plots are consistent
with 1. Due to limitations in statistics, we cannot
say anything very quantitative about Figure 7.1.
However, Figure 7.2 seems to indicate that the
proton data have slightly less high z particles than
the π^- data. This can be statistically significant,
for the aluminium target, if we combine the
$p_\perp$ ranges (3 to 4) with (4 to 6.5). We shall
discuss one possible explanation for this different
$D(z)$ phenomenon later in the next section.

In Figure 7.3, we have the relative $D(z)$
(called $R(z)$ from now on) of the aluminium target
over the hydrogen target. We observe here a similar
effect at large z (i.e., aluminium is lower than

hydrogen) as shown in the away side R(z)

distribution discussed in the last chapter. Such

effects seem to occur at even lower $p_\perp$ values for

particles in the trigger jet than for the away side.

7.2 CONTAMINATIONS FROM LOW $P_\perp$ PARTICLES

One possible explanation for this R(z) $\neq$ 1

effect (in both target and beam comparisons) is that

this is due to additional low $p_\perp$ particles that

happen to be in the cone defining the jet, although

in fact , they come, for instance, from the beam or

target fragmentations.

In order to understand this contamination

effect, we define for all charged particle in the

jet:

$$z_Q = \frac{z}{\sum_{z_i > z_{cut}} z_i} \qquad (7.2)$$

where i sums over all the charged particles in the

jet. We ignore cases where the denominator becomes

0. This parameter z_Q is really defined in such a

way that it behaves like the variable z for different triggers as we switch smoothly (by increasing ZCUT) from the jet trigger (no ZCUT) to the single charged particle trigger (ZCUT greater than or around .8). When we say there is "no ZCUT", we mean $z_Q = z$. The case for ZCUT=0 corresponds to the charged component of the jet.

In Figures 7.4 and 7.5, we combine the higher $p_\perp$ bands and plot $D(z_Q)$ distributions for various values of ZCUT's. The mean jet $p_\perp$ of these plots are listed in Table 6.1.

The proton over π^- D(z) plot (Figure 7.4a) was consistent with 1 originally (see Fig. 7.1a). The operation of using finite ZCUT has only a small effect on the ratio, although it does tend to make the ratio closer to 1. For the aluminium target (Figure 7.4b), the relative $D(z_Q)$ is definitely affected by the ZCUT. For ZCUT=.2, our relative $D(z_Q)$ has already become consistent with 1, while our old relative D(z) is about 20% below 1 at high z. Both of these plots seem to indicate that any slight difference in D(z) between proton and π^- beams can be due to low z particles.

On the other hand, this explanation seems to fail in cases of target comparisons. For both proton and $\bar{\pi}$ beams, ZCUT=.4 is still insufficient to make $R(z_Q)=1$ for all values of z_Q (Figure 7.5), indicating that things are probably more subtle here. However, these plots may still support possibilities like multiple scatterings of the jet fragments in the nuclear matter for interactions off aluminium. Comparisons of these plots with predictions of a reasonable theoretical model (let us hope there will be one) will be very intriguing.

CHAPTER VIII

SUMMARY AND CONCLUSION

8.1   SUMMARY

The Fermilab experiment E260 has three major triggers: jet, single high $p_\perp$ and interacting beam. This thesis reports on some of the recent studies on our data and emphasizes comparisons of two targets (hydrogen and aluminium) and three beams (π^-, π^+ and proton). Here is a summary of our results:

(1)   A jet is defined here as a group of particles going into either of the two calorimeters. Both our jet cross section and the associated particle distributions agree pretty well with the QCD predictions (FFF model).

(2)   We understand the problems associated with the 2X2 counter. Results on the forward region study is still very preliminary.

(3)   We observe a larger charge correlation than predicted by FFF between the +/- ratio on the away side and the charge of the jet.

(4)   Target comparison:

   a) $\alpha > 1$ at high $p_\perp$ for both jet and single particle triggers. The value of α for our proton beam single high $p_\perp$ data agrees with the Chicago-Princeton result. α depends strongly on multiplicity.

   b)   Interactions off the aluminium target have higher associated charged multiplicities in all regions except in the very forward region.   This could be due to the enhancement of gluon production in the hadron nucleus scattering.

   c)   If this higher multiplicity is caused by additional nuclear scatterings, than such additional nuclear scatterings are probably very coherent with the main interaction.   The two body correlation for all the associated charged particles, in our interacting beam trigger, is the same for both the hydrogen and aluminium targets.   This seems to indicate that the final hadrons are produced outside the nucleus.

(5)   Beam comparison:

a)   The results on π^+ and π^- beams are

essentially the same.

b)   Our proton data look different from the

pion beam; they have a slightly higher charged

multiplicity and the proton almost always

enhances nuclear effects (like larger α) more

than the pion .

8.2   CONCLUSION

(1)   Qualitatively, our data agree well with the

QCD predictions by FFF.   However, there are

indications of discrepancies especially when we try

to make some quantitative comparisons.   Both

theoretical and experimental studies are needed to

understand such discrepancies.

(2)   We are the first experimental group to study

nuclear anomalies with the detailed measurement of

the event structure.   Some of the qualitative

predictions suggested by the QCD theory for the

hadron nucleus scattering, such as, enhancement of

the gluon production and that the final

hadronization process is well separated from the main interaction, are all in good agreement with the data. However, it is still not clear that results like $\alpha > 1$ can be explained by the theory. We believe that the study of the hadron nucleus scattering is important in the investigation of many fundamental processes. Hopefully our results will stimulate further researches in this fascinating field.

REFERENCES

[1.1]   J. D. Bjorken, Phys. Review 179 (1969) 1547;

R. P. Feynman, Phys. Rev. Letters 23 (1969) 1415;

J. D. Bjorken and E. A. Paschos, Phys. Rev. 158 (1969) 1975;

R. P. Feynman, Photon-Hadron Interactions, Benjamin, New York 1972.

[1.2]   S. M. Berman, J. D. Bjorken and J. Kogut, Phys. Review D4 (1971) 3388.

[1.3]   B. Alper et al., Phys. Letters 44B (1973) 521;

M. Banner et al., Phys. Letters 44B (1973) 537;

F. W. Busser et al., Phys. Letters 35 (1973) 471.

[1.4]   G. Hanson et al., Phys. Rev. Letters 35 (1975) 1609;

G. Hanson, "$e^+ e^-$ Hadron Production and Jet Structure at SPEAR", Invited Talk at the 18th Int. Conf. on High Energy Physics, Tbilisi, GSSR, 1976, and SLAC-PUB-1814, September 1976.

[1.5]   R. D. Field, "Can Existing High Transverse

REFERENCES

Momentum Hadron Experiments be Interpreted
by Contemporary Quantum Chromodynamic
Ideas?", CALT-68-633 (1977);

G. C. Fox, "Application of Quantum Chromo-
dynamic to High Transverse Momentum Hadron
Production", CALT-68-643 (1978).

[1.6] R. D. Field and R. P. Feynman, Phys. Rev.
D15 (1977) 2590;

R. P. Feynman, R. D. Field and G. C. Fox,
Nucl. Phys. B128 (1977) 1;

R. P. Feynamn, R. D. Field and G. C. Fox,
"A Quantum Chromodynamic Approach for
the Large Transverse Momentum Produc-
tion of Particles and Jets", CALT-68-651.

[1.7] C. Bromberg et al., Phys. Rev. Lett. 38
(1977) 1447;

C. Bromberg et al., Nucl. Phys. B134
(1978) 189-241;

C. Bromberg et al., "Comparison of Hadron
Jets Produced by π and p Beams on Hydrogen
and Aluminum Targets", Proceedings of the
VIII International Symposium on Multipart-
icle Dynamics, page B89, Kaysersberg,
France, June 1977;

REFERENCES

G. C. Fox, "Recent Experimental Results on High Transverse Momentum Scattering from Fermilab", CALT-68-630 preprint (1977).

[1.8]   C. Bromberg et al., "Jets Produced in π^-, π^+, and Proton Interactions at 200 Gev on Hydrogen and Aluminum Targets", CALT-68-694;

C. Bromberg et al., "Structure of Events in 200 Gev Interactions on Hydrogen and Aluminum Targets at Low and High Transverse Momentum", in preparation.

[1.9]   M. Medinnis, UCLA, Thesis in preparation;

J. Rohlf, Caltech, Thesis in preparation;

R. Stanek, UICC, Thesis in preparation.

[1.10] P. Darriulat, in Proceedings of the 18th International Conference on High Energy Physics, Tbilisi, U.S.S.R. (1976), Edited by N.N. Bogolulov et al.

"Large Transverse Momentum Phenomena", ISR Discussion Meeting no. 21, March 7, 1977;

M. Della Negra et al., Nucl. Phys. B104, (1976) 429;

M. Della Negra et al., Nucl. Phys. B127, (1977) 1.

REFERENCES

[1.11] D. Sivers, S. Brodsky and R. Blankenbecler.
Phys. Reports 23C, 1 (1976).

[1.12] M. G. Albrow et al. , "Studies of Proton-
Proton Collisions at the CERN ISR with an
Identified Charged Hadron of High Trans-
verse Momentum at $90°$ I: On Forward Parti-
cles in High $p_{\perp}$ Reactions", CERN preprint
(1977);

D. Drijard et al., "Quantum Number Effects
in Events with a Charged Particle of Large
Transverse Momentum" (Part 1: Leading
Particles In Jets), Submitted to XIX
Int. Conf. on High Energy Physics, Tokyo,
August 1978, CERN/EP/PHYS 78-14.

[1.13] G. Donaldson et al., Phys. Rev. Lett. 36,
(1976) 1110;

M. D. Corcoran, Phys. Rev. Lett. 41 (1978) 9.

[1.14] U. Becket et al., Phys. Rev. Lett. 37
(1976) 1731;

J. W. Cronin et al., Phys. Rev. D11 (1975)
3105;

L. Kluberg et al., Phys. Rev. Lett 38
(1977) 670;

L. M. Lederman, in High Energy Physics and

REFERENCES

Nuclear Structure 1975, Amer. Inst. of Physics Conference Proceedings No. 26 p303.

[1.15] D. Antreasyan et al., Chicago preprint EFI 78-29, "Production of Hadrons at Large Transverse Momentum in 200, 300 and 400 Gev p-p and p-N Collisions".

[1.16] R. J. Glauber, Lectures in Theoretical Phyics, Vol.1 (1958), eds. W. E. Brittin and L. E. Dunham (Inter-Science, N. Y., 1959).

[1.17] A. Krzywicki, Phys. Rev. D14 (1976) 152.

[1.18] C. Bromberg et al., "Structure of Events in 200 Gev Interactions on Hydrogen and Aluminium Targets in both Soft and Hard Collisions", Caltech preprint CALT-68-725.

[1.19] W. Busza, "Review of Experimental Data on Hadron-Nucleus Collisions at High Energies VIIth Int. Colloquium on Multiparticle Reactions", Tutzing 21-25 June 1976, p545; A. Bialas, "Particle Production From Nuclear Targets and the Structure of Hadrons", preprint Fermilab-PUB-78/75-THY (1978).

[1.20] A. Krzywicki et al., "Does a Nucleus Act like a Gluon Filter?", Bielefeld preprint BI-TP79/14 (May 1979).

REFERENCES

[2.1]   A. Dzierba, E. Malamud, D. McLeod, "Multi-
        particle Spectrometer at Fermilab", report
        prepared for the Multiparticle Spectrom-
        eter Workshop. (Fermilab, March 4, 1977).

[2.2]   G. C. Fox and K. W. Yung, "Pseudo Data-Map
        Variables", Caltech memo CIT-31-76(1976).

[2.3]   E. Malamud, "The M6 Beam Line", internal
        report, (Feb. 1977) plus private
        communications;
        R. Beausoleil, "E250 Cerenkov Analysis for
        the M6 Beam", Caltech lunch seminar
        (April 12, 1979).

[2.4]   K. W. Yung, "Study of Pair Resolution in Y
        View", Caltech E260 memo (March, 1979).

[2.5]   H. Haggerty, "Multiparticle Spectrometer
        Calorimeters", Proceedings of the
        Calorimeter Workshop, page 251, Fermilab,
        May 1975.

[2.6]   K. W. Yung, "Calorimeter Handling Routines",
        Caltech E260 memo CIT-59-79(1977);
        K. W. Yung, "Geometric Parameters In The
        Calorimeter Handling Programs", Caltech
        memo CIT-60-79(1977).

[2.7]   W. Kropac, " Calorimeter Calibration

REFERENCES

from Beam Tracks", Caltech memo CIT-43-77 (may 11, 77).

[2.8] K. W. Yung, "Calorimeter Calibration with the Data", Caltech memo CIT-61-79 (Nov. 1977);

K. W. Yung, "Pulse Shape of a Hadron Entering Our Calorimeter", Caltech memo CIT-46-78 (Oct. 1, 1978).

[2.9] G. C. Fox, "E260 Normalization", Caltech memo CIT-40-77 (June 13, 1977).

[3.1] G. C. Fox, "State of Track Finding Message: 26April76; Subroutine ONEVU1 and FITLIN", Caltech memo CIT-14-75;

G. C. Fox, "State of Track Finding Message: 26April76; Subroutine MATCH1", Caltech memo CIT-16-75;

G. C. Fox, "Vertex Determination", Caltech memo CIT-25-76 (21April 1976);

K. W. Yung, " Scheme Used for Vertex Determination in (June76 to Sept76) Run", Caltech E110/E260 memo;

K. W. Yung and G. C. Fox, "E260 Track Finding Algorithm; Addendum-June25, 1977", Caltech memo CIT-37-77 (August 1976).

REFERENCES

[3.2]   K. W. Yung, "Subroutine LAUNDARY: Clean Up Results of Loose Track Findings", Caltech memo CIT-30-76 (1976).

[3.3]   K. W. Yung, " Curve Through Studies ", Caltech E110/E260 memo (Feb. 1976).

[3.4]   K. W. Yung, " A Preliminary Study of Track Qualities",Caltech memo CIT-48-78(July77); K. W. Yung," E260 Quality Factor Studies", Caltech memo CIT-62-79 (April 1979).

[5.1]   R.L. McCarthy et al.,   "Atomic Number Dependence of the Production Cross Section for Massive Dihadron States", Fermilab preprint Fermilab-Pub-77/102-EXP, Nov. 1977 and submitted to Phys. Rev. Letters.

[6.1]   T. Tse, "Comparison of Two-Particle Corre-lations For Hydrogen and Aluminum Events", Caltech memo CIT-55-78 (1978).

[7.1]   K. W. Yung,"Comparison of Jets from Hydro-gen and Aluminium Targets", Caltech memo CIT-47-78 (1978); K. W. Yung, "Observed Differences between Jets Produced by Positive and Negative Beams in E260", Caltech memo CIT-49-78 (1978).

TABLE 6.1: Mean jet $p_\perp$ for the following plots.
Cut used to define the $p_\perp$ range is $2 < p_\perp < 6.5$.

BEAM	TARGET	$<$JET $P_\perp>$ in Gev/c	FIGURE NUMBER	COMMENTS
Proton	Hydrogen	2. 94 + .006	6. 6a 6. 16b	HIJET
Proton	Aluminum	3. 14 + .010	6. 6b 6. 16b	HIJET
π^+	Hydrogen	3. 10 + .020	6. 6c	HIJET
π^+	Aluminum	3. 24 + .032	6. 6d	HIJET
π^-	Hydrogen	2. 96 + .005	6. 6e	HIJET
π^-	Aluminum	3. 11 + .009	6. 6f	HIJET
Proton	Proton	2. 90 + .004	6. 7	Monte Carlo
Proton	Hydrogen	2. 64 + .006	6. 16a	LOJET
Proton	Aluminum	2. 80 + .013	6. 16a	LOJET

a) Deep Inelastic Lepton-Nucleon Scattering
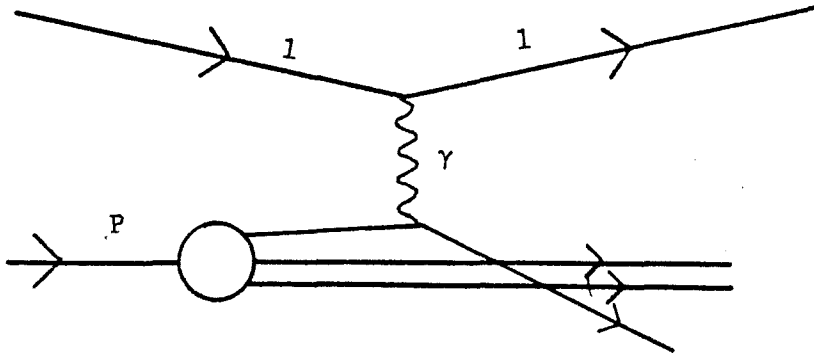
b) Lepton Pair Annihilation
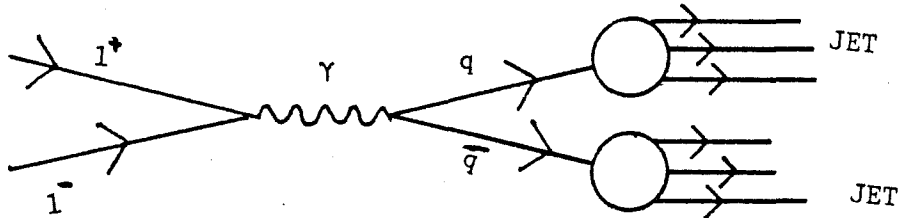
1 leptons
P nucleons
q quarks
γ photons

Figure 1.1

(a) Constituent Scattering

Either detect directly (Jet) or by fragmentation into single Hadron

q_a q_c

q_b q_d

p

p
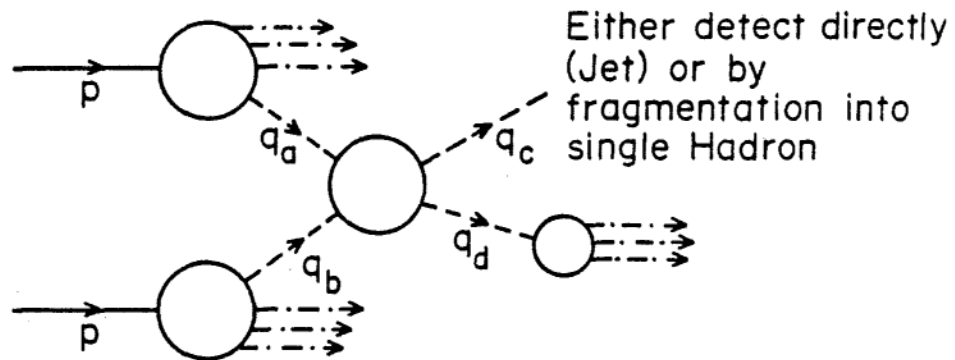
(b) Typical "QCD" Quark Quark Scattering

$g(Q^2)$ = running coupling constant

g

q   q

gluon

q   g   q

(c) 4-jet Structure of Events

Towards side

q_c

←Trigger particle

P_x

p   p

P_z

Away side

q_d
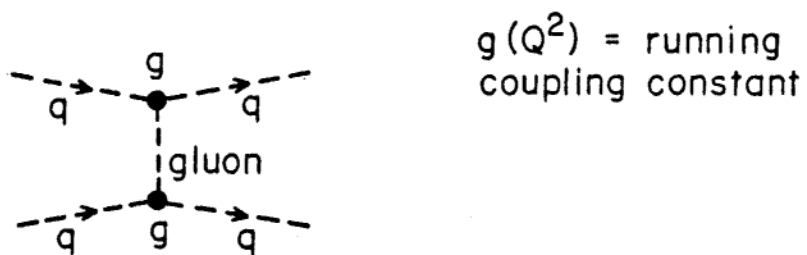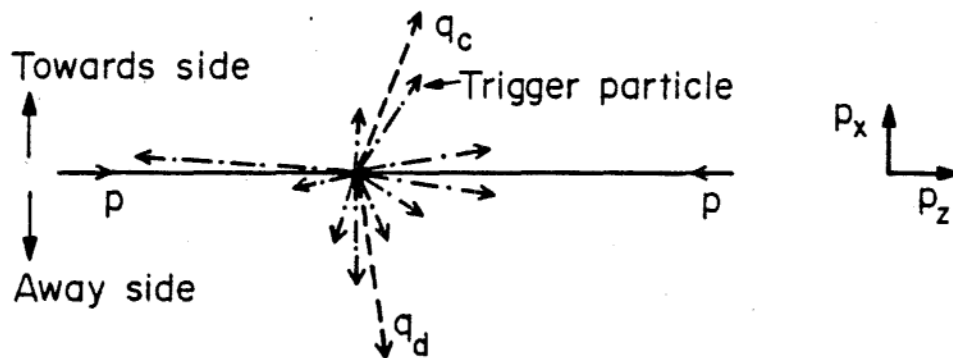
——→ Initial state Hadron

—·—·→ Final state Hadron

———→ Constituent (Quark or Gluon)

Figure 1.2

PLAN VIEW MULTIPARTICLE SPECTROMETER SUMMER 1976   BEAM ENERGY 190 OR 200 GEV
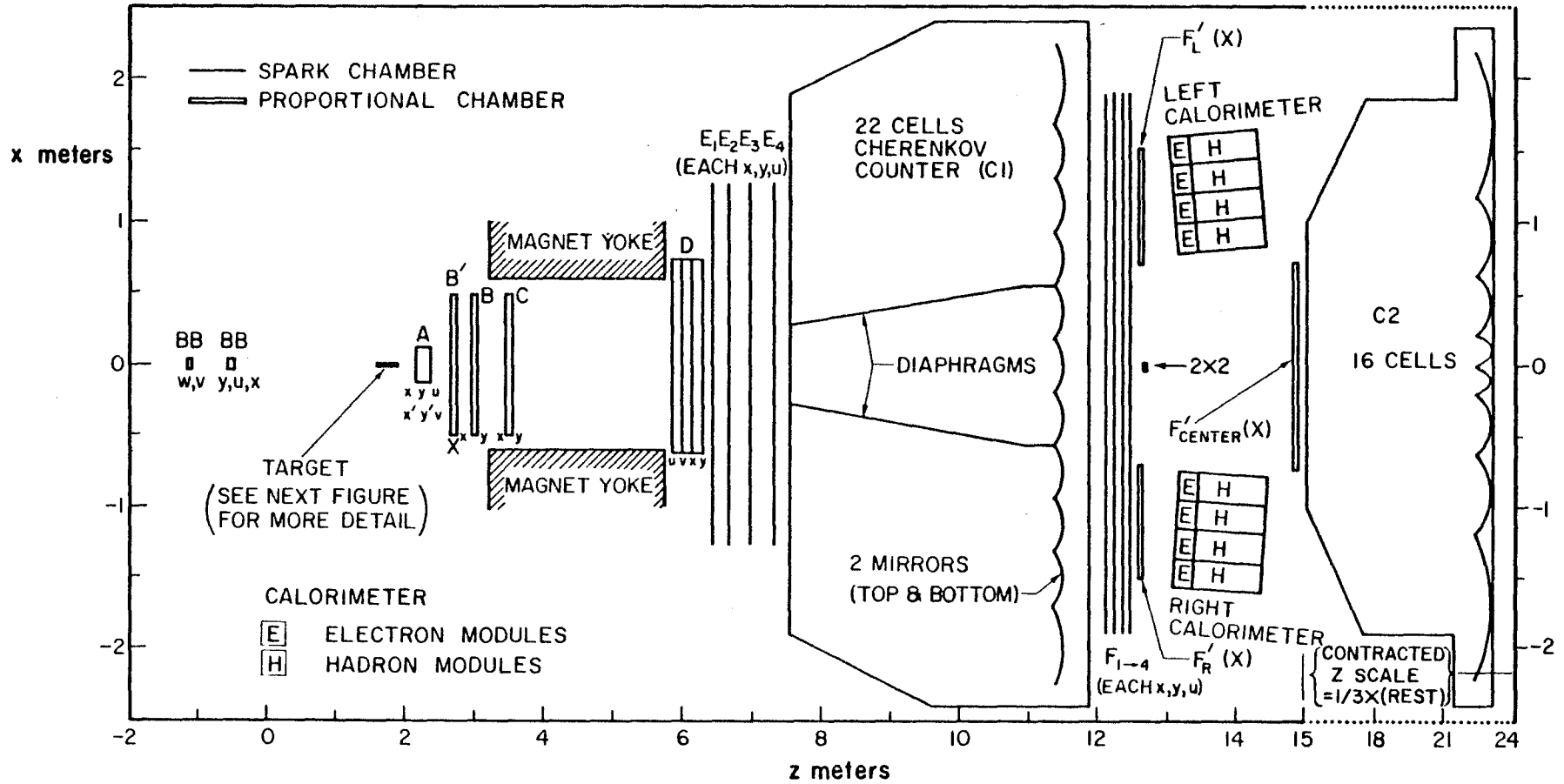
Figure 2.1

ELEVATION: FRONT PORTION OF MULTIPARTICLE SPECTROMETER

Figure 2.2

USED FOR THIS ANALYSIS

(.031 ± .005) INCH

Aℓ WINDOW

12" H$_2$ TARGET

←——— 28 cm ———→

0   10   20   30   cm.

⟹ BEAM
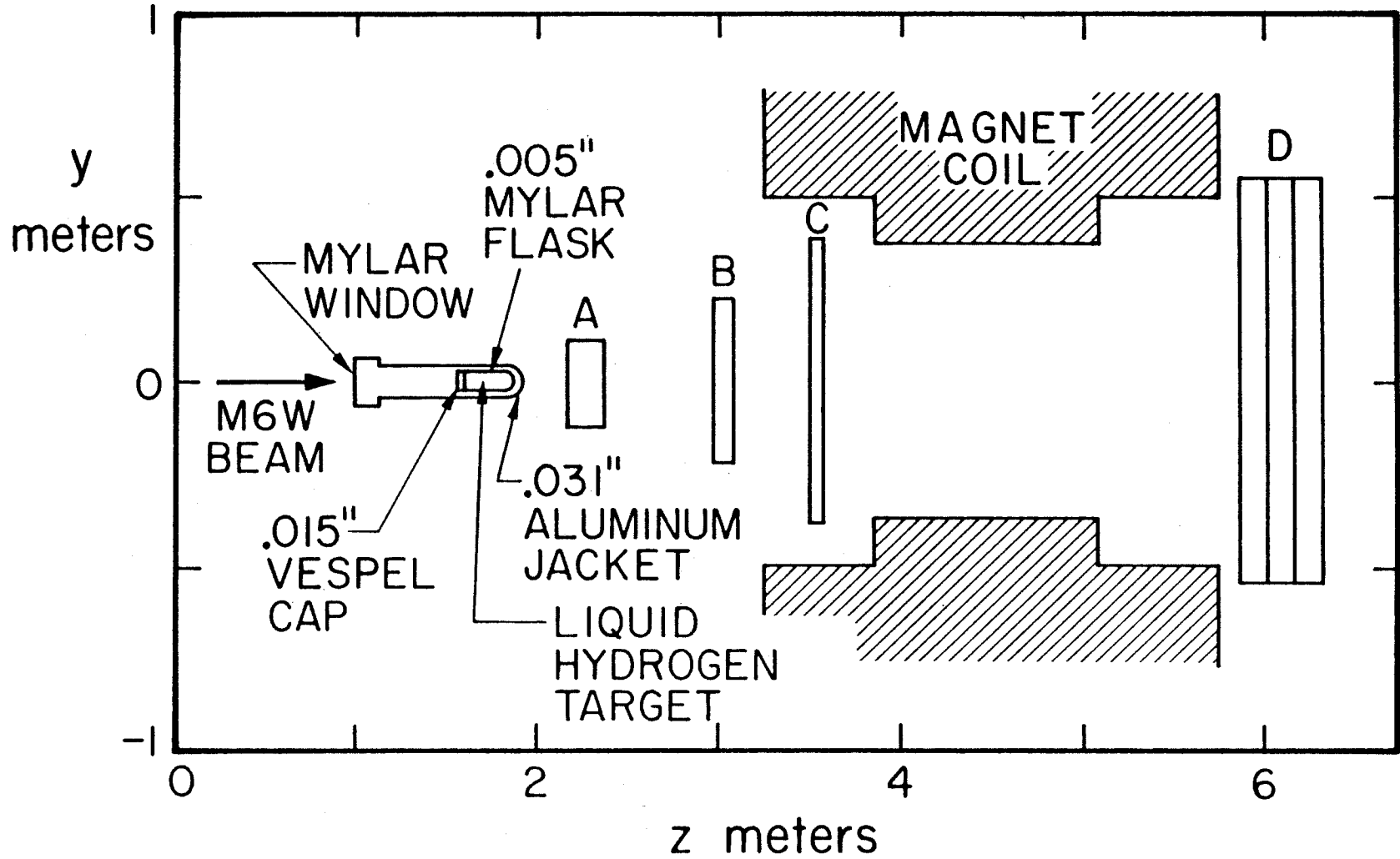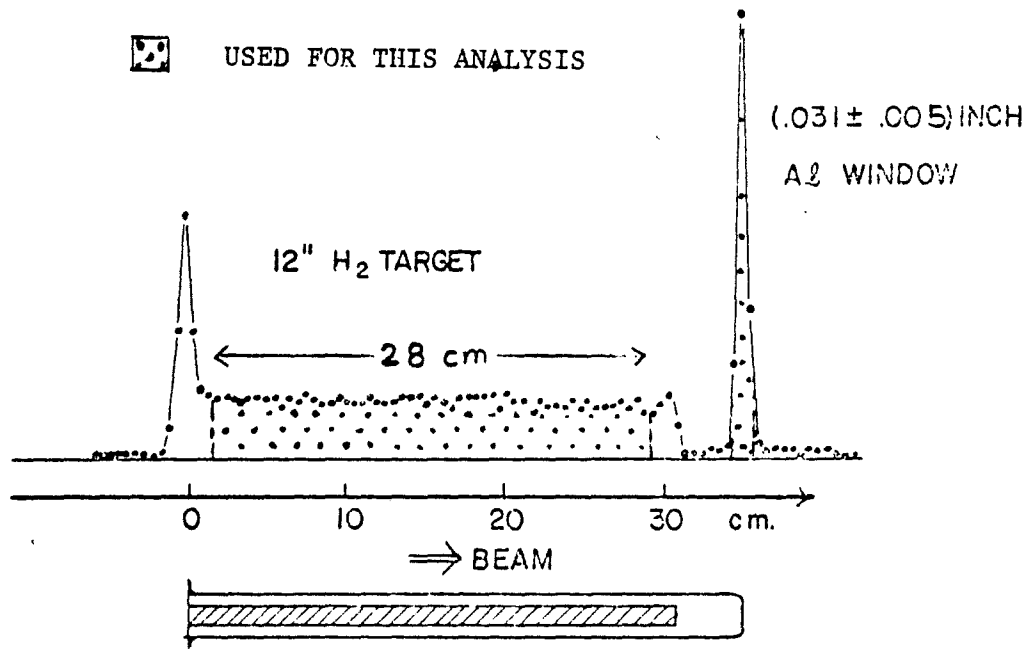
a) The vertex distribution of all triggers.

P$_⊥$

GeV/c

$X_{||}$
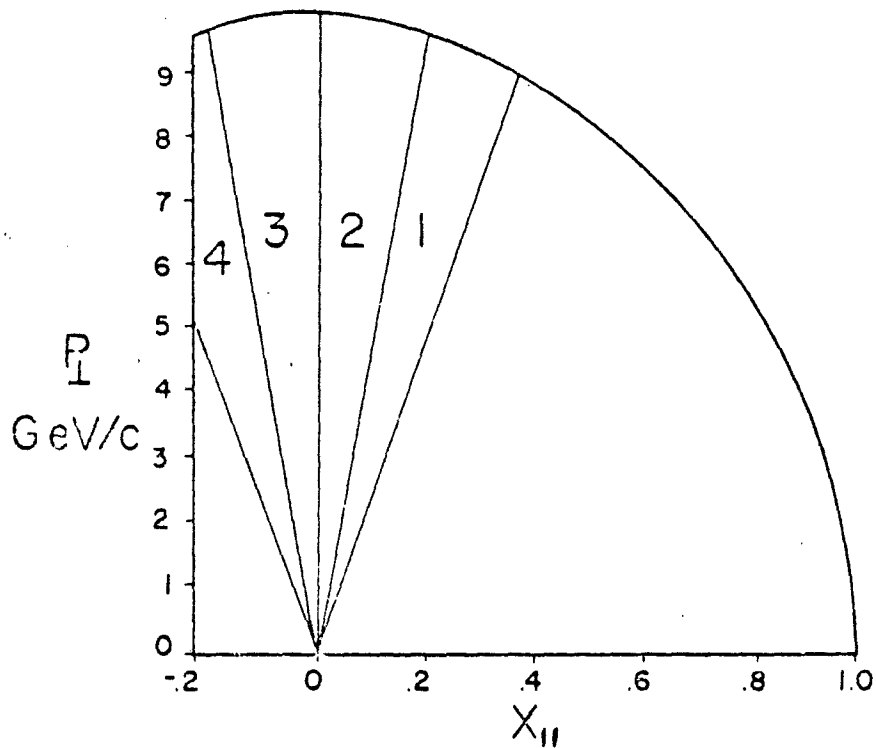
b) Acceptance of our apparatus for the
charged particles (no magnet bending)

Figure 3.1

Figure 3.2a

No. of tracks (N_t)

edge →

Number of PWC hits (N_{fv})

Figure 3.2b

Run 673

No. of particle found (N_p)

10

5

.5   1   1.5

f_D as defined in section 3.1
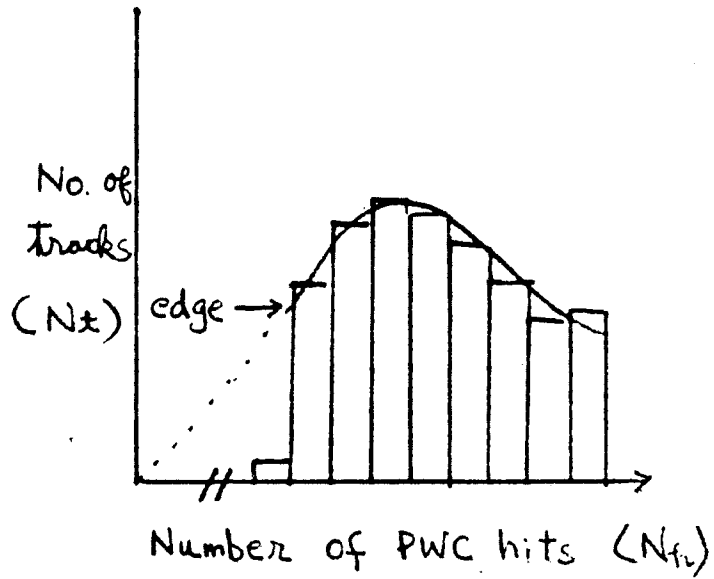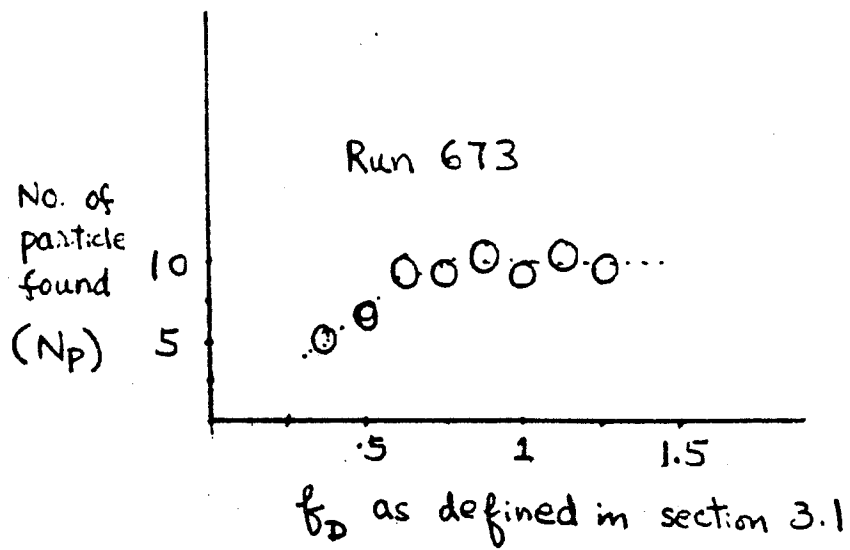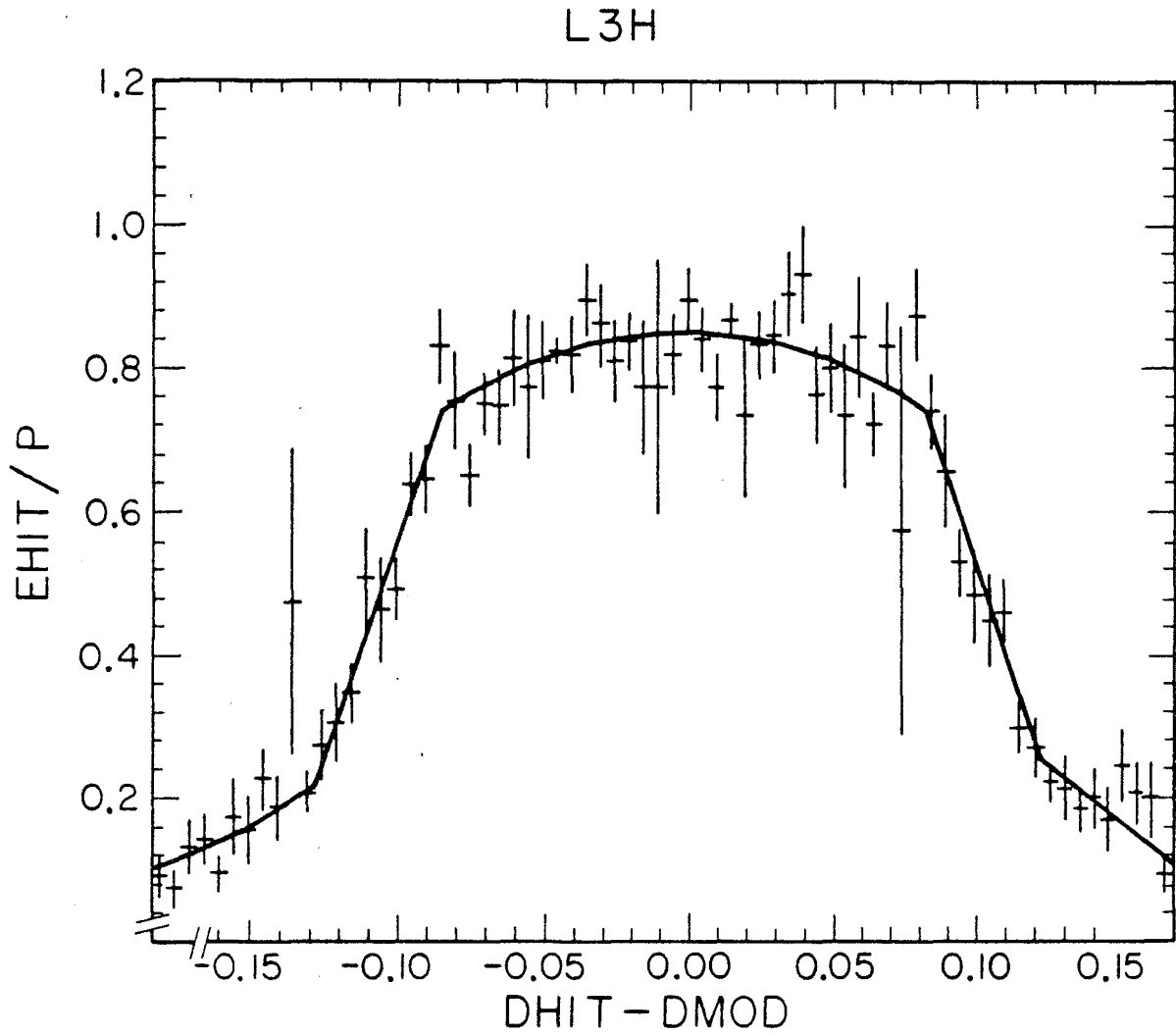
Figure 3.3 Fraction of energy deposited in
the module versus distance with respect to
the center of the module. Derivation of
this curve is described in [2.3b].
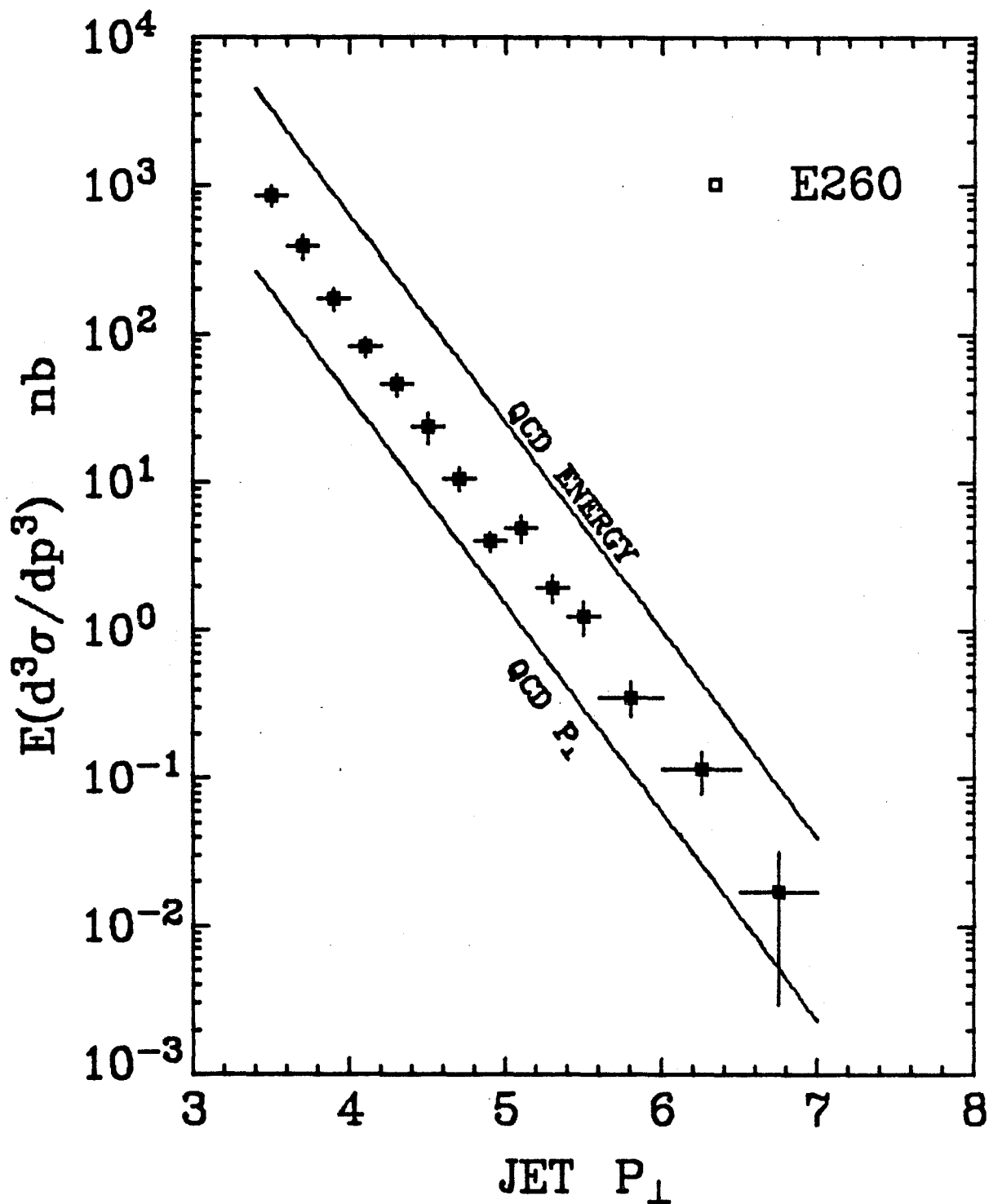
pp→JET+X

Figure 4.2a   E260 jet cross section and comparison with QCD predictions (using FFF model).
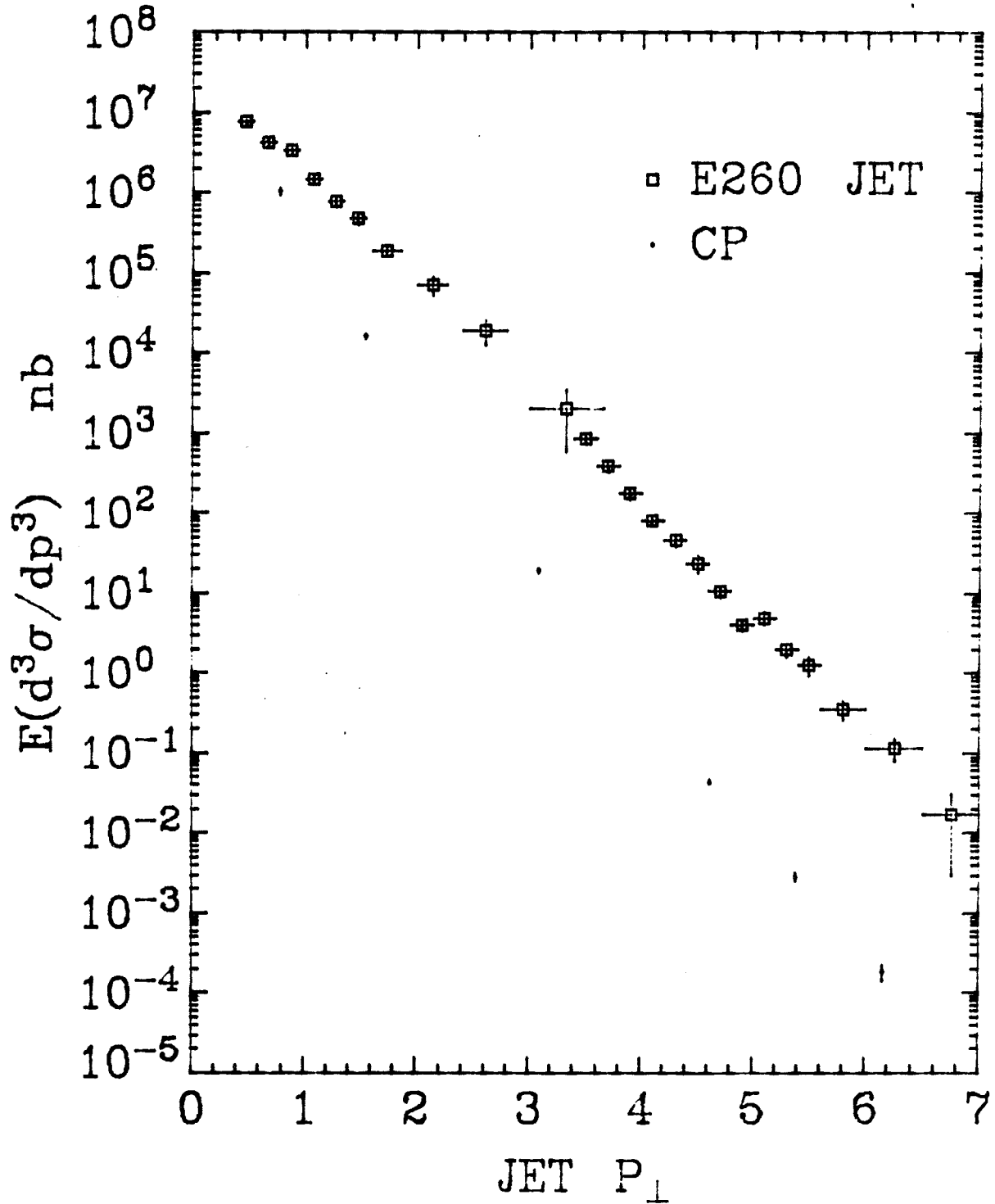
Figure 4.2b   E260 jet cross section and Chicago-Princeton single particle cross section.

Figure 4.3   Ratios of jet cross sections
(vs. jet $P_\perp$) for different beam types.

EXPT. 260
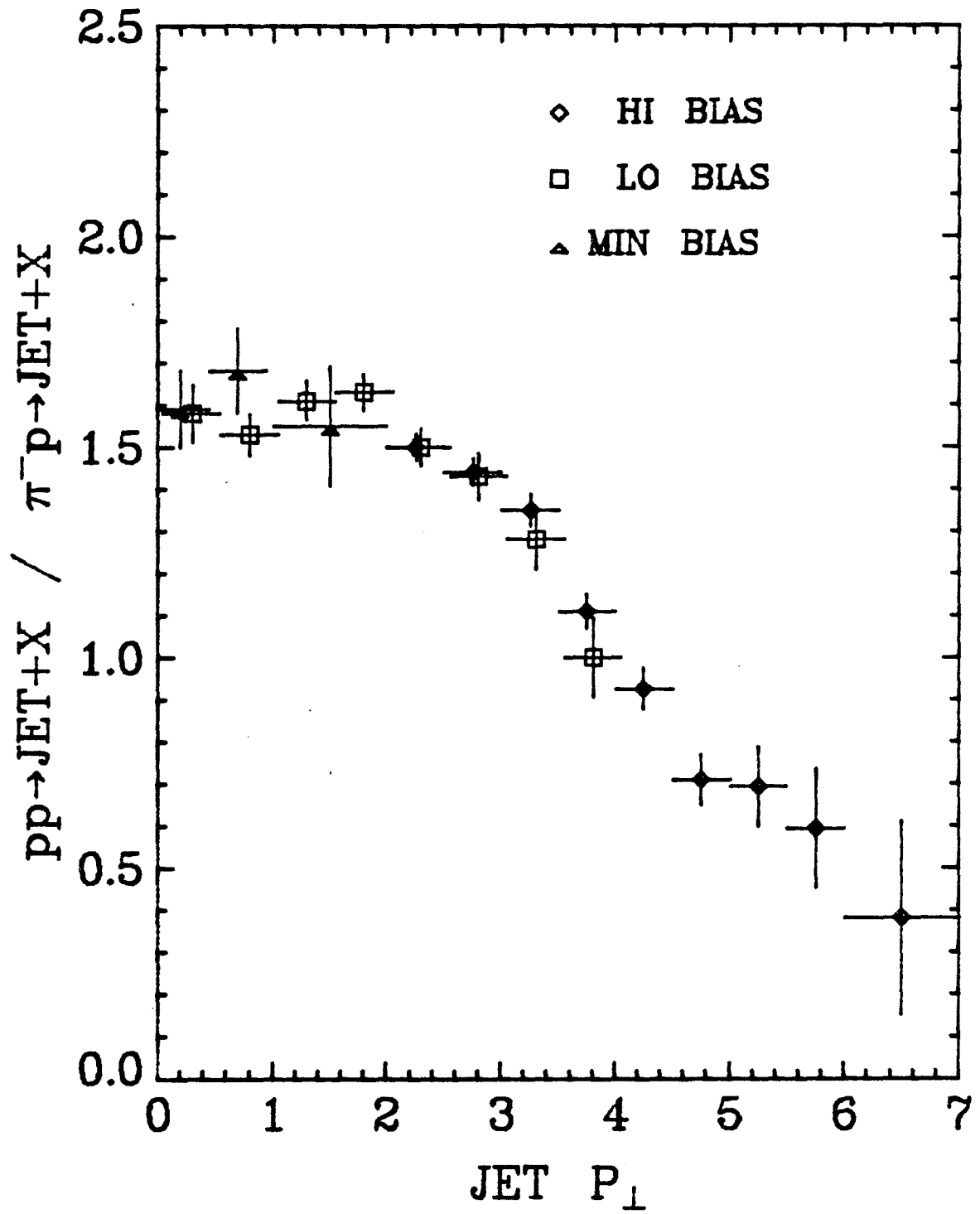
Figure 4.3a

EXPT. 260
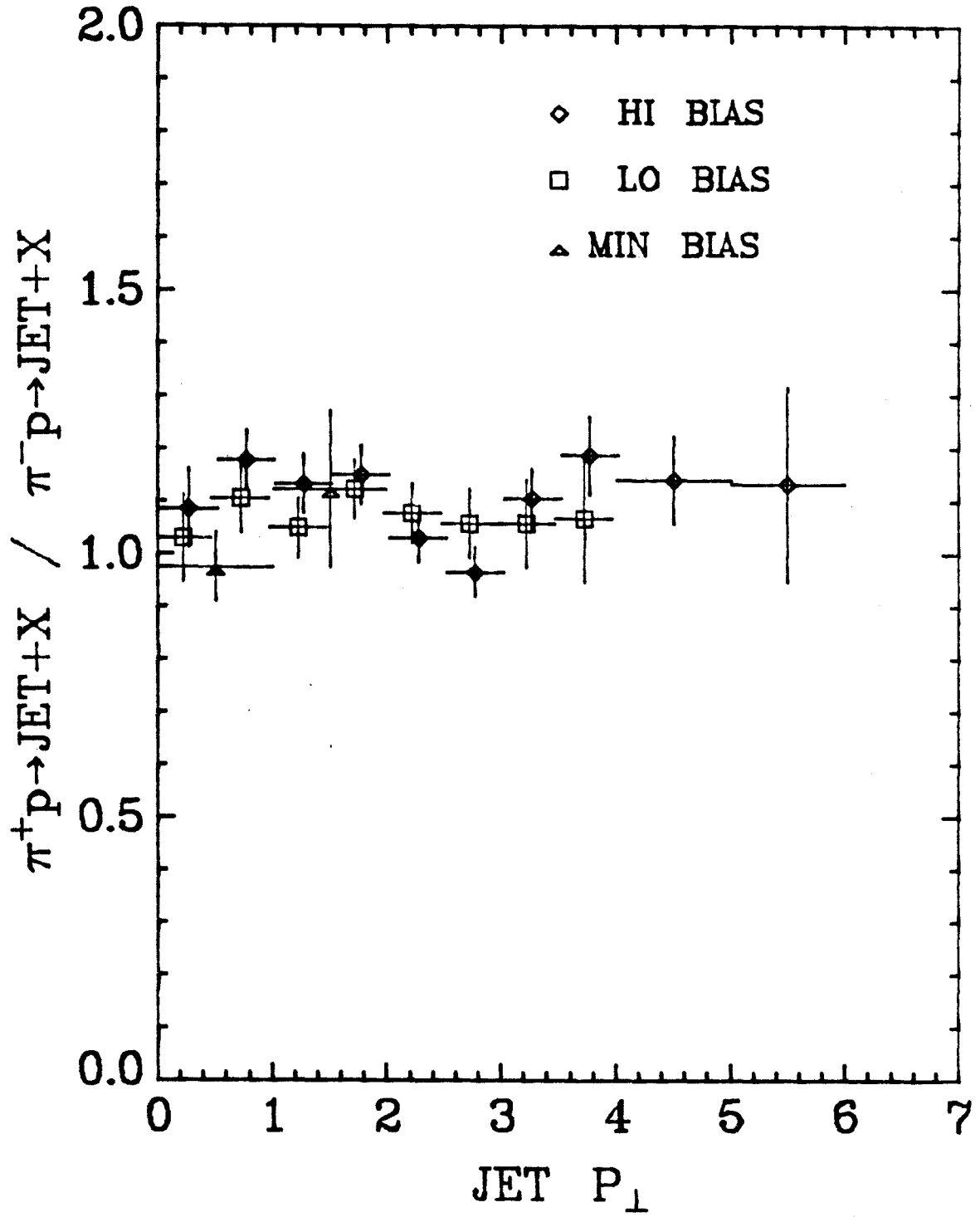
Figure 4.3b

EXPT. 260
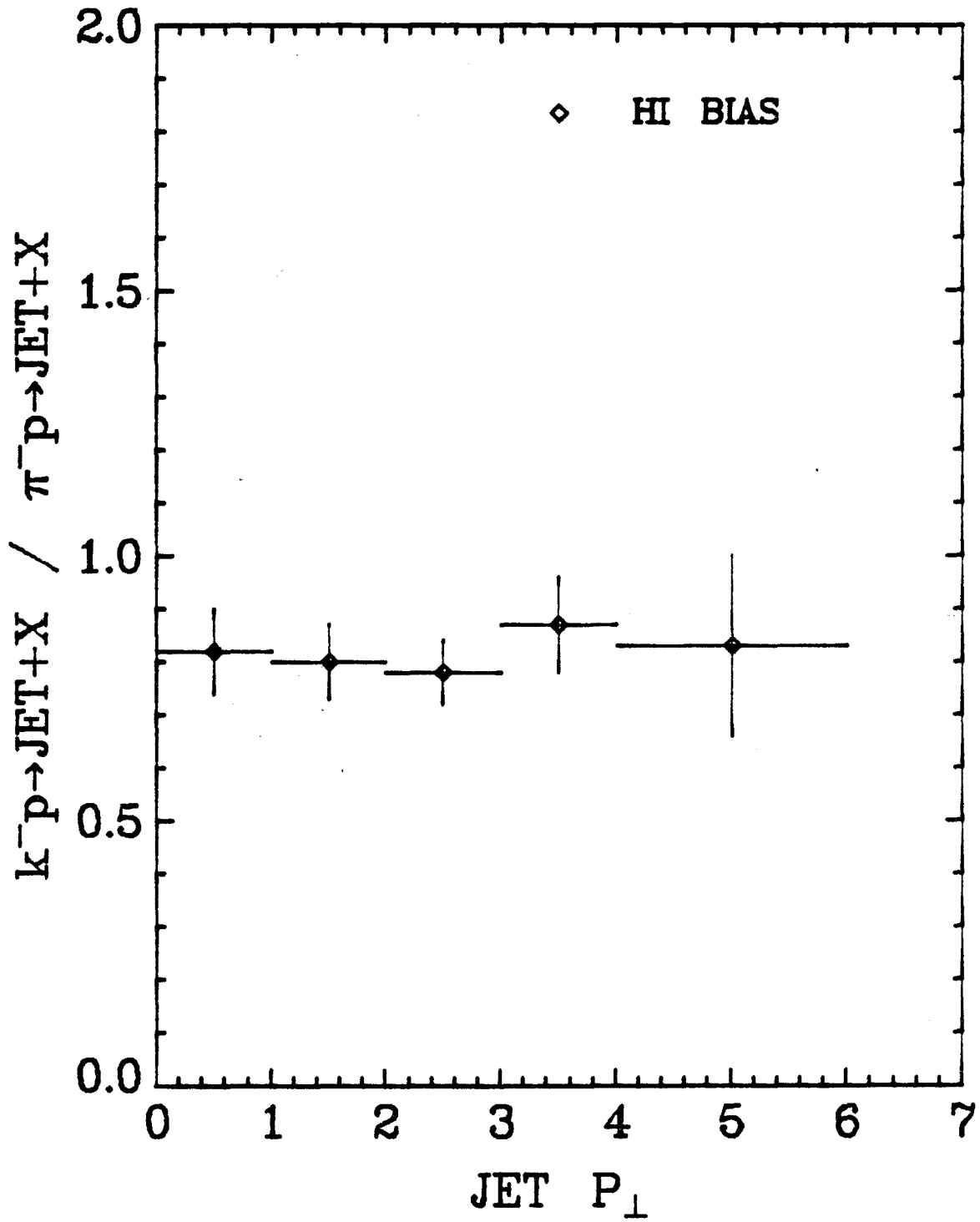
Figure 4.3c

PROTON BEAM   JET
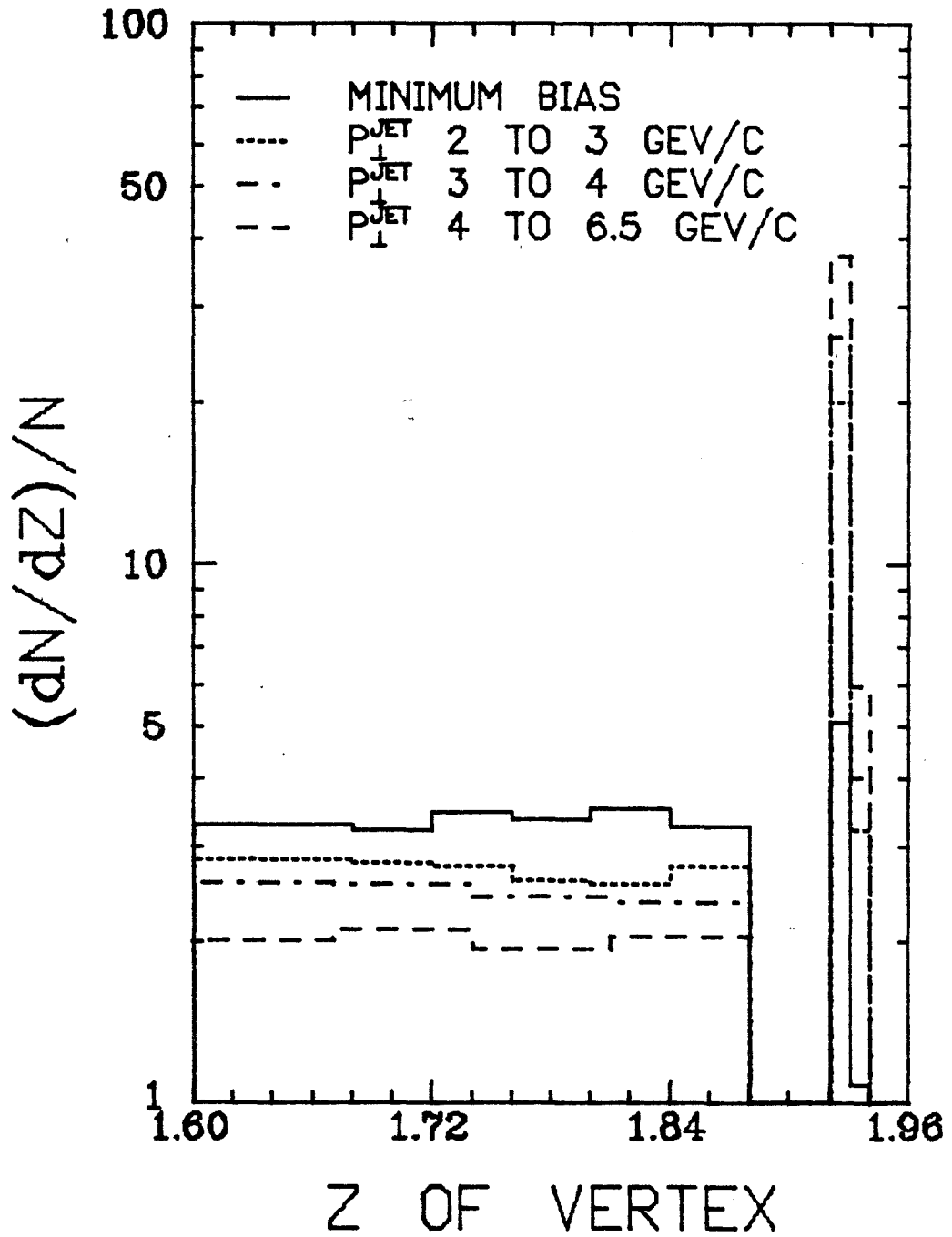
Figure 5.1a   Vertex distribution for jet trigger.
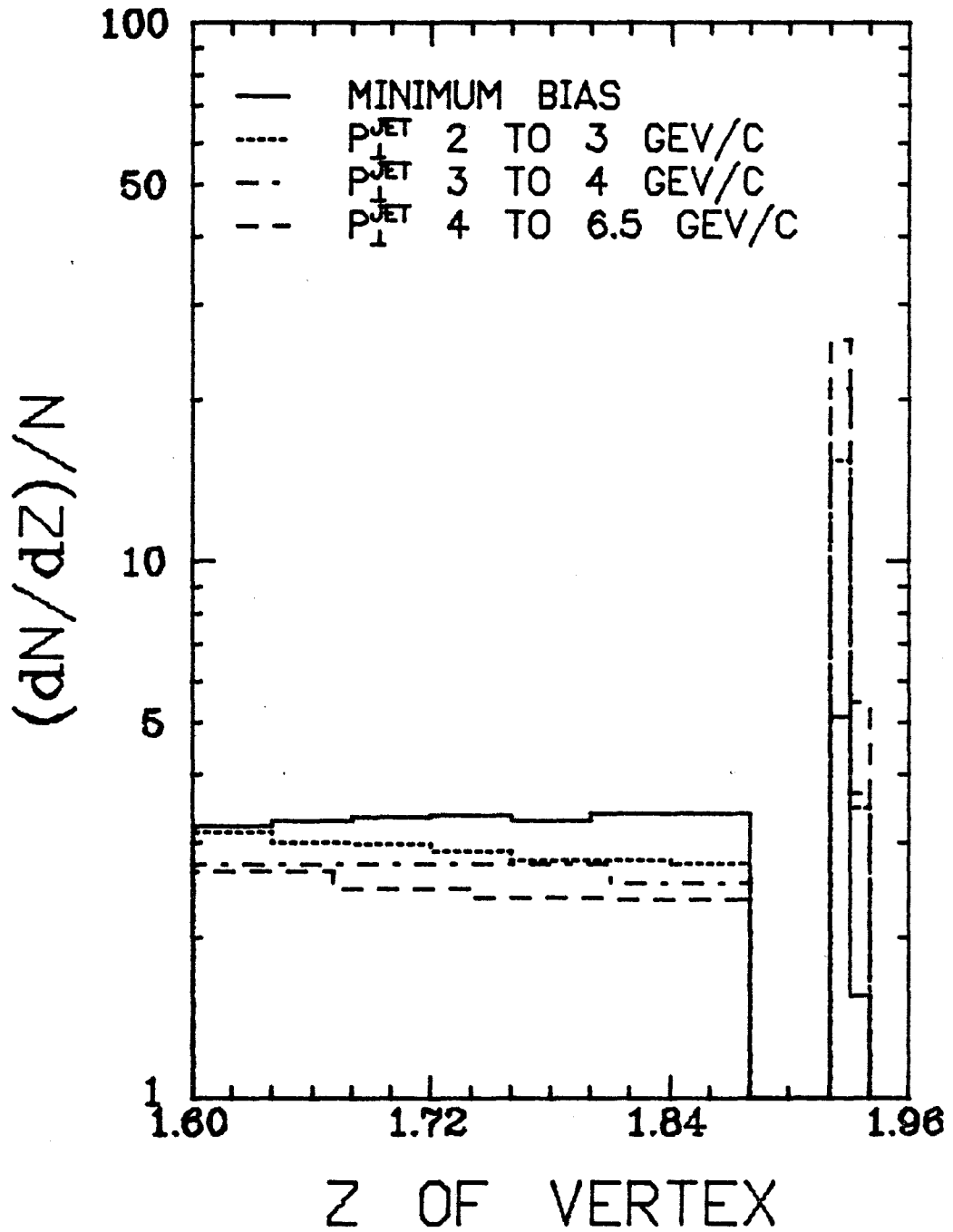
π^- BEAM JET

Figure 5.1b   Vertex distribution for jet trigger.

π^+ BEAM JET
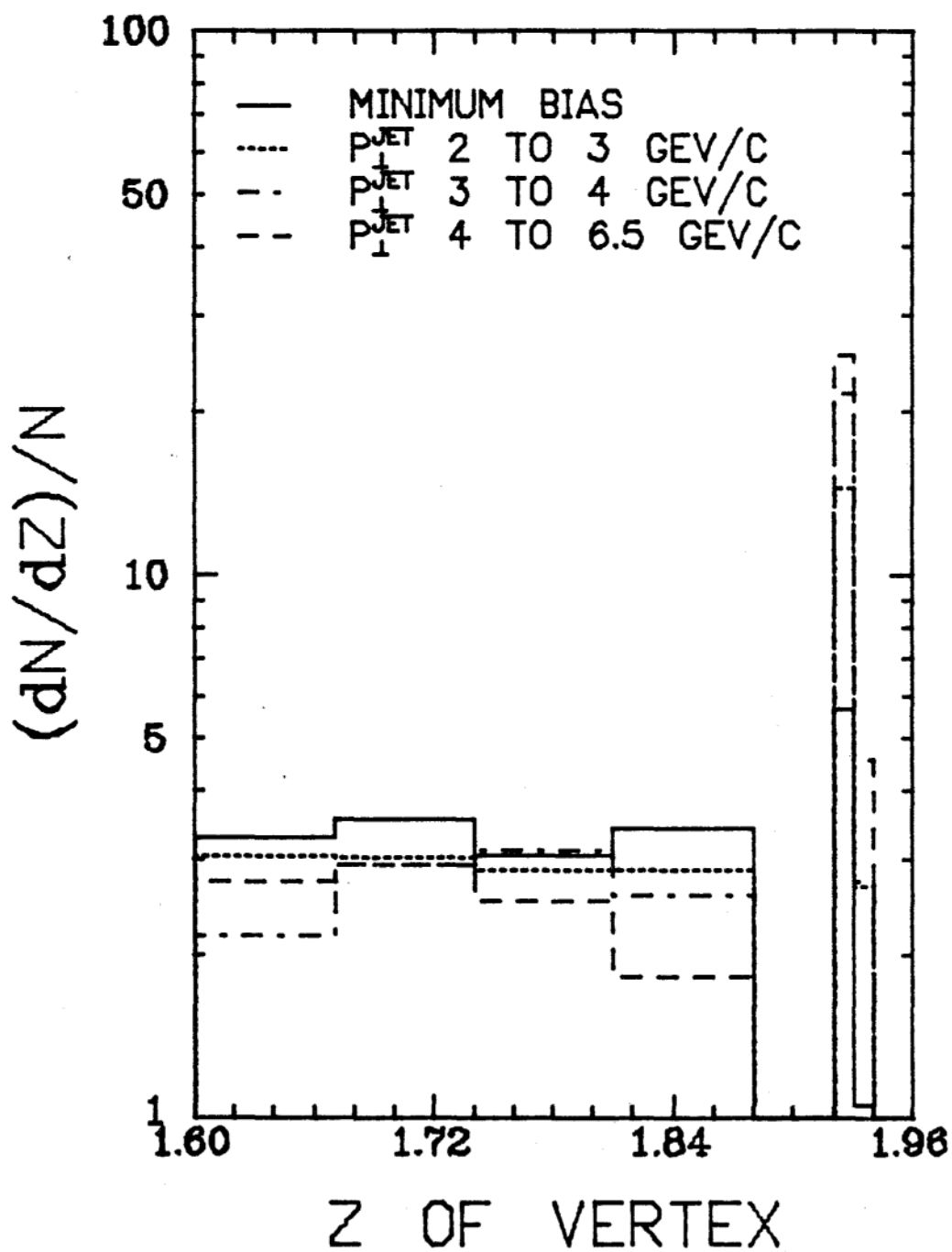
Figure 5.1c   Vertex distribution for jet trigger.

π^- BEAM

$6.5 \geqq PT_{TRG} \geqq 4$
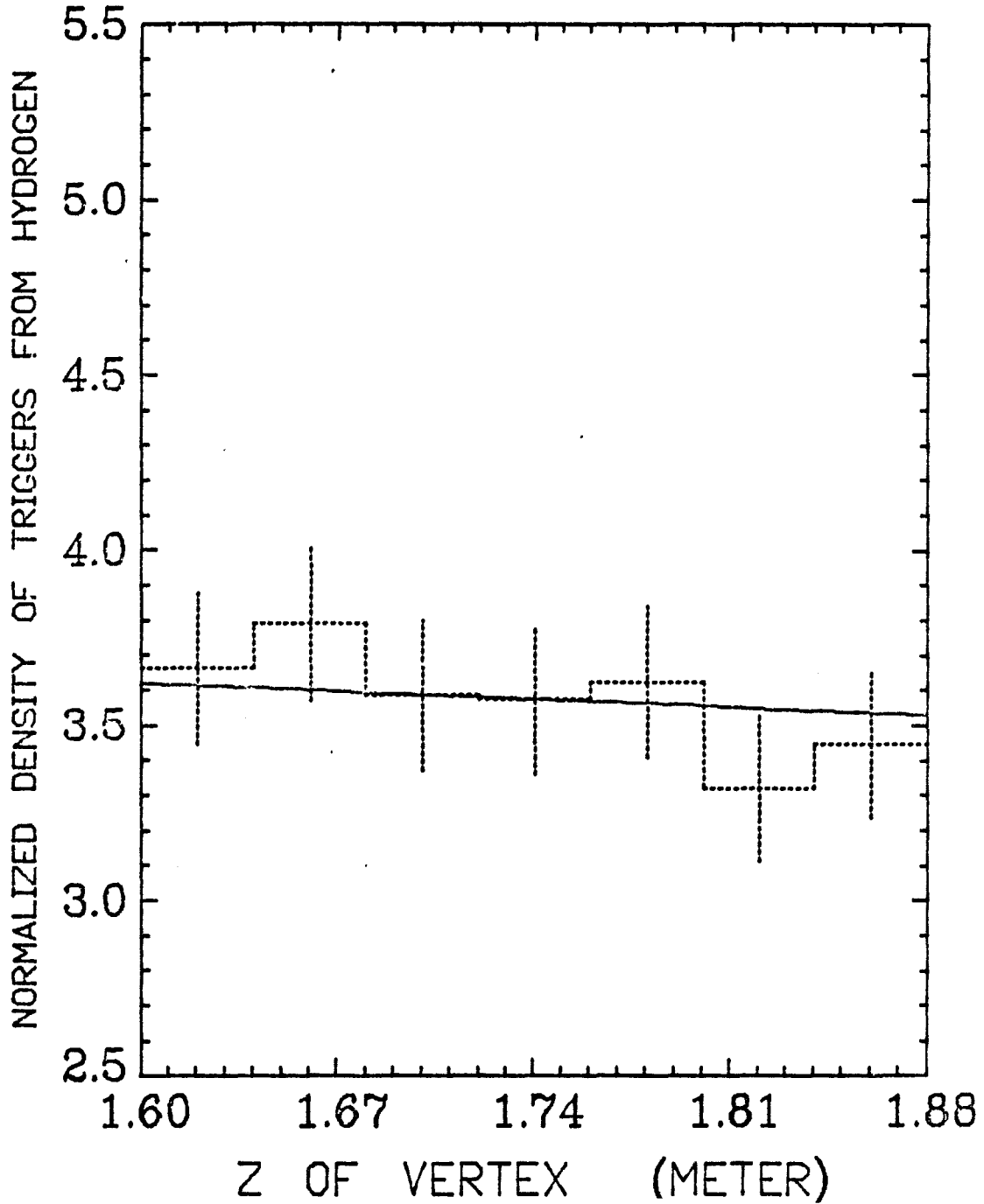
Figure 5.1d   Vertex distribution for jets produced off Hydrogen by π^-. The curve is the expected beam attenuation   calculated from π^- absorption cross section.
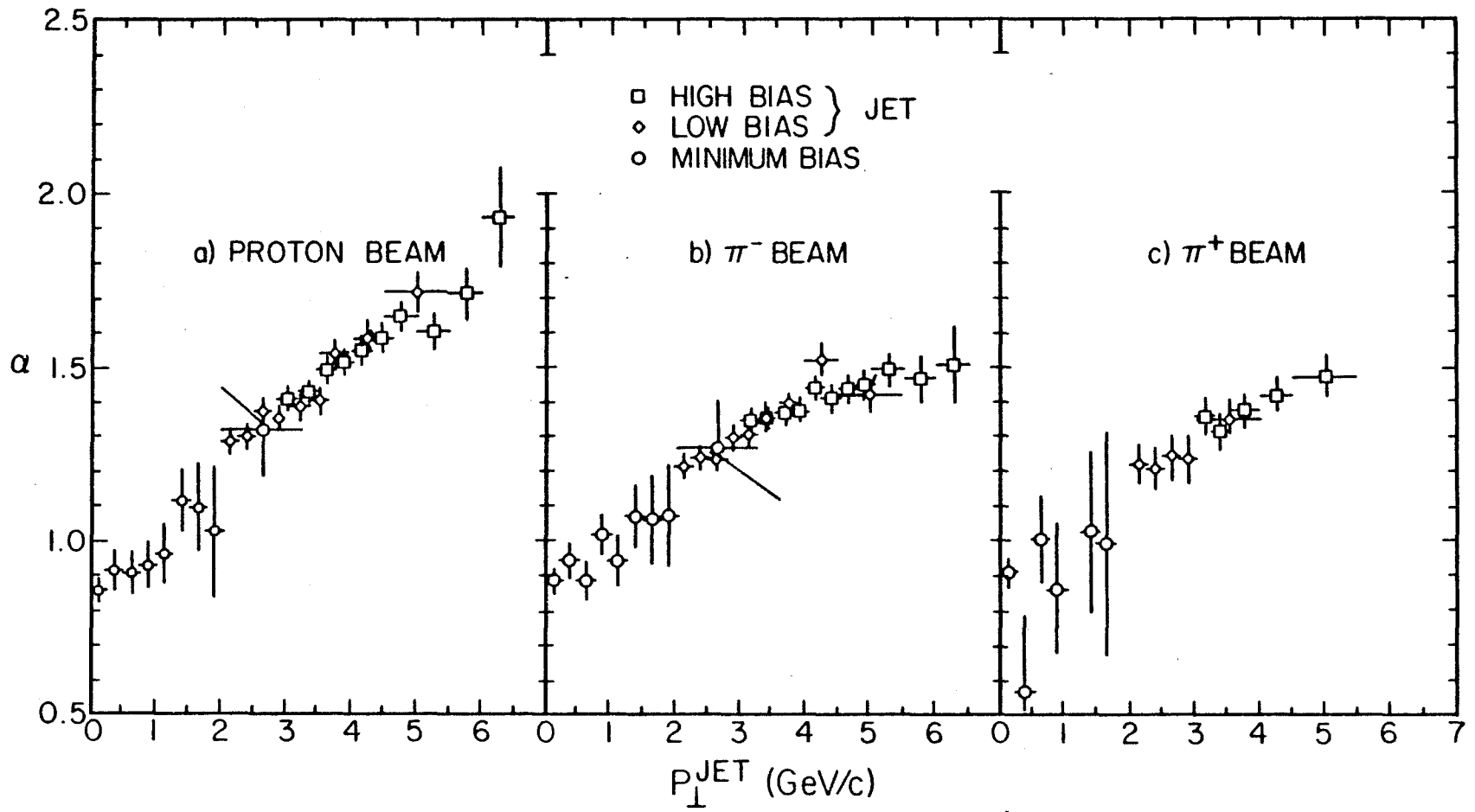
Figure 5.2a   α vs. jet $p_\perp$ for jets.
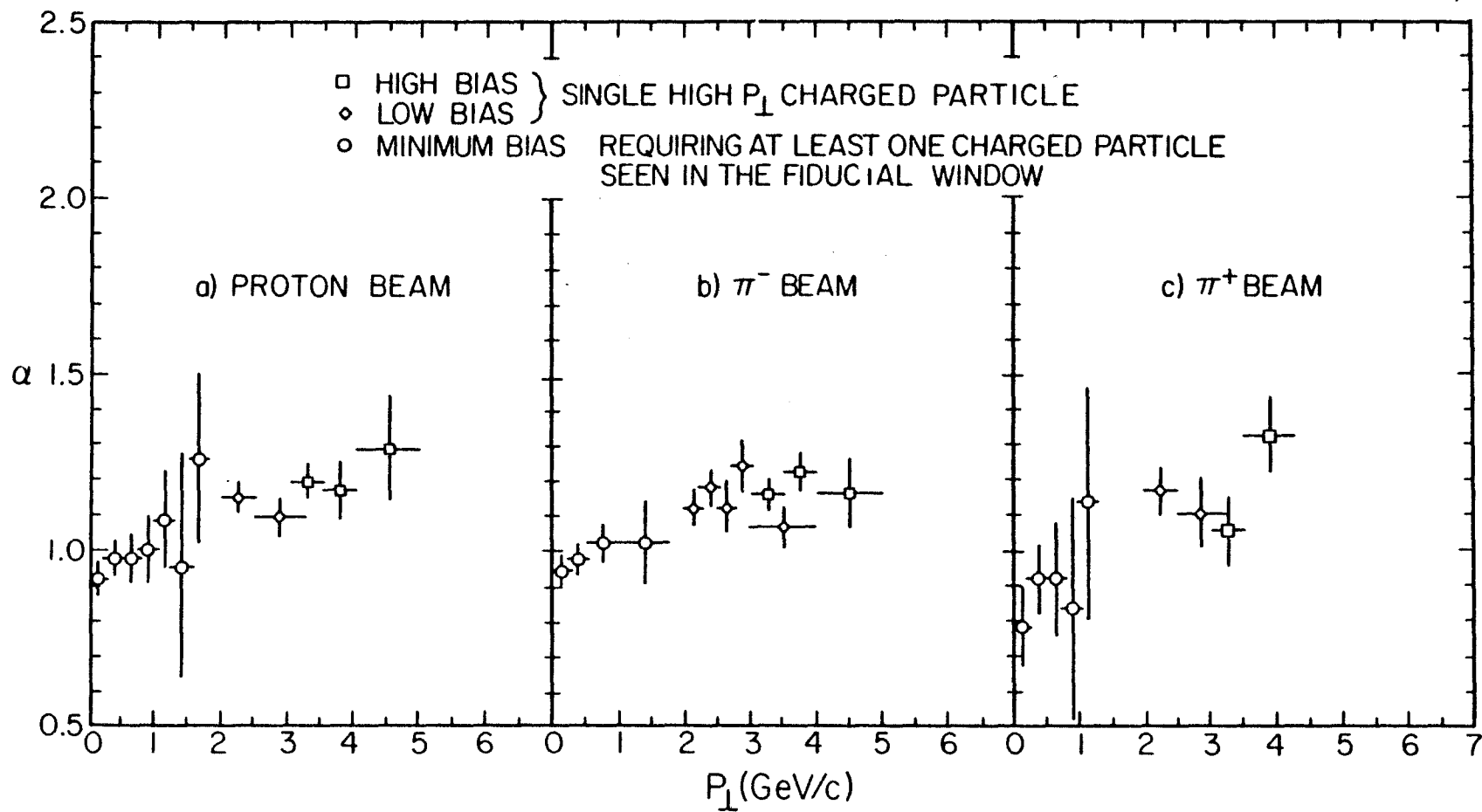
Figure 5.2b α vs. p⊥ for single charged particles.
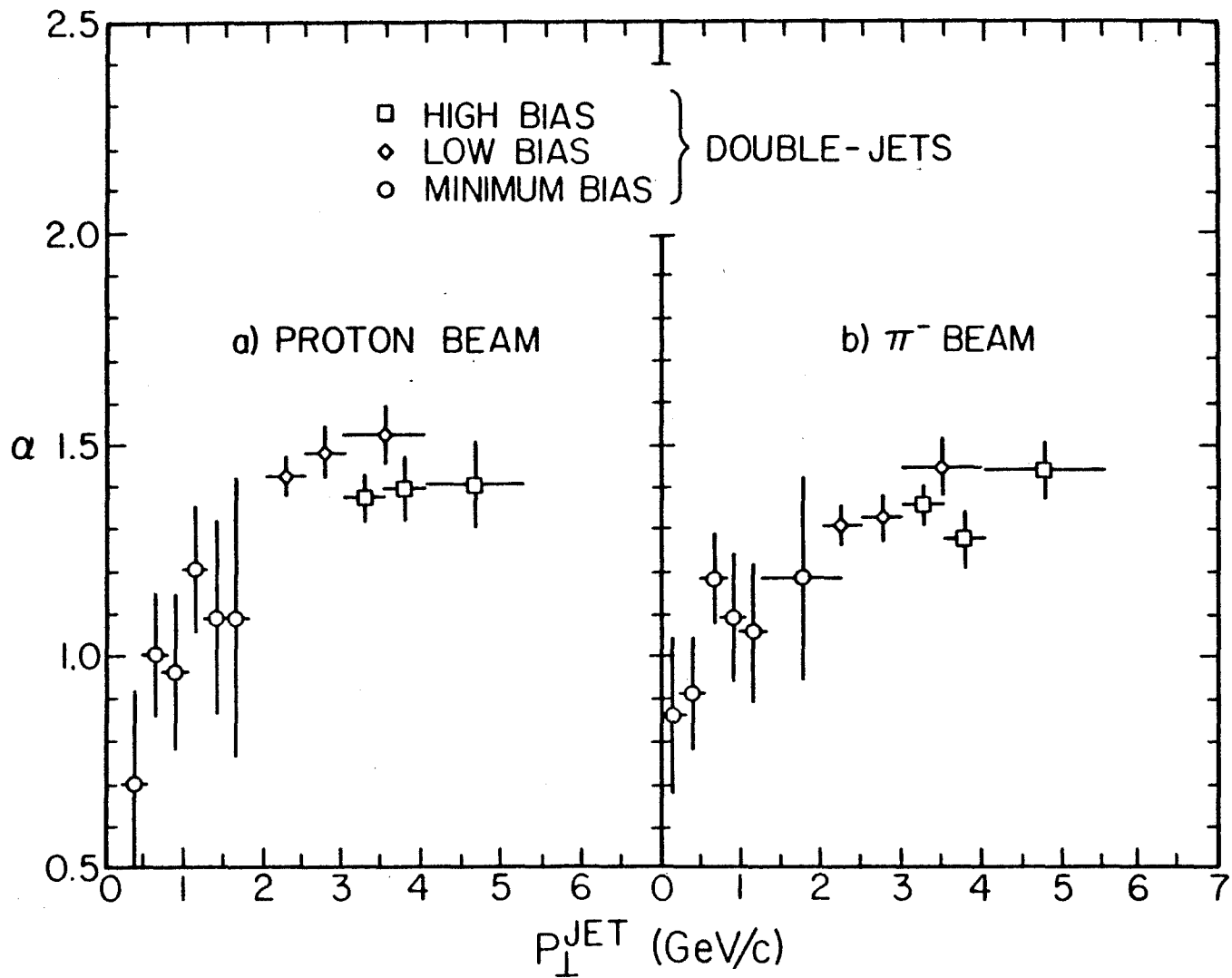
Figure 5.2c   α vs. jet $p_\perp$ for double-jets.
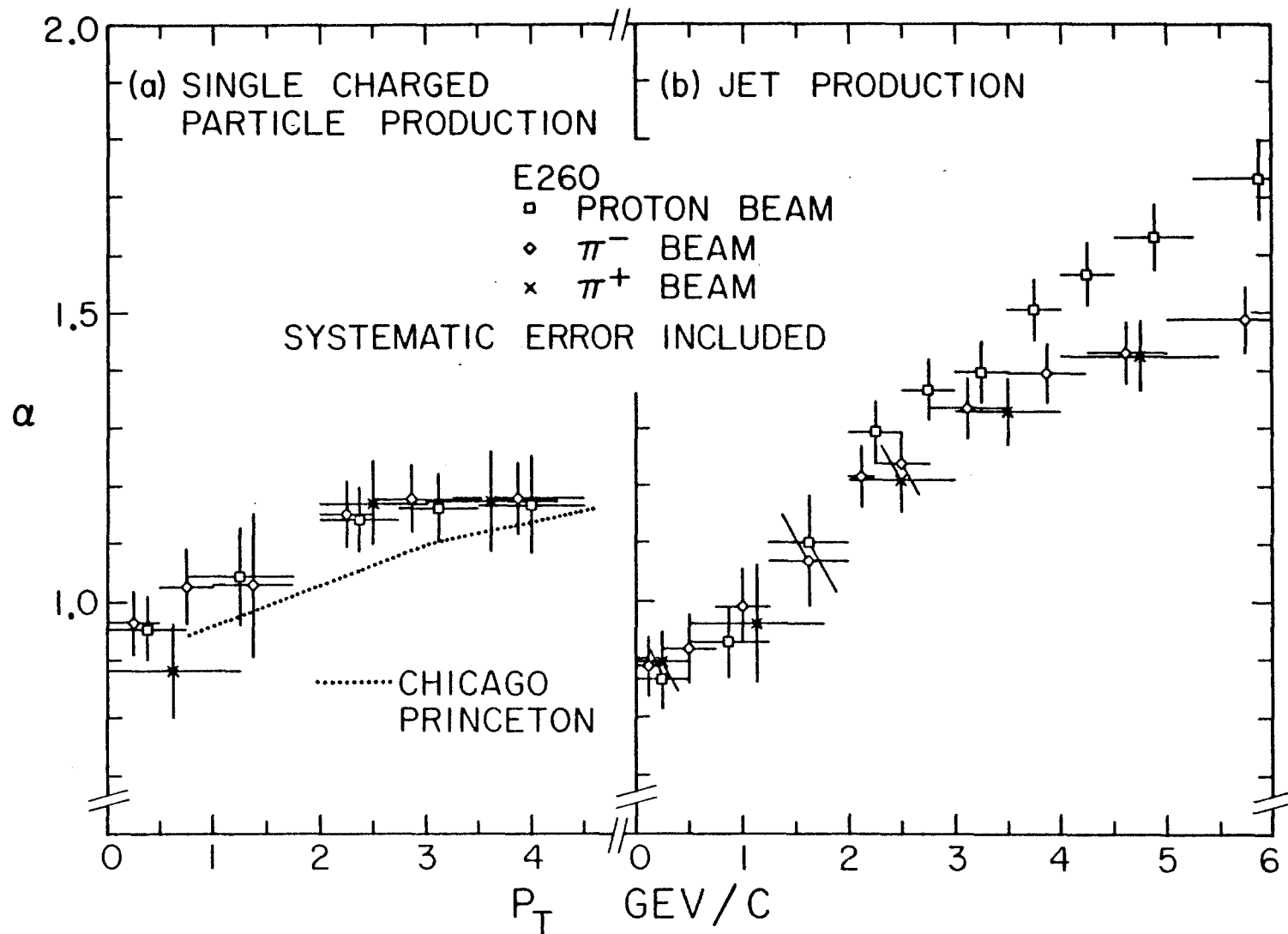
Figure 5.3   α vs. $p_\perp$ for jet, single particle and minimum bias triggers.   The curve marked CHICAGO PRINCETON comes from [1.15].
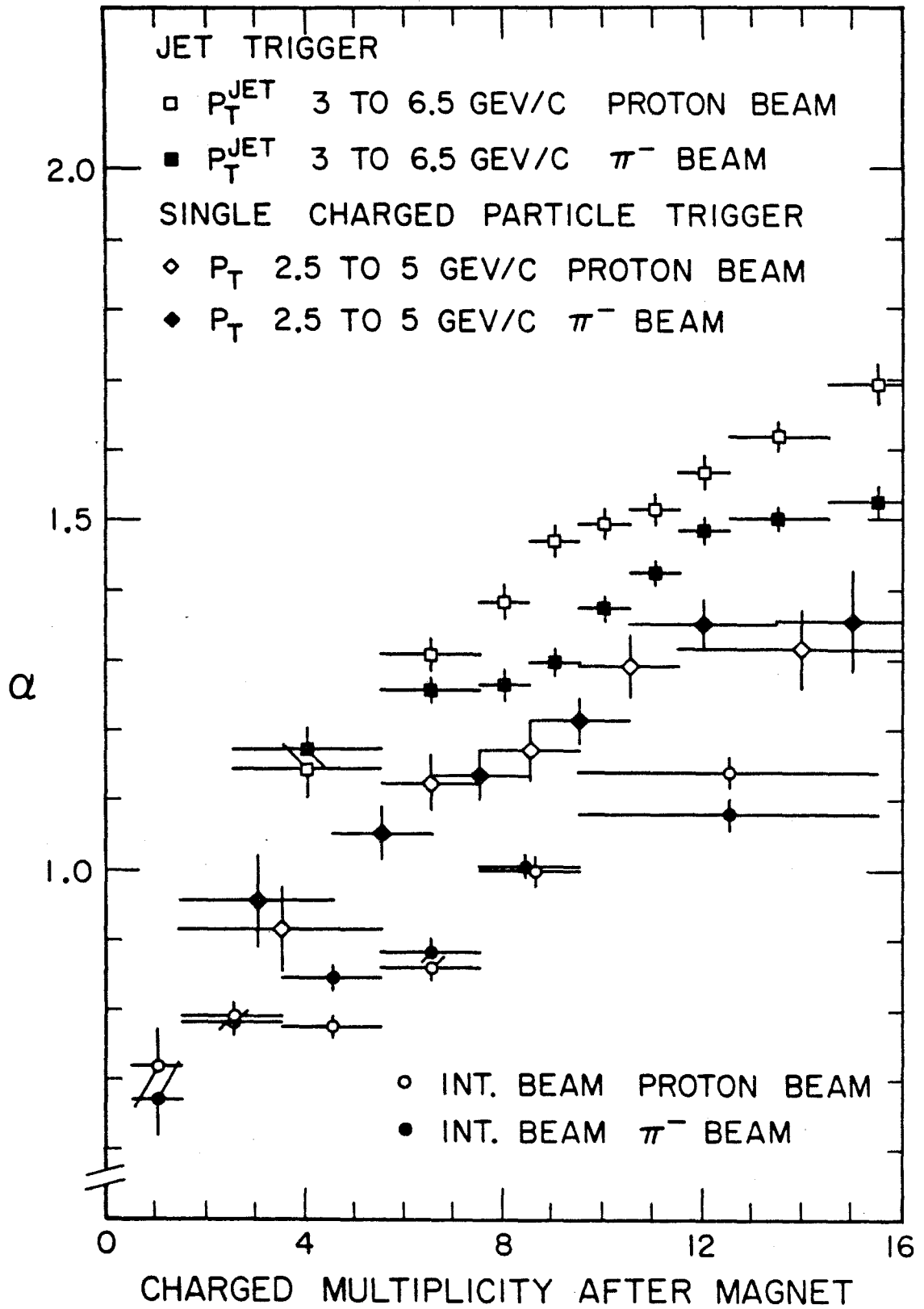
Figure 5.4 α vs. the total charged multiplicity seen after the magnet.
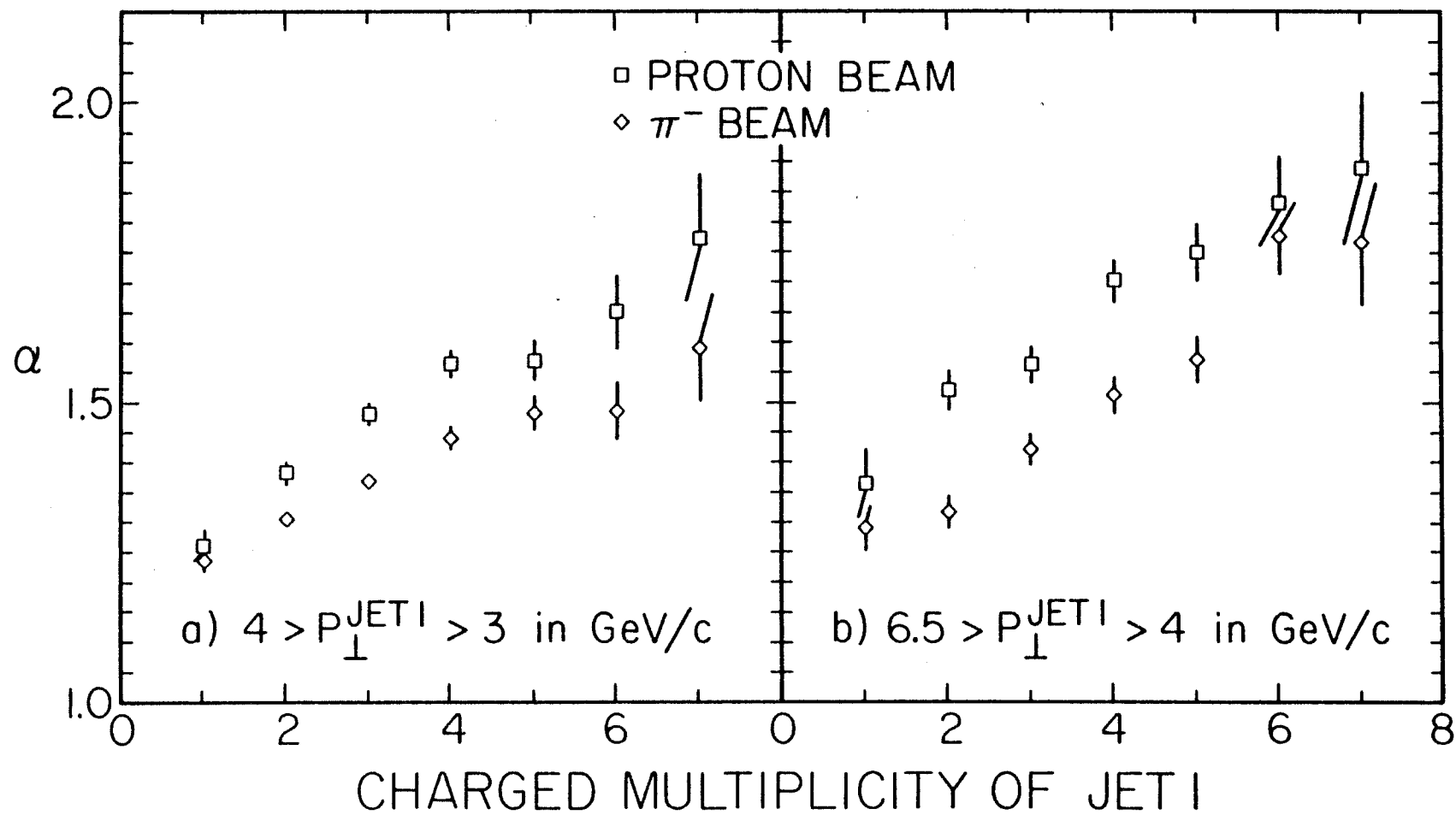
Figure 5.5   α versus multiplicity of charged particle in the jet.
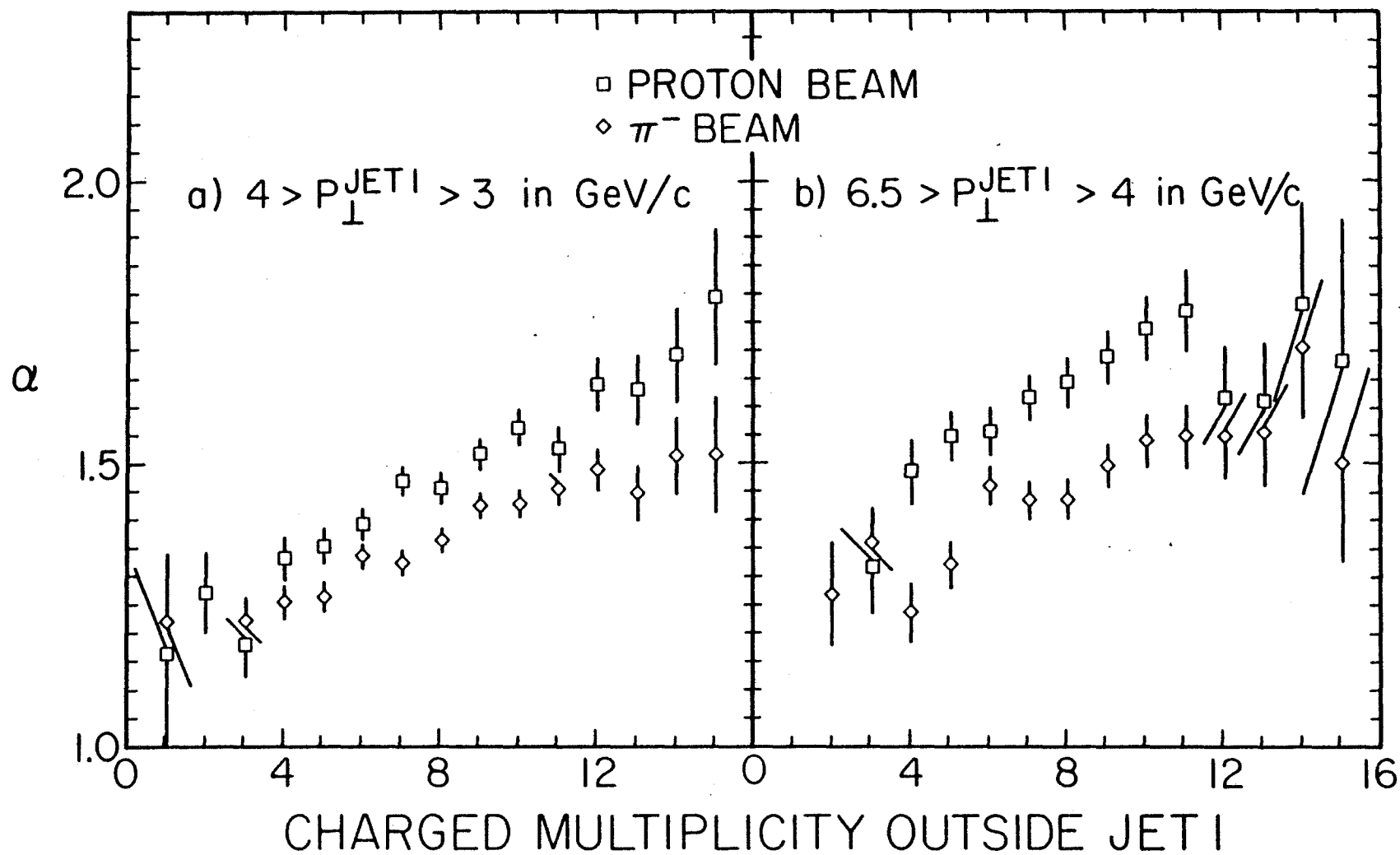
Figure 5.6   α versus   charged multiplicity outside the jet.
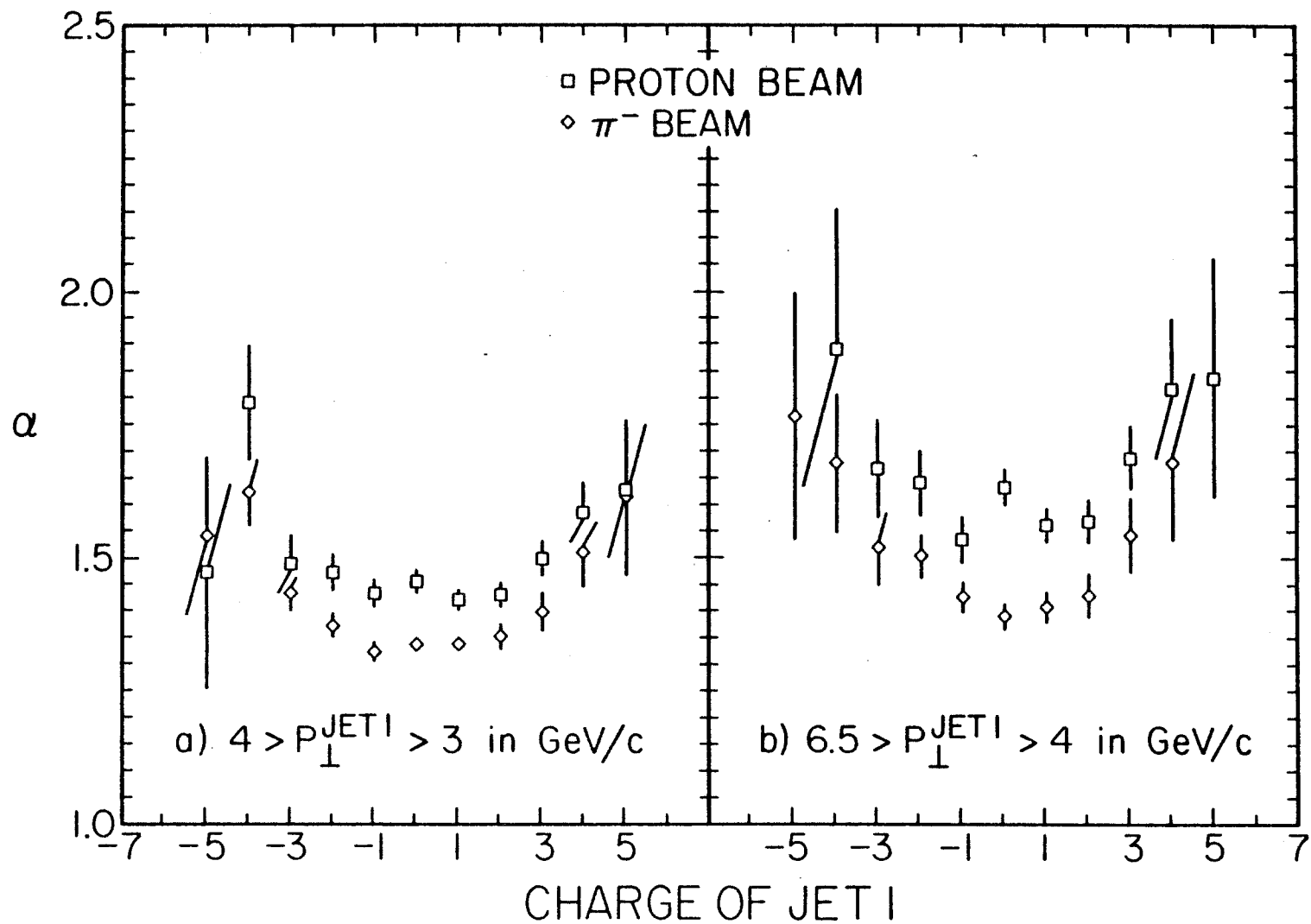
Figure 5.7 α vs. charge of the jet
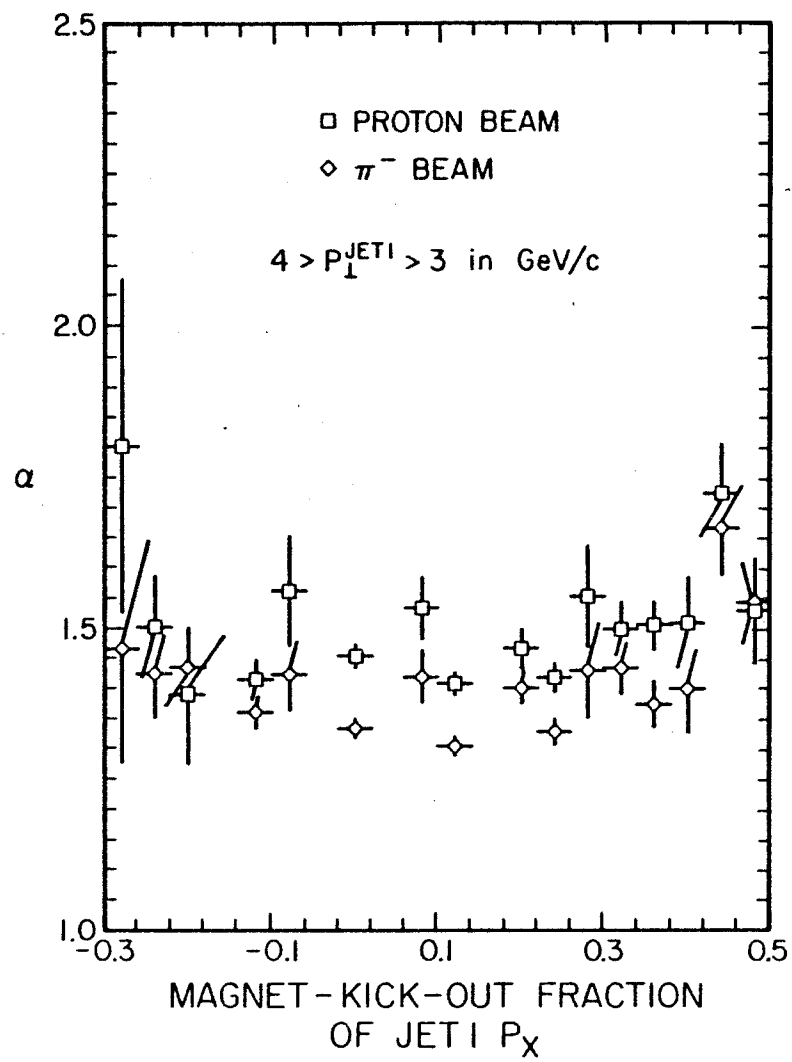
Figure 5.9   α versus f_{mk}, where f_{mk} is defined in the text.
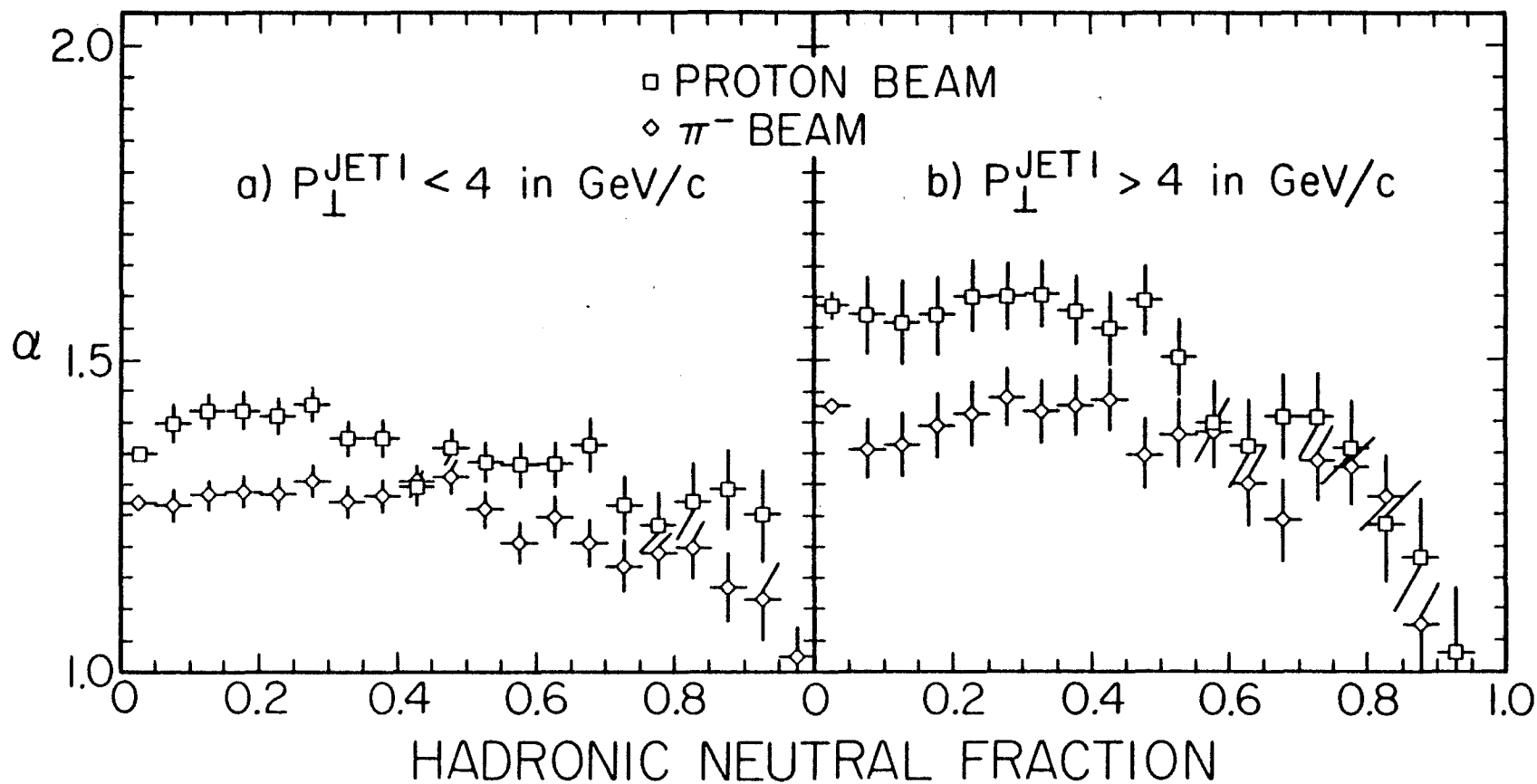
Figure 5.10   α vs. hadronic neutral fraction before any other cut.
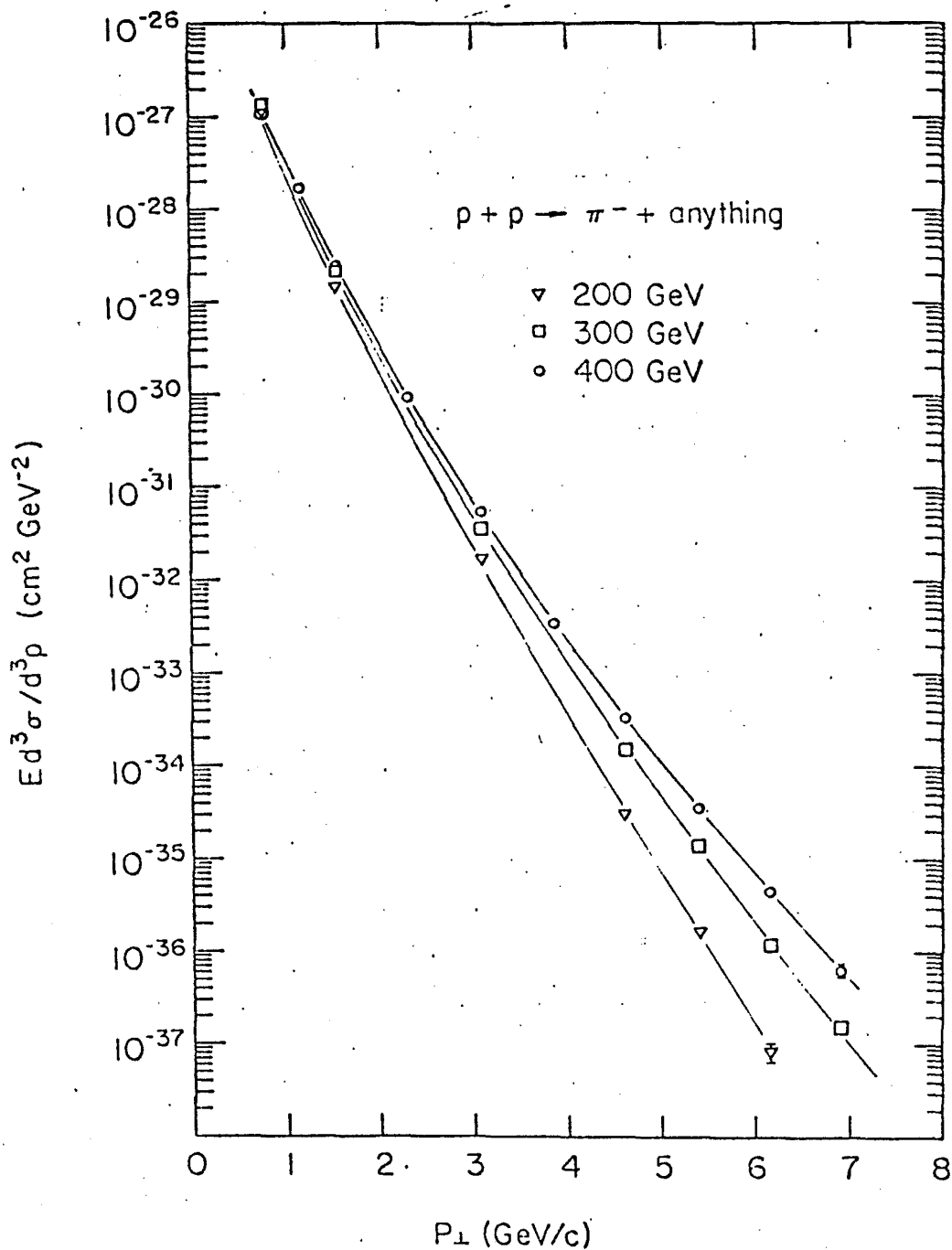
Figure 5.11a   Data showing that the invariant cross section for

π^- production increases with s at fixed $p_\perp$.

b)

$\sqrt{s} = 27.4\,\text{GeV}$

$P_\perp = 3.82\,\text{GeV/c}$

c)
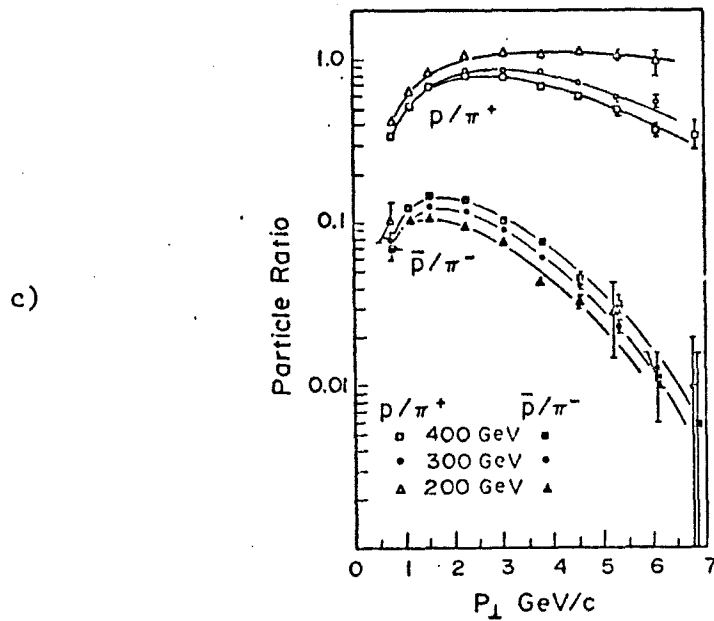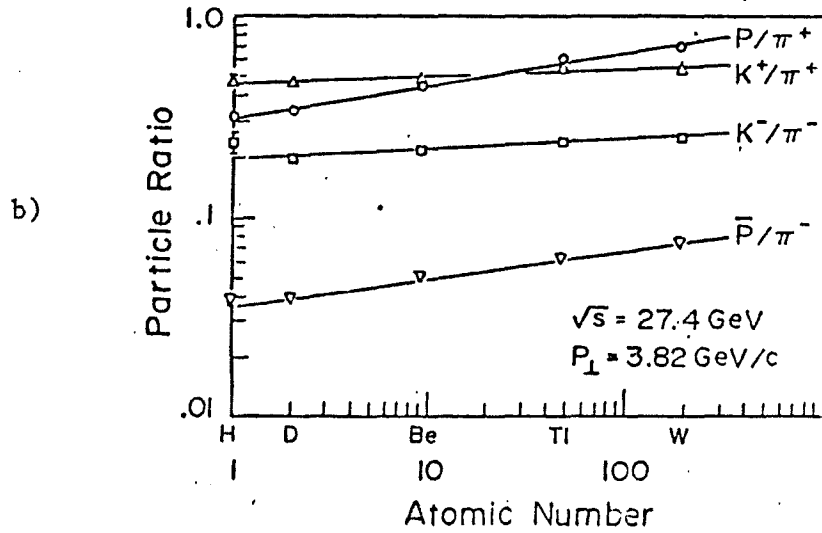
Figure 5.11

b) Data showing that p/π^+ ratio increases with A.

c) Data showing that p/π^+ ratio decreases with s.

All data (a to c) come from Ref.[1.15].
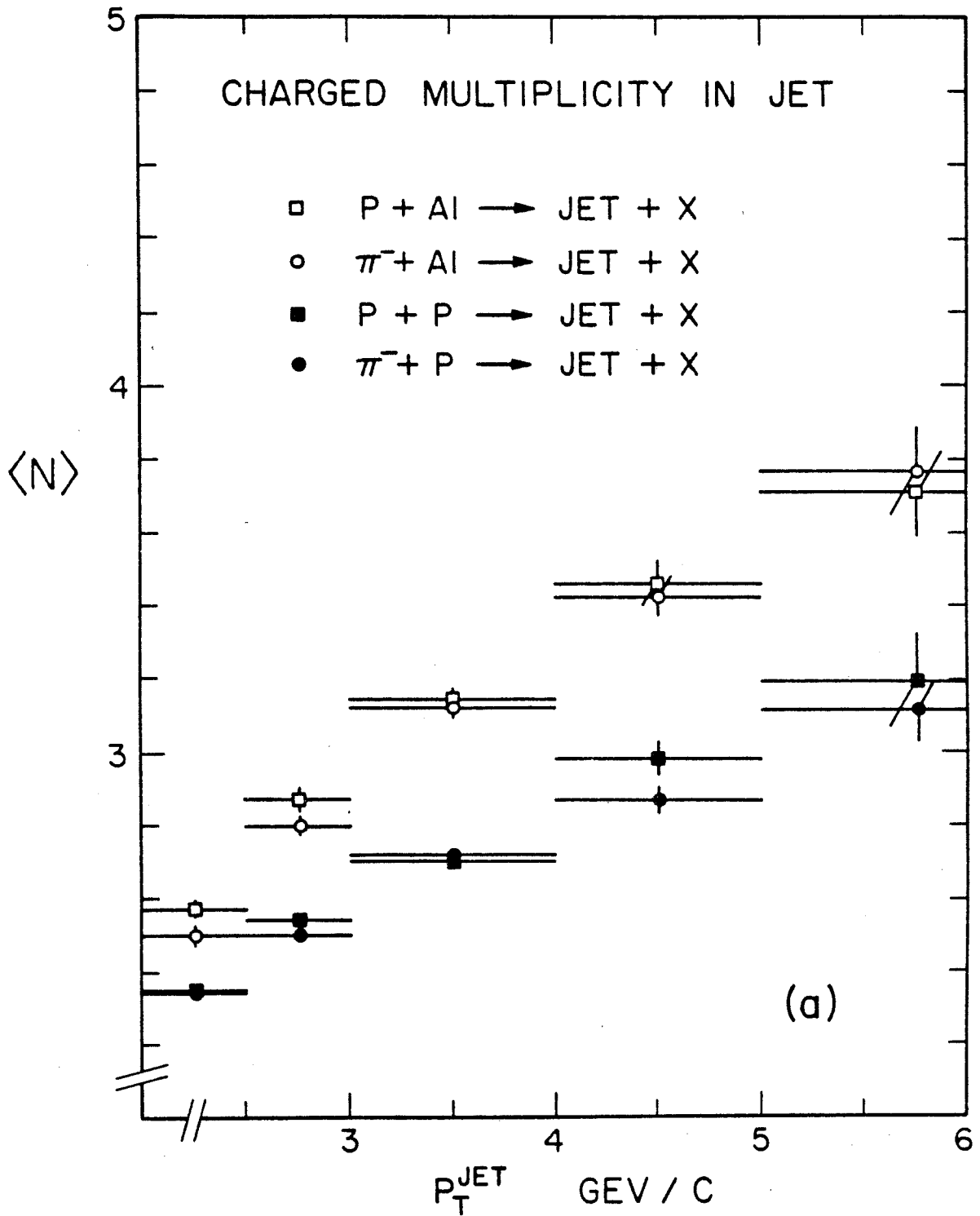
Figure 5.12   Charged multiplicity in the jet vs. jet $P_\perp$ for aluminium and hydrogen targets; p and $\bar{\pi}$ beams.

Figure 6.1 Multiplicity density function $D(\theta_{xx})$

of the associated charged particles with energy

greater than 0.5 Gev in the C. M. Jet Frame

(defined in section 6.1).   These plots do not

have any acceptance correction.

PROTON   HY
ALL CHARGES $E_Q > .5$
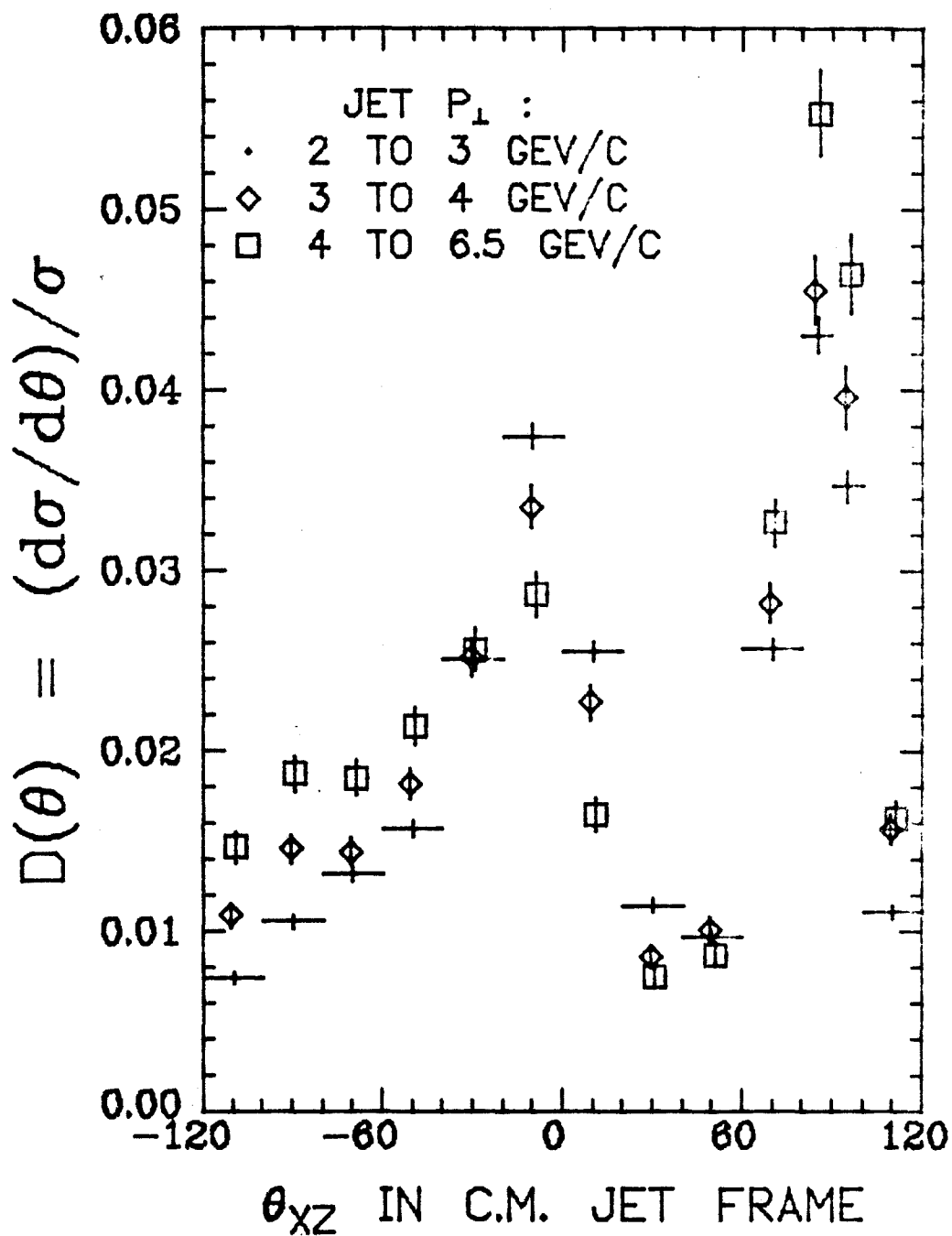
Figure 6.1a Proton beam, hydrogen target.

PROTON AL
ALL CHARGES $E_Q > .5$
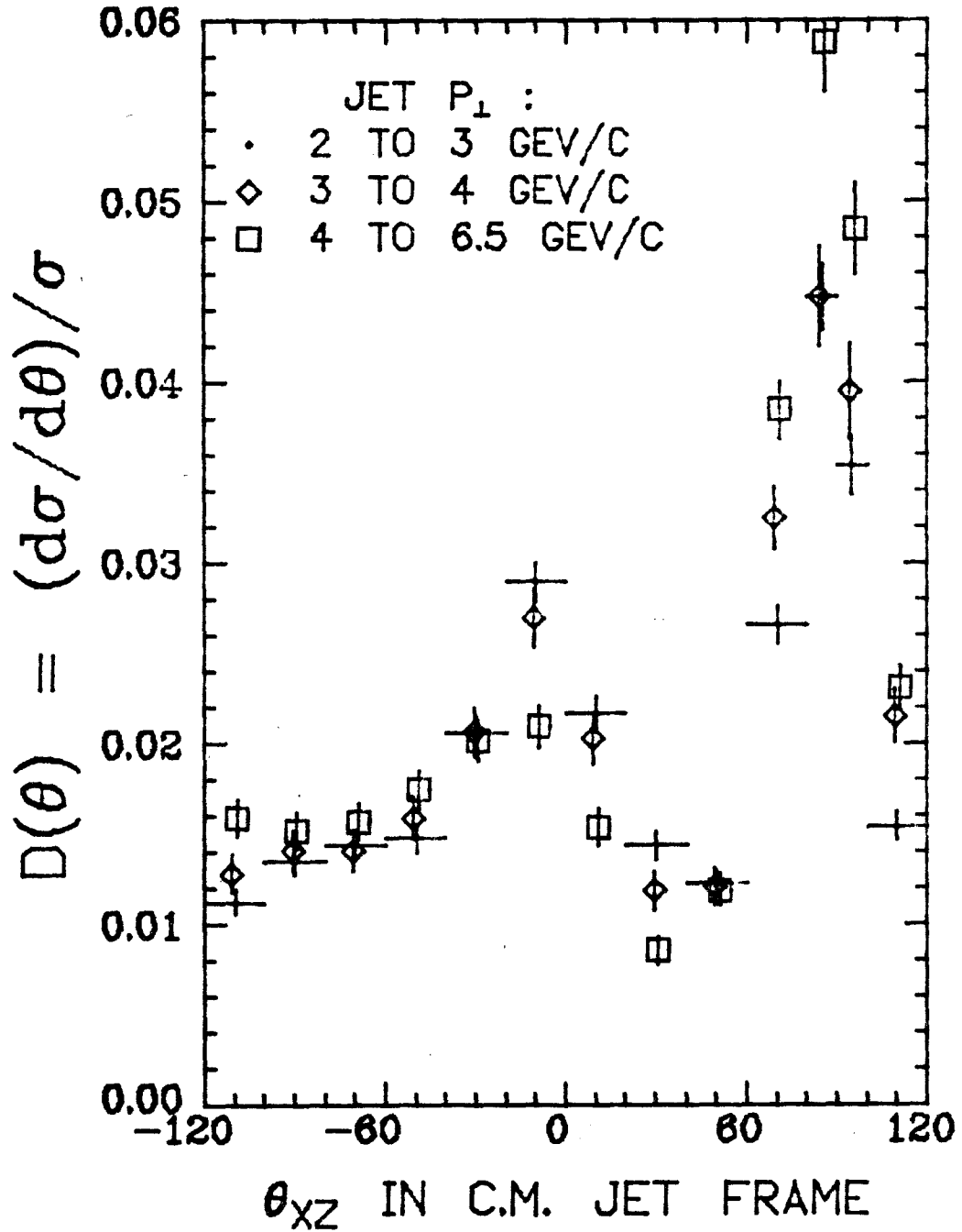
Figure 6.1b Proton beam, aluminium target.

Figure 6.1c π^+ beam, hydrogen target.

π^+ AL
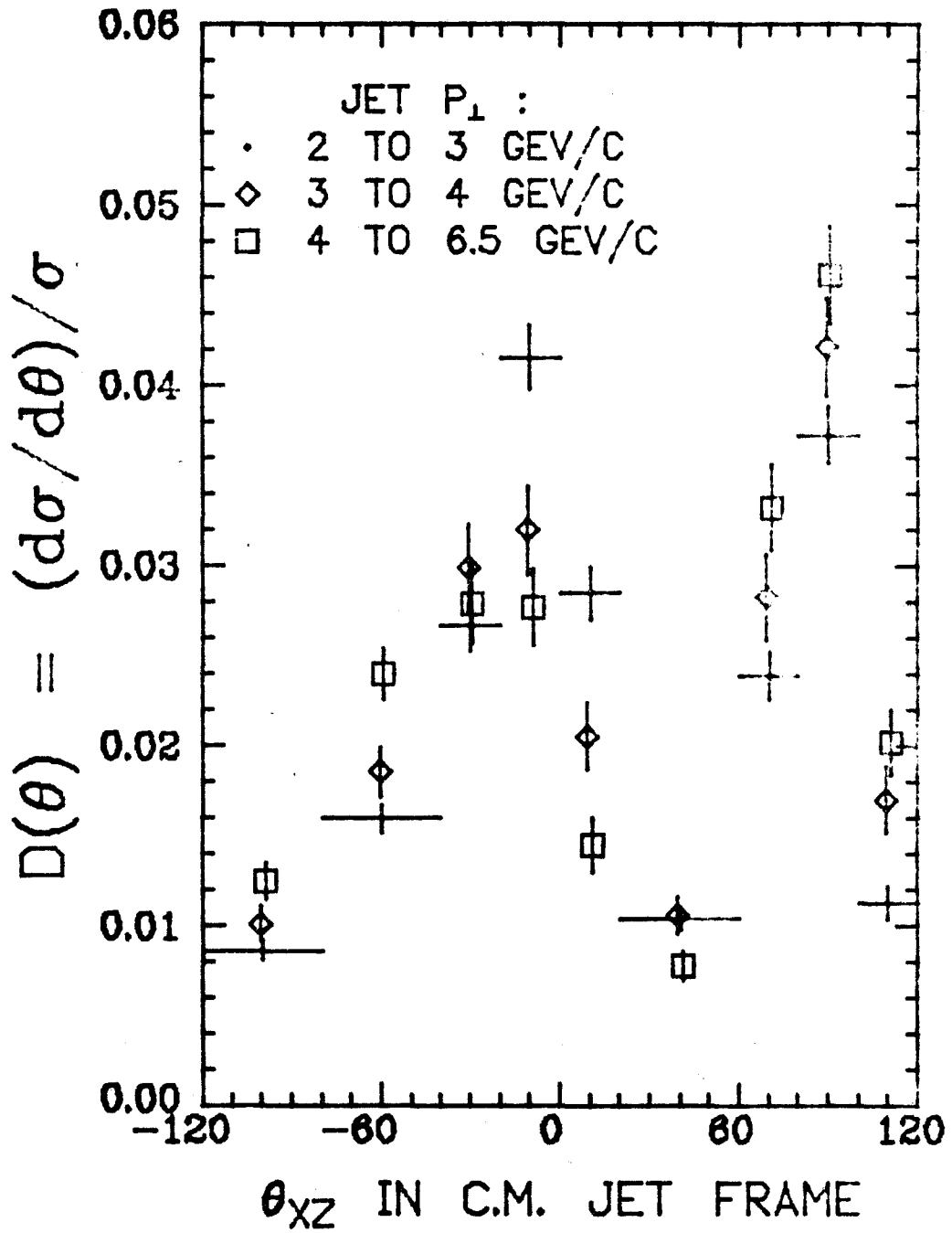
ALL CHARGES $E_Q > .5$

Figure 6.1d π^+ beam, aluminium target.

Figure 6.1e π^- beam, hydrogen target.

π^- AL
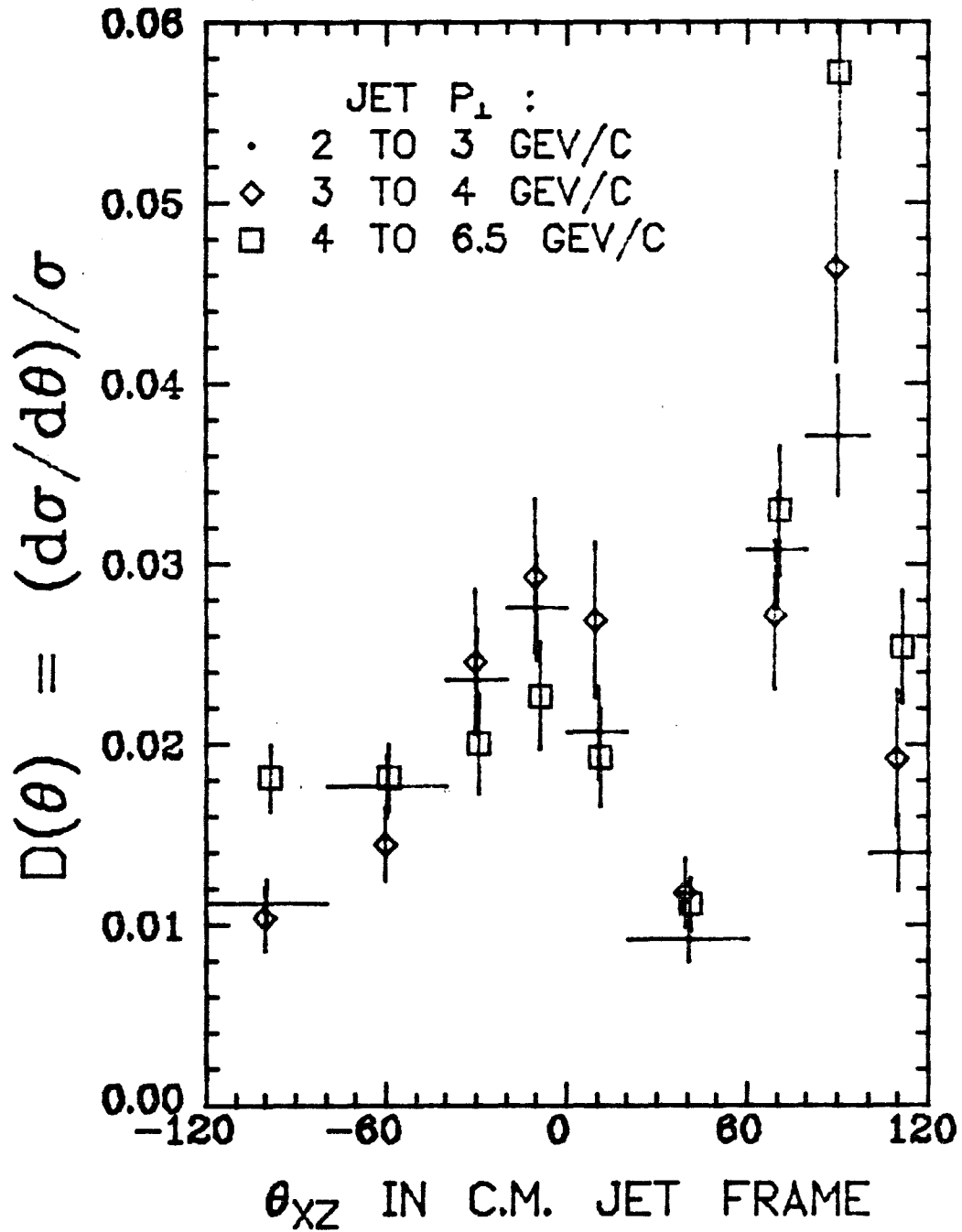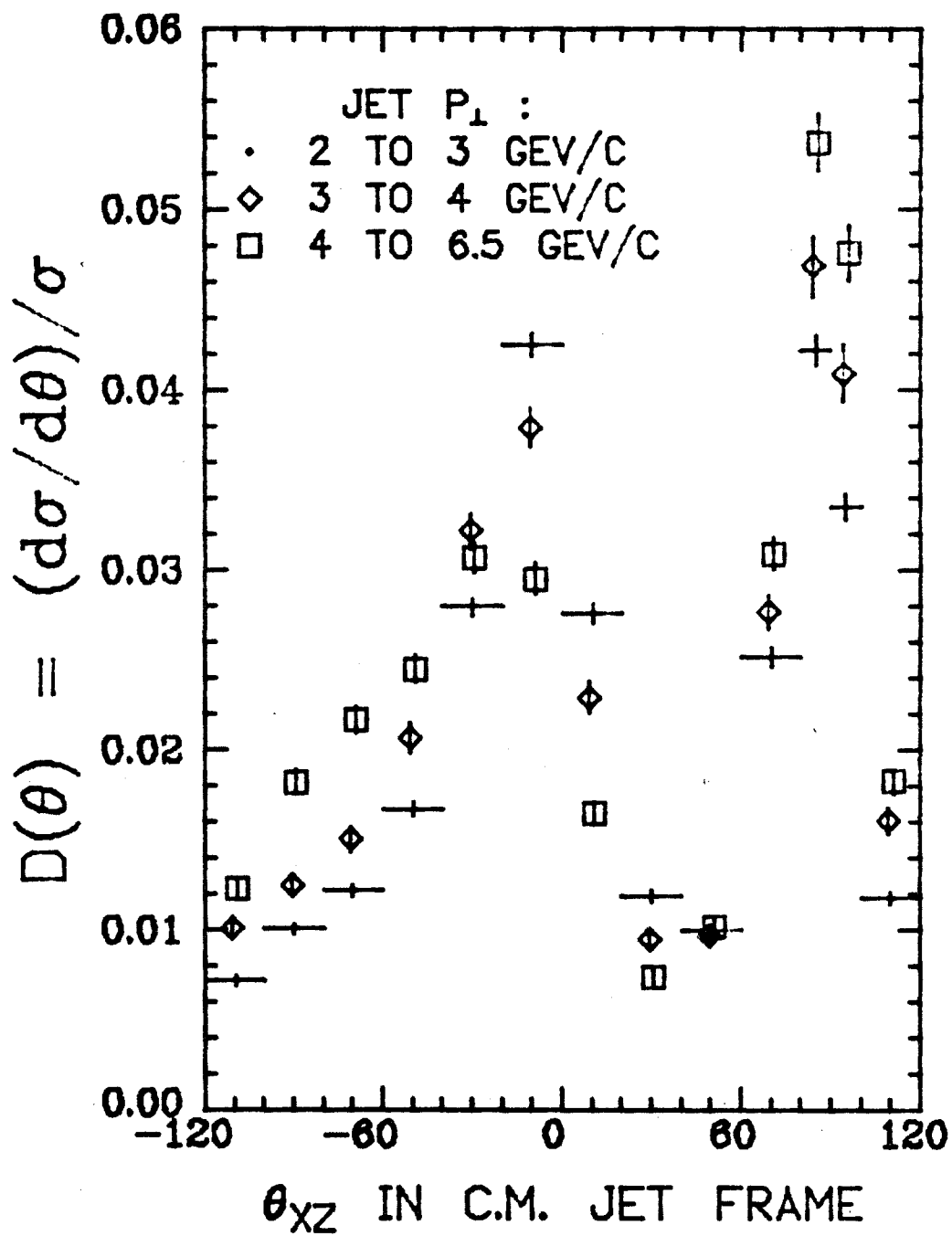
ALL CHARGES $E_Q > .5$
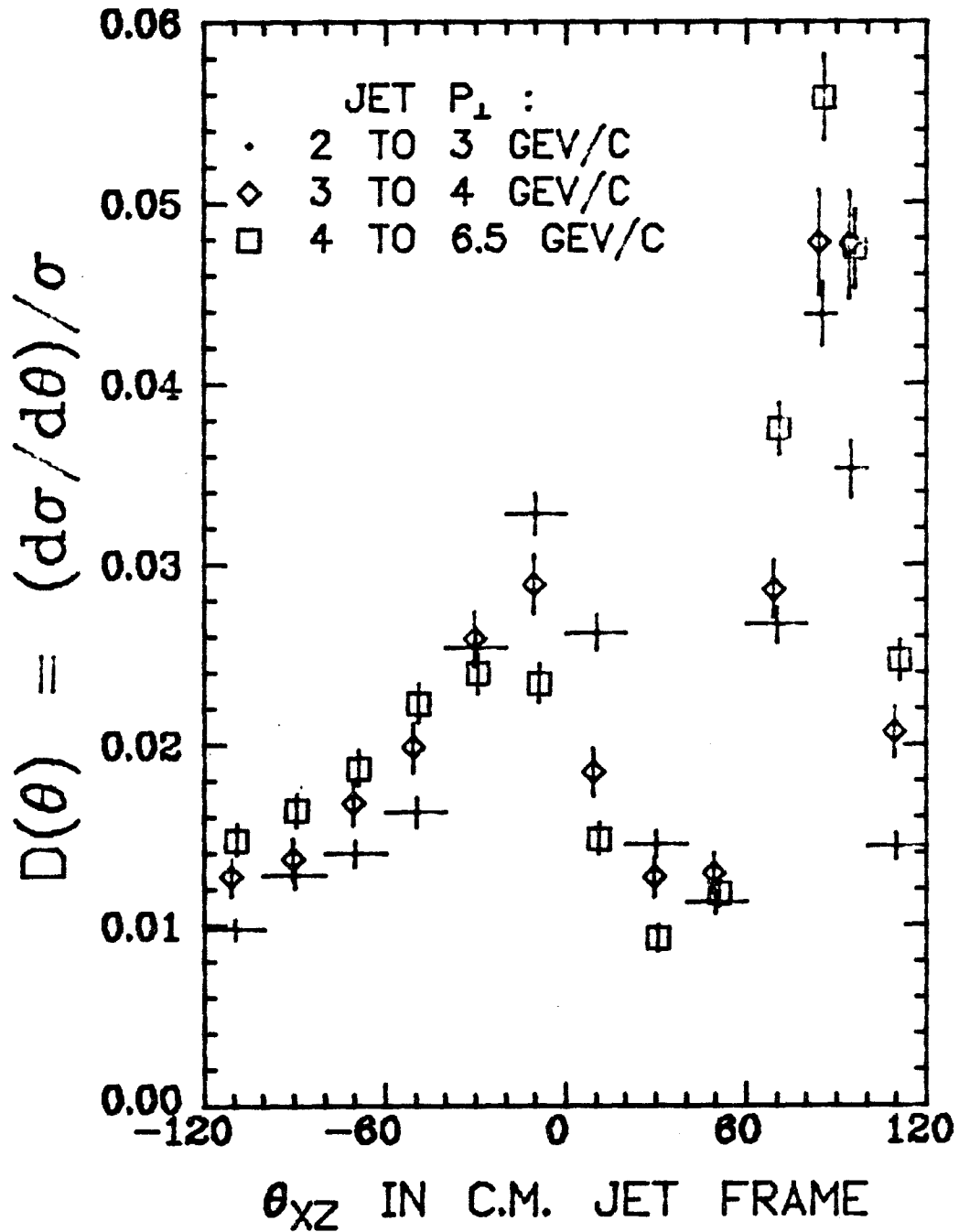
Figure 6.1f π^- beam, aluminium target.

PROTON BEAM $0 < E_Q < .5$
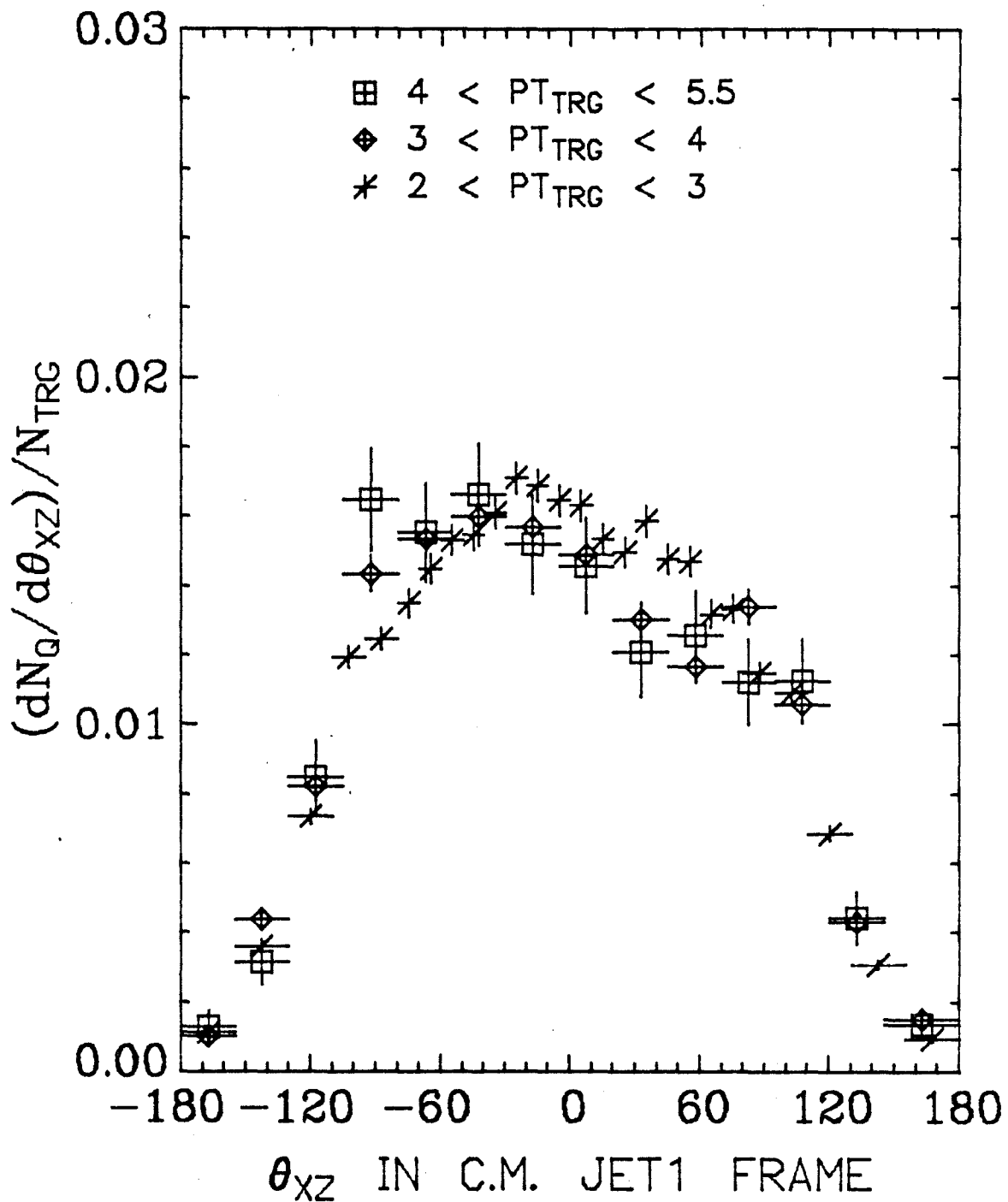
Figure 6.2 $D(\theta_{XZ})$ for lower energy particles (E<0.5).

Figure 6.3   This D(θ_{χ_2}) plot is similar to
those in Figure 6.1, only that the data used
here are Monte Carlo simulations.   Our M.C.
program uses the FFF model [1.6].

MCDATA   PROTON
ALL CHARGES $E_Q > .5$

JET $P_\perp$:
·   2 TO 3 GEV/C
◇   3 TO 4 GEV/C
□   4 TO 6.5 GEV/C

$D(\theta) = (d\sigma/d\theta)/\sigma$

θ_{XZ} IN C.M. JET FRAME
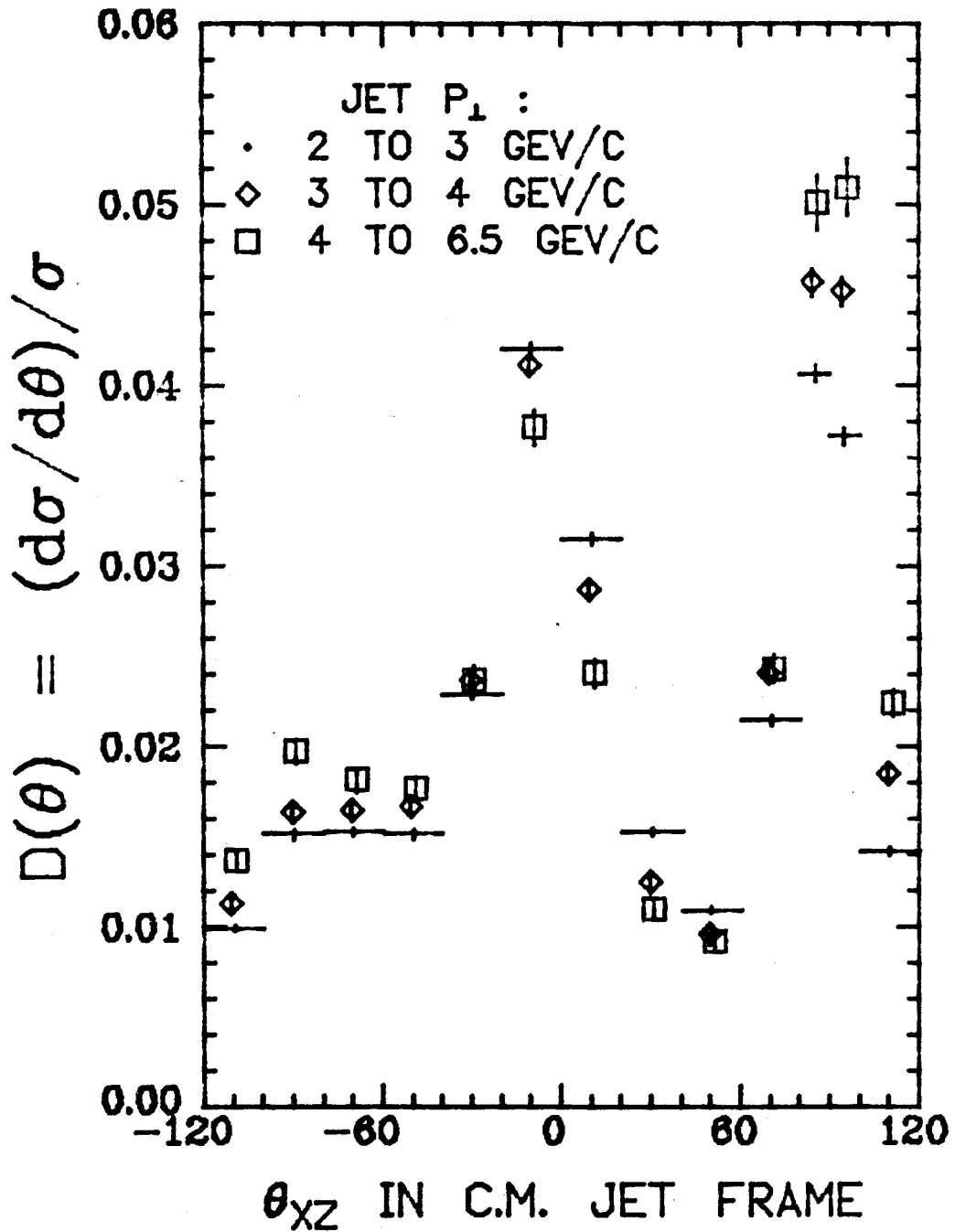
Figure 6.3

Particle density in the spatial X-Y space

(at the 5 position of 2X2) before and after

cuts.   The square box shown in the figure

is where the 2 X 2 is.
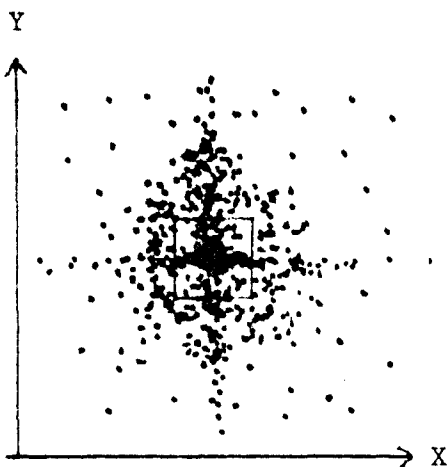
Figure 6.4a   Before any cut.
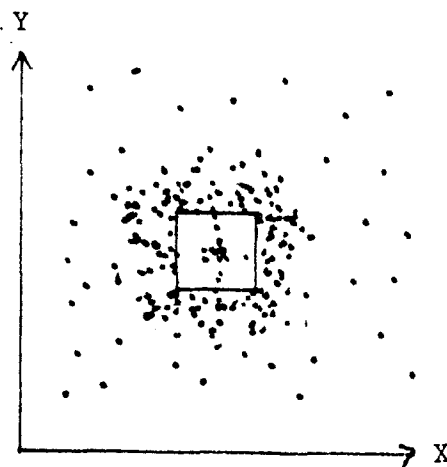
Figure 6.4b   After some PWC quality cuts.

Figure 6.4c,d The ratio of the deleted particle

over the accepted particle as a function of Θ_{xz}

from the Monte Carlo data.

M.C.DATA   PP→4JETS
POSITIVELY   CHARGED

θ_{XZ} IN C.M. JET FRAME
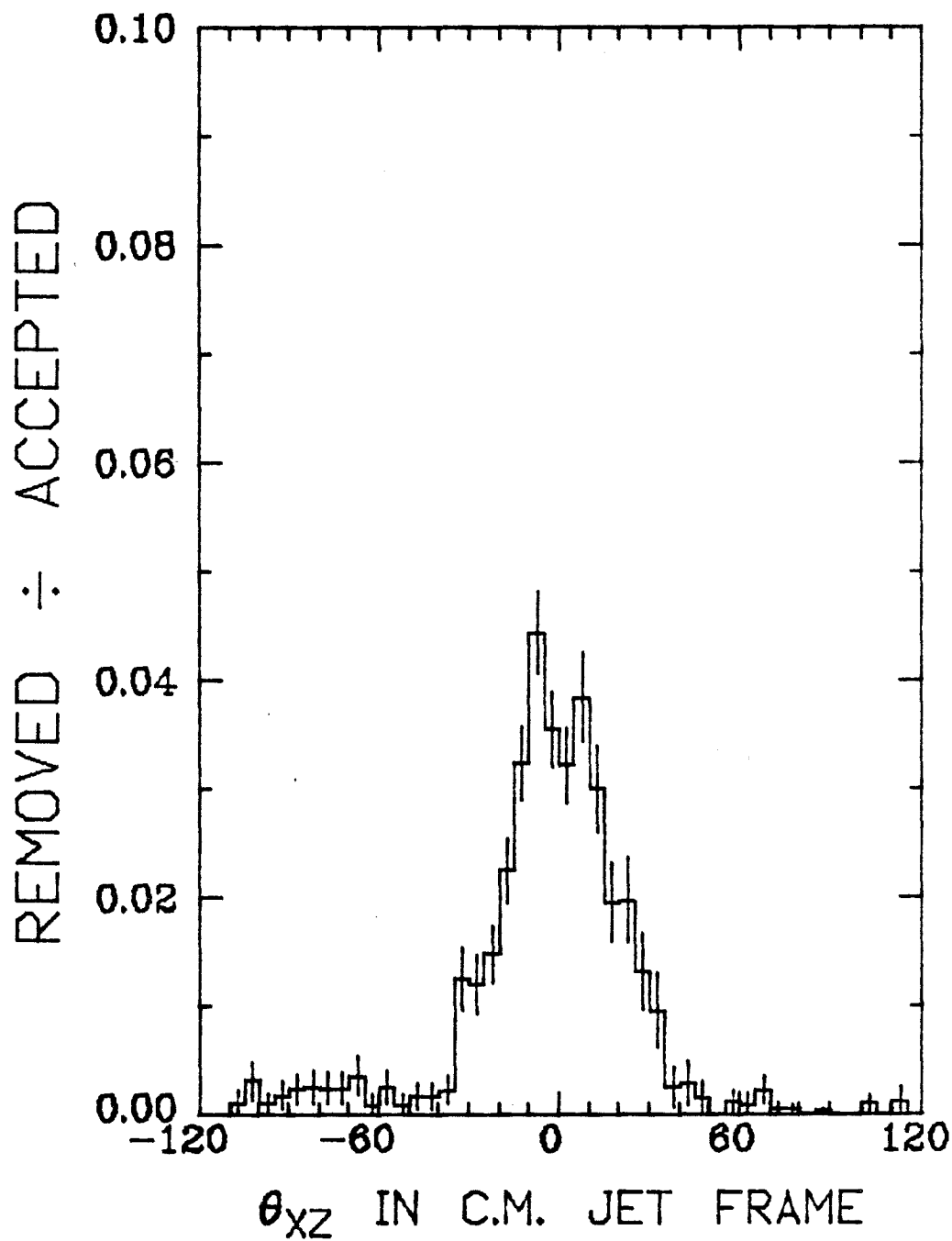
Figure 6.4c

M.C.DATA   PP→4JETS
NEGATIVELY CHARGED
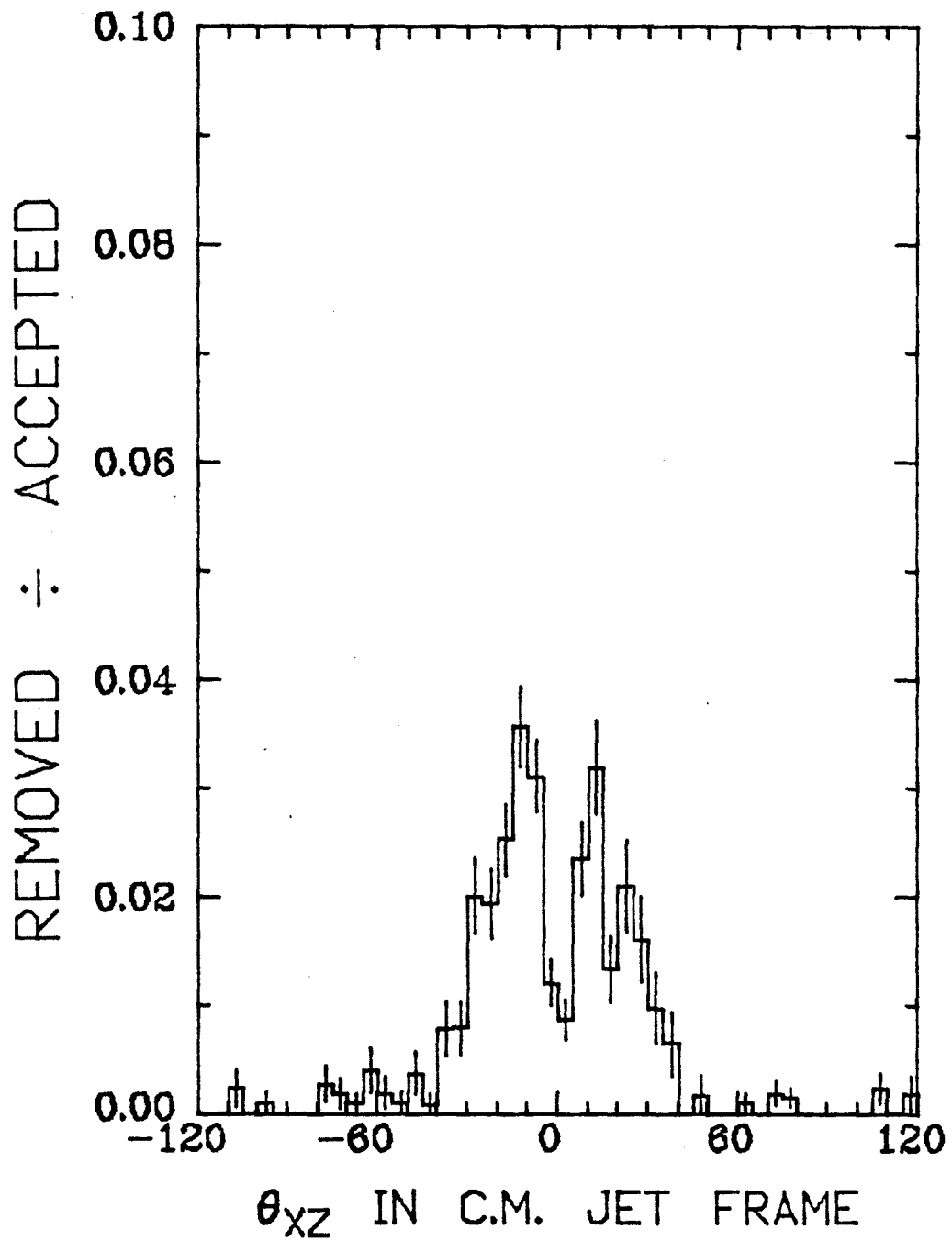
Figure 6.4d

Figure 6.6   The number of positively charged

particles over the number of negatively charged

particles as a function of $\theta_{x\underline{z}}$ for three values

of Q_{JET}. Q_{JET} is defined in the text (section

6.3).   Only particles with $E > 0.5$ are included.
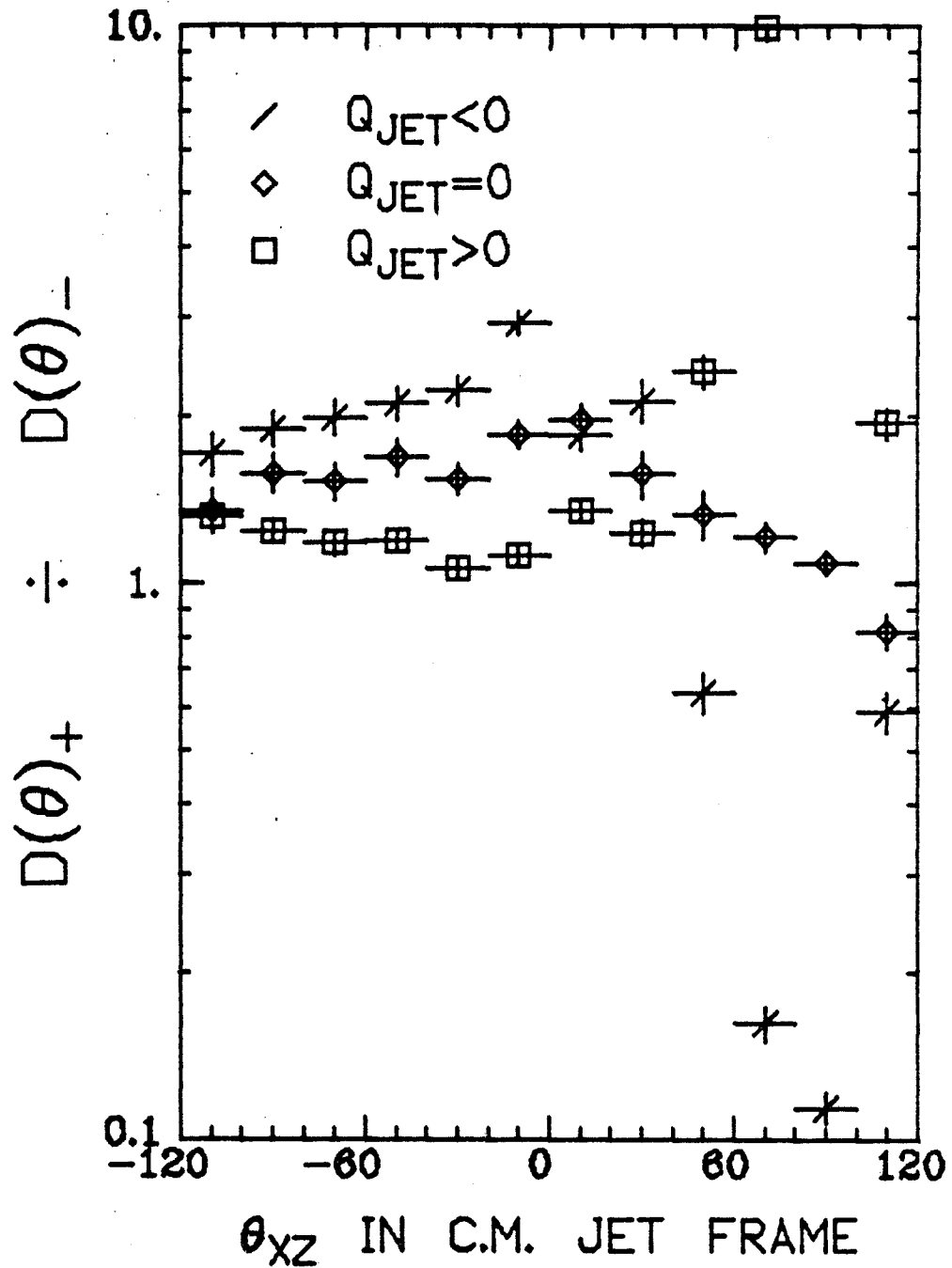
Figure 6.6a Proton beam, hydrogen target.

165
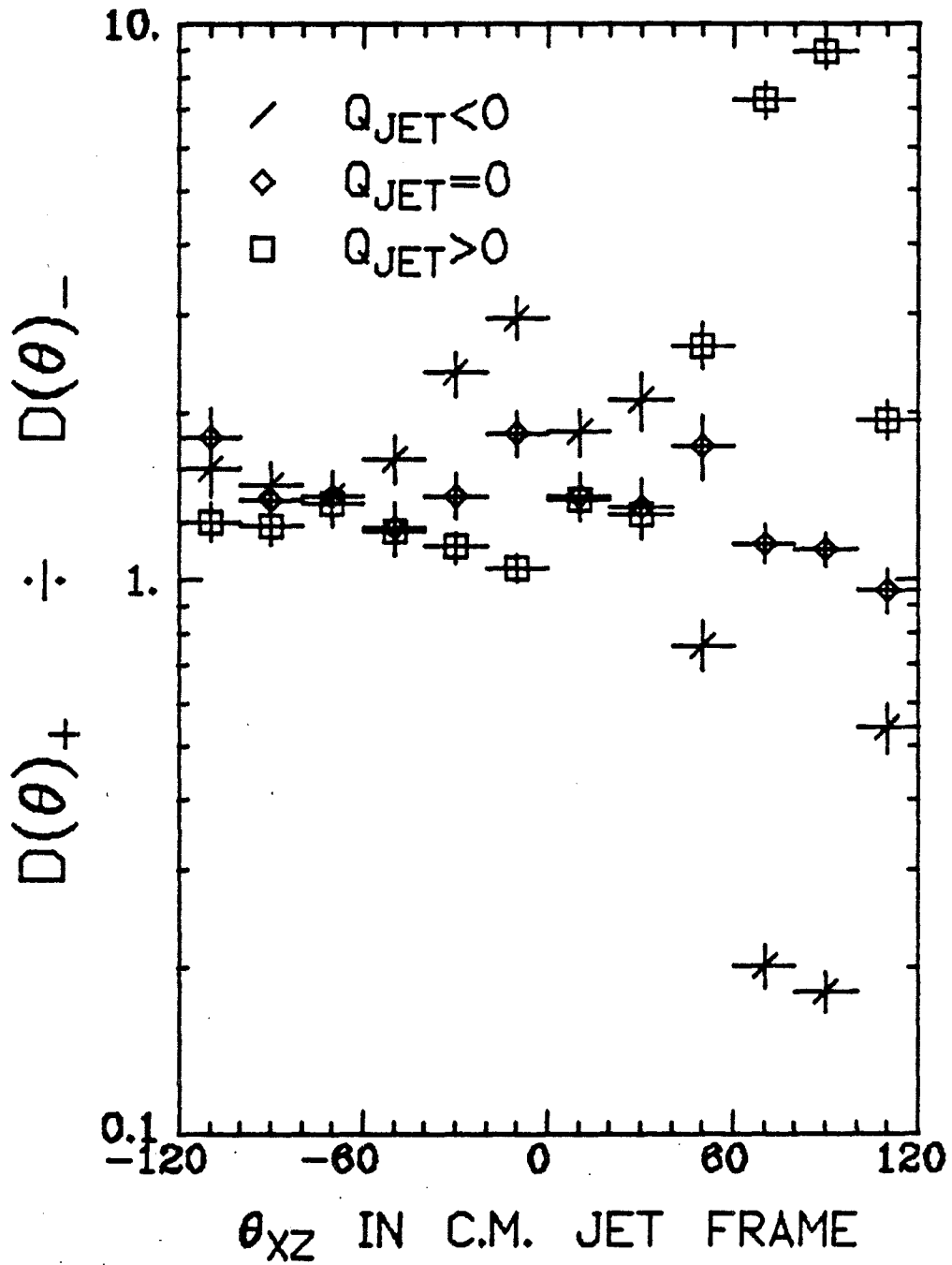
Figure 6.6b Proton beam, aluminium target.
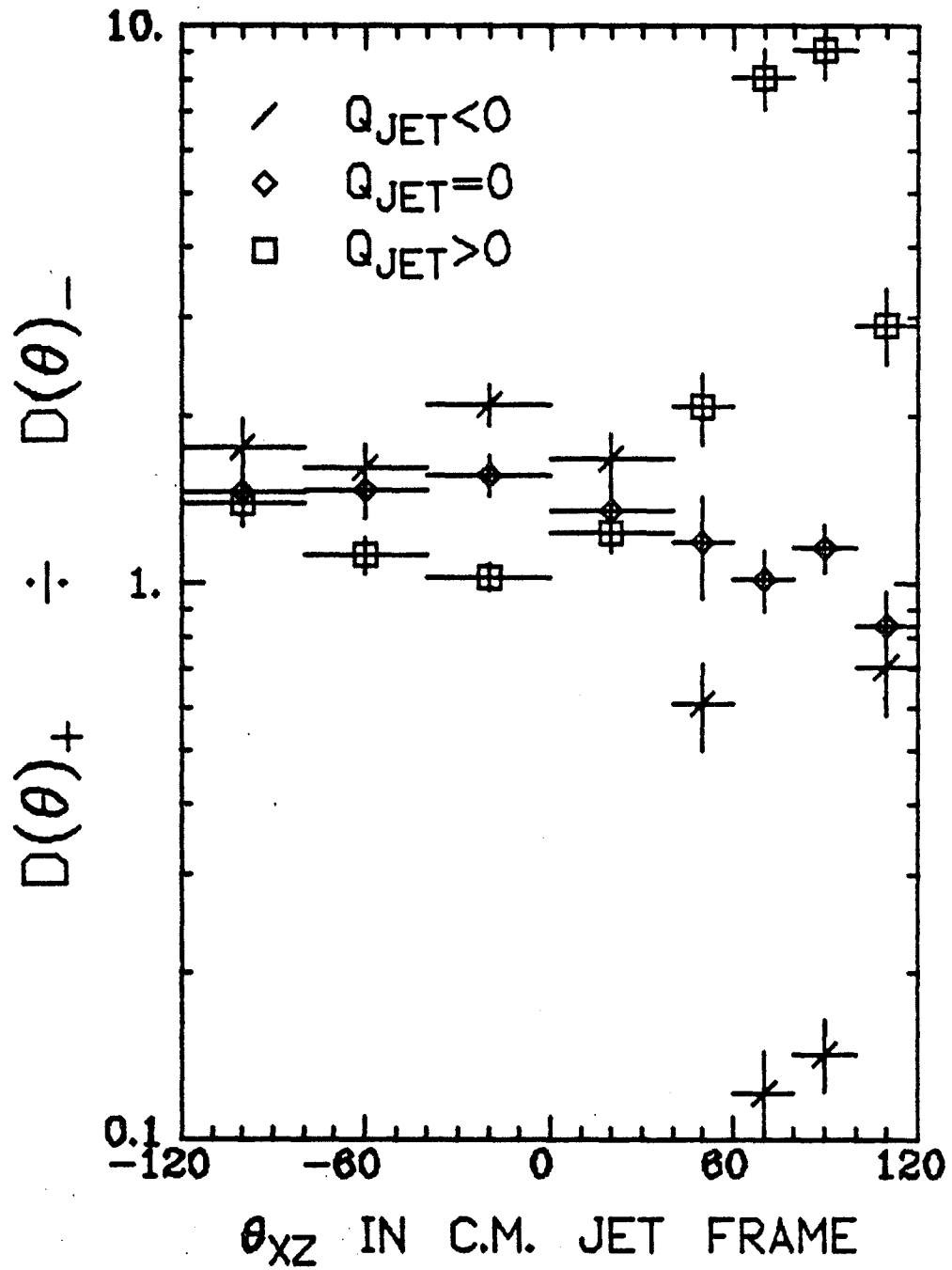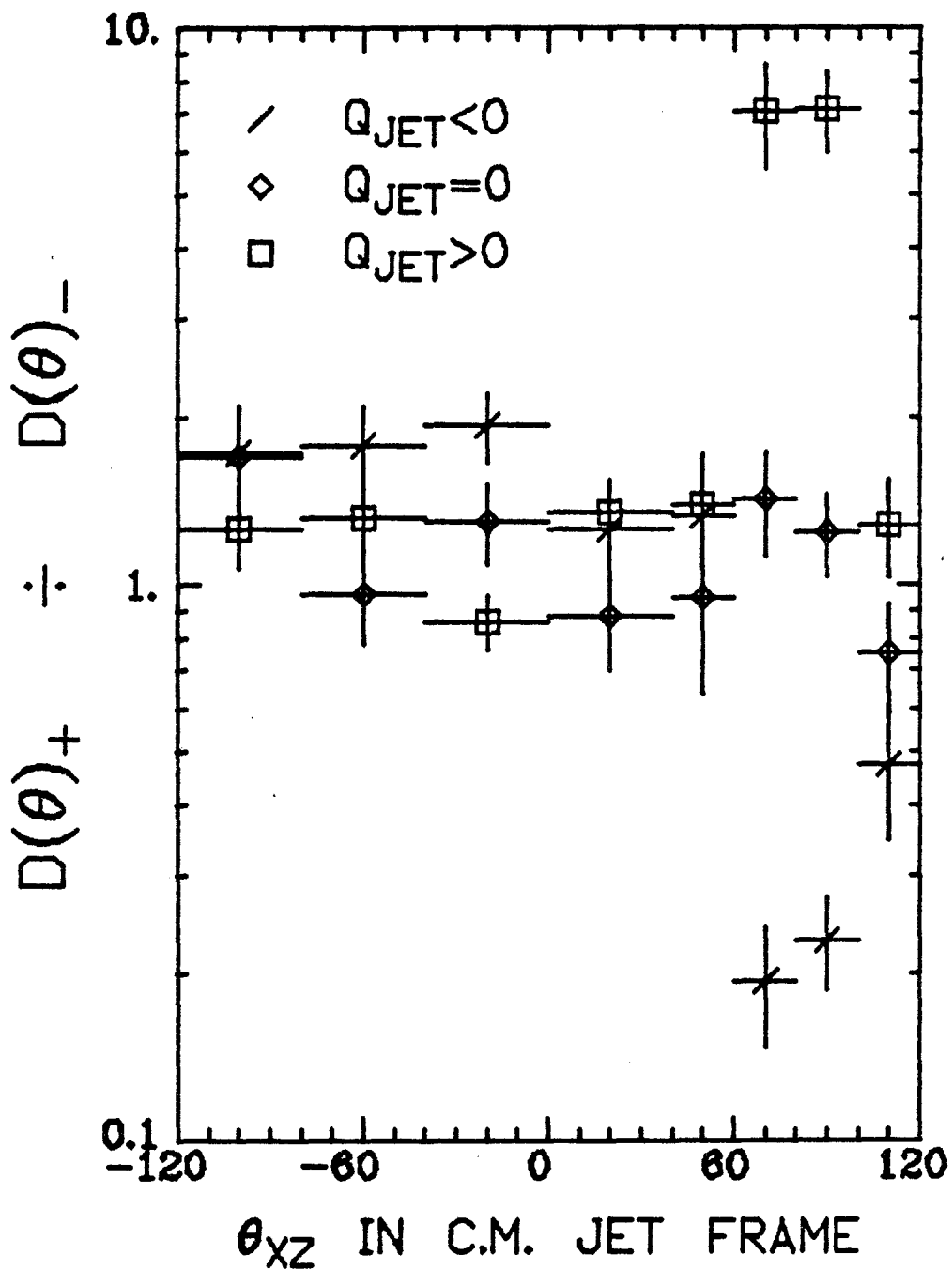
Figure 6.6c π^+ beam, hydrogen target.

Figure 6.6d π^+ beam, aluminium target.

π^- HY E_a>.5

HIJT $P_\perp^{JET}$ 2 TO 6.5 GEV/C

Figure 6.6e π^- beam, hydrogen target.
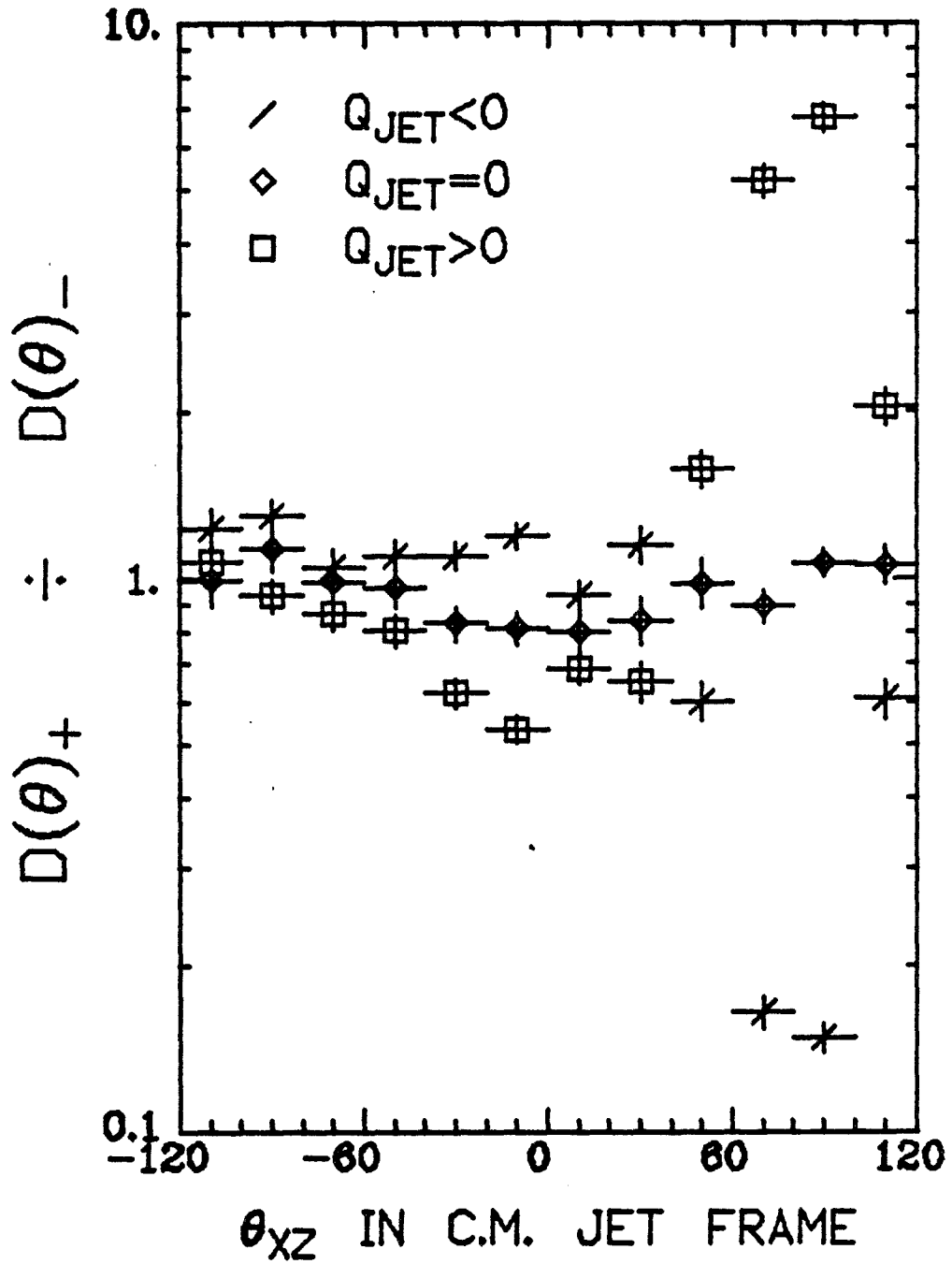
Figure 6.6f π^- beam, aluminium target.
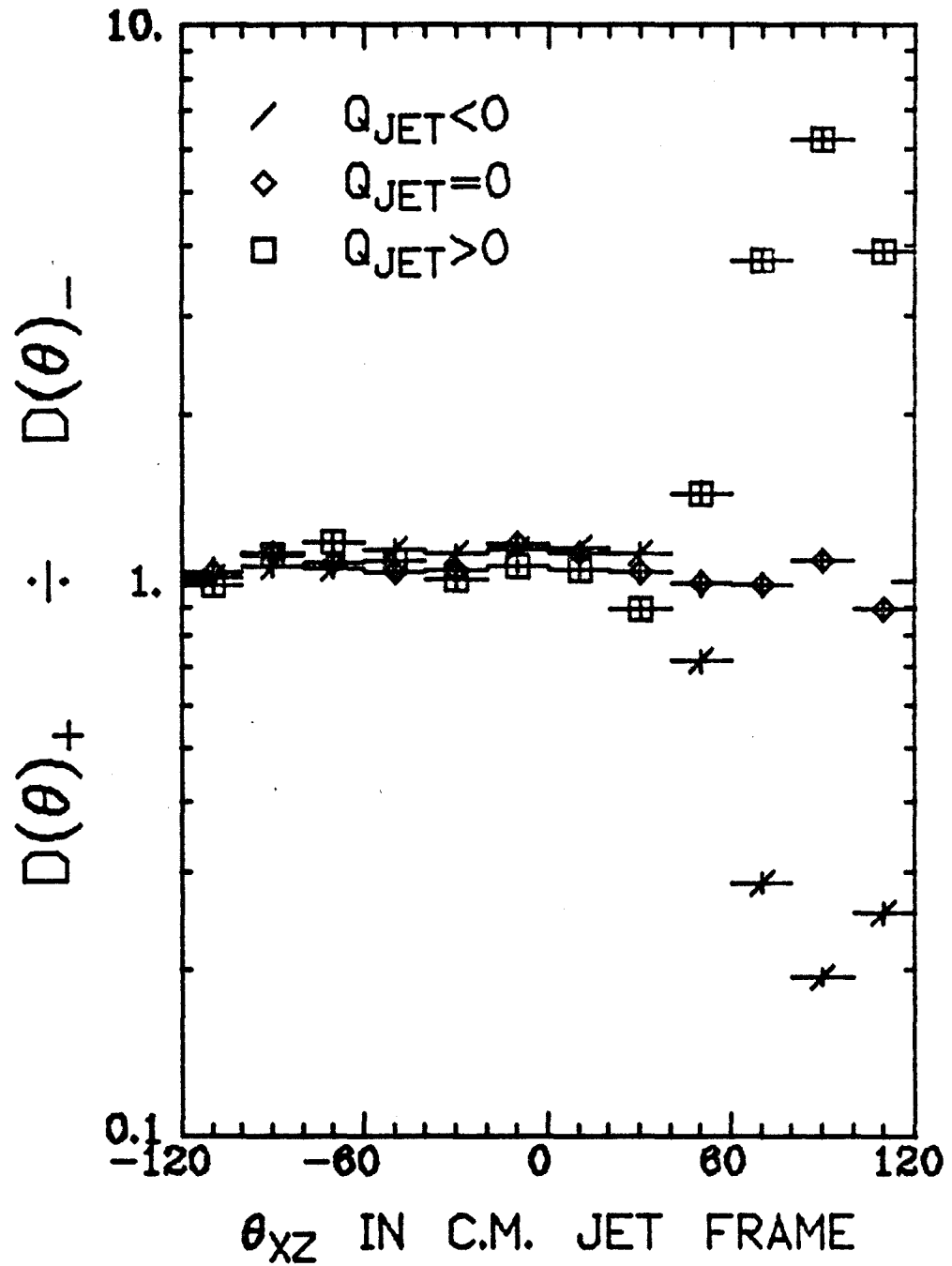
Figure 6.7   +/- ratios for our M.C. data.

Please see figure caption for Figure 6.6.

POS BEAM   HIJT $E_Q > .5$
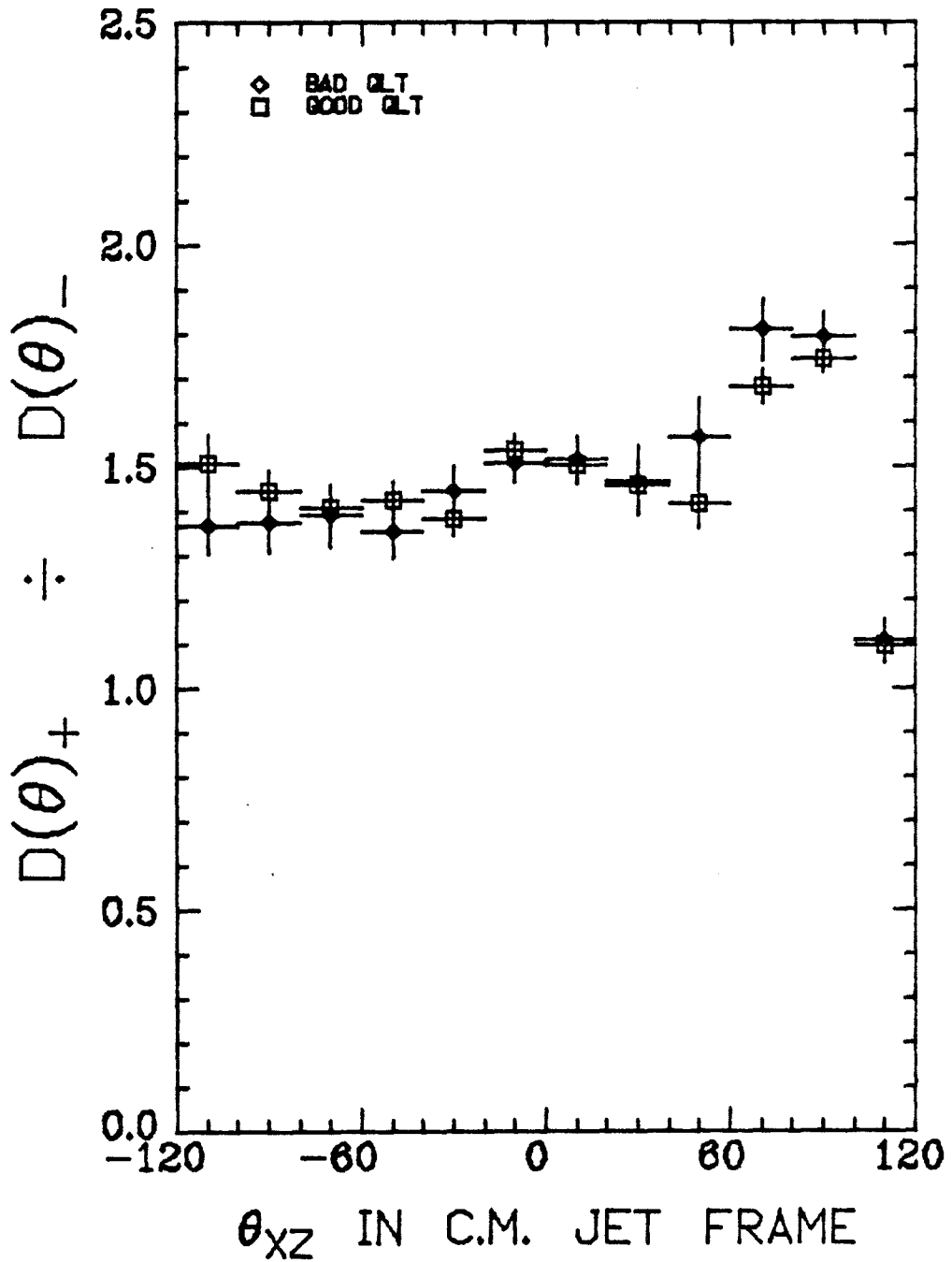
Figure 6.8   +/- ratios for two ranges of

PWC quality factors (PWCNCE).

HYDROGEN TARGET
ALL CHARGES $E_Q > .5$
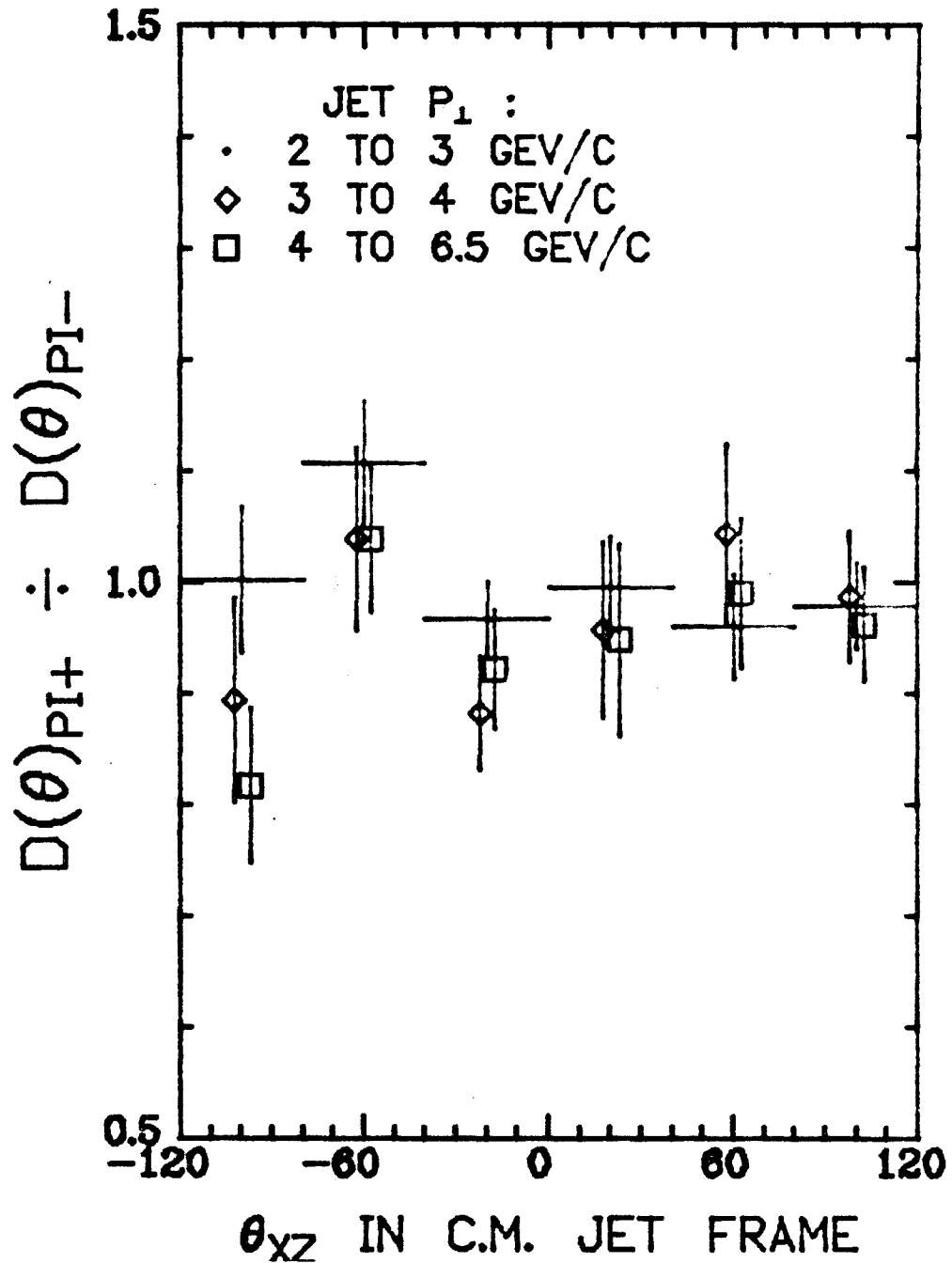
Fig. 6.9a Ratio of the $D(\theta)$ distribution for

the π^+beam over the π^- beam (hydrogen).

ALUMINIUM TARGET
ALL CHARGES $E_Q > .5$
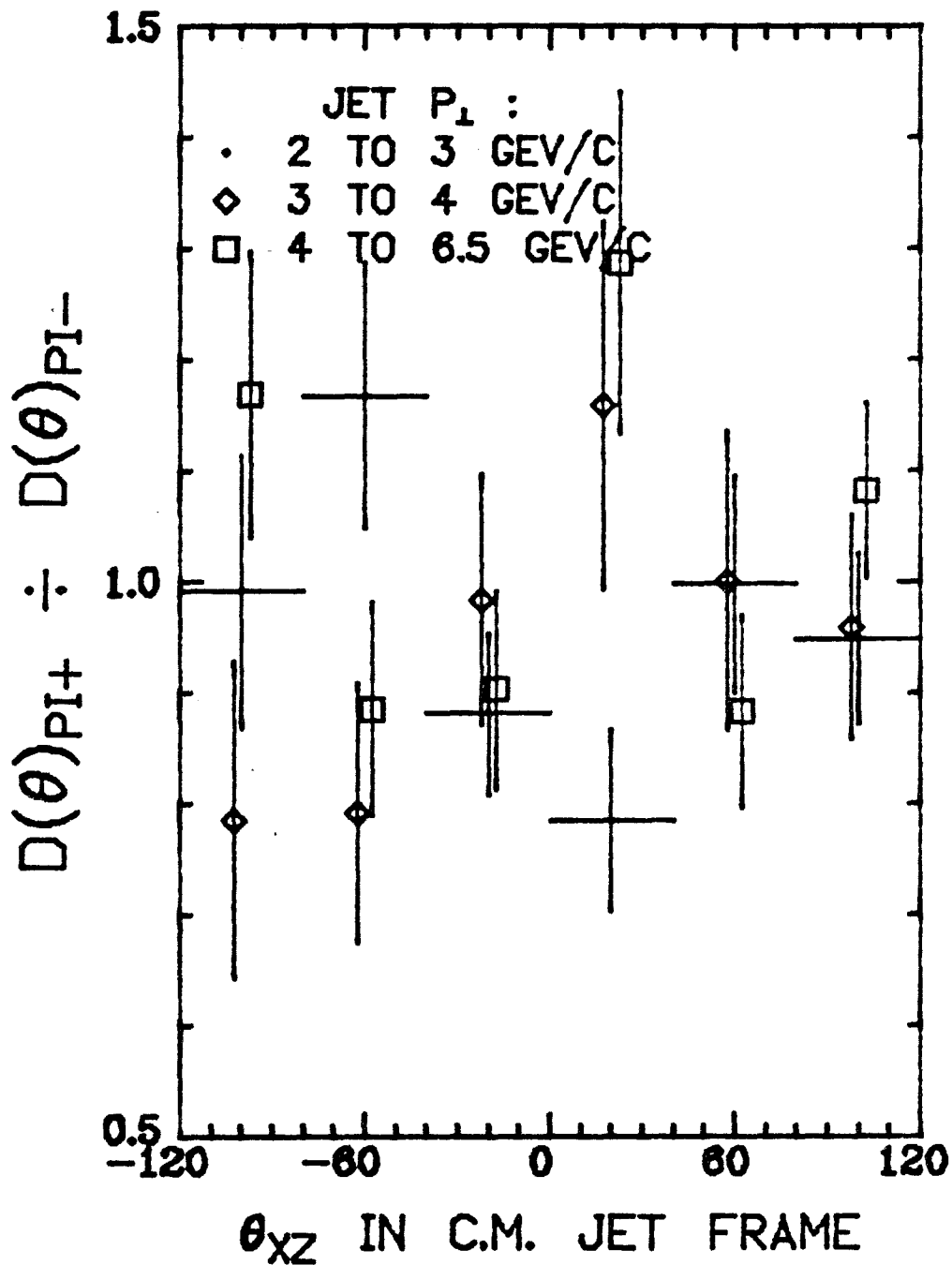
Fig. 6.9b Ratio of the $D(\theta)$ distribution for

the π^+ beam over the π^- beam (aluminium).

HYDROGEN TARGET
ALL CHARGES $E_Q > .5$
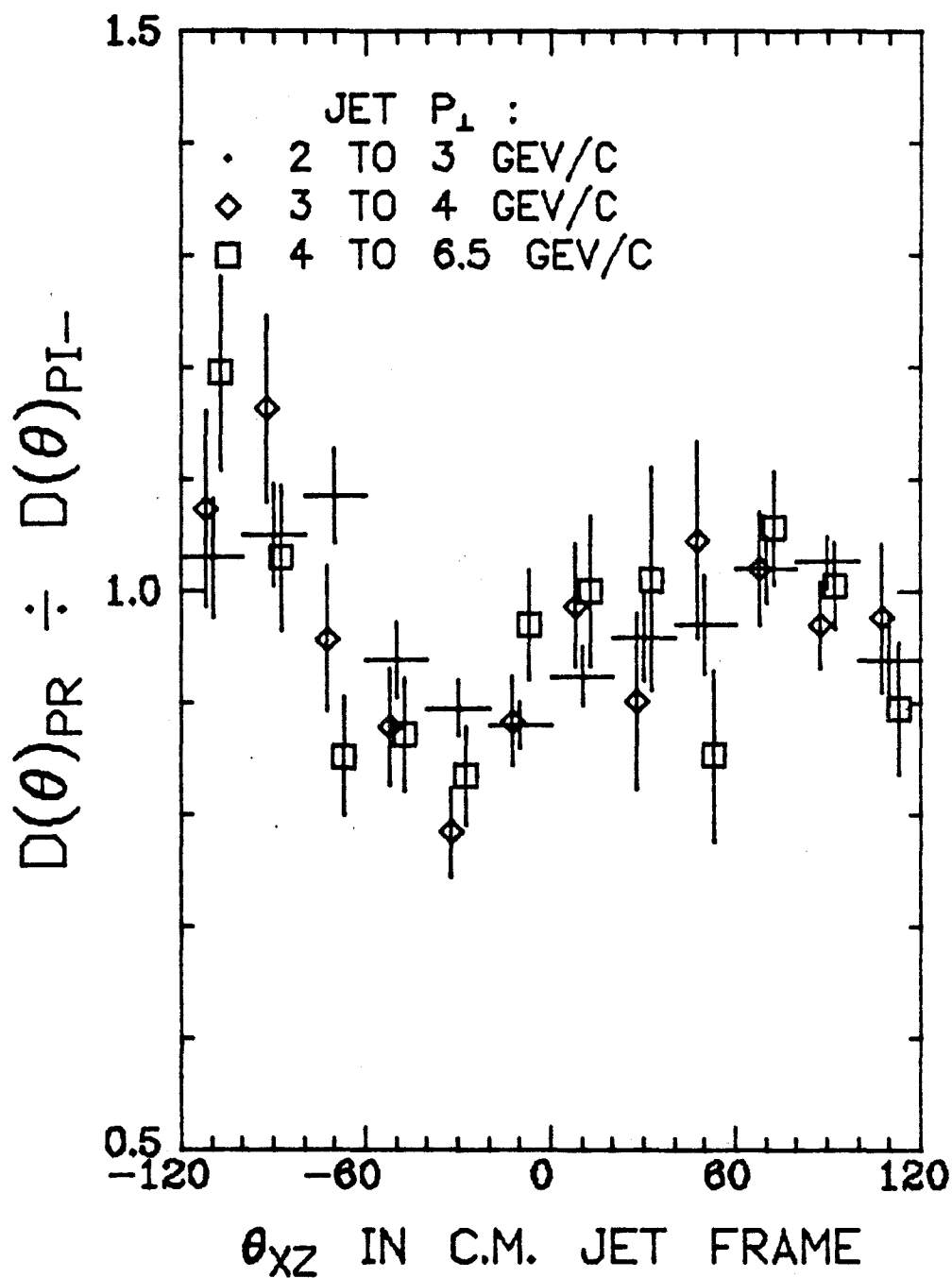
Fig. 6.10a Ratio of D(θ) for the proton beam over the π^- beam (hydrogen target).

ALUMINIUM TARGET
ALL CHARGES $E_Q > .5$
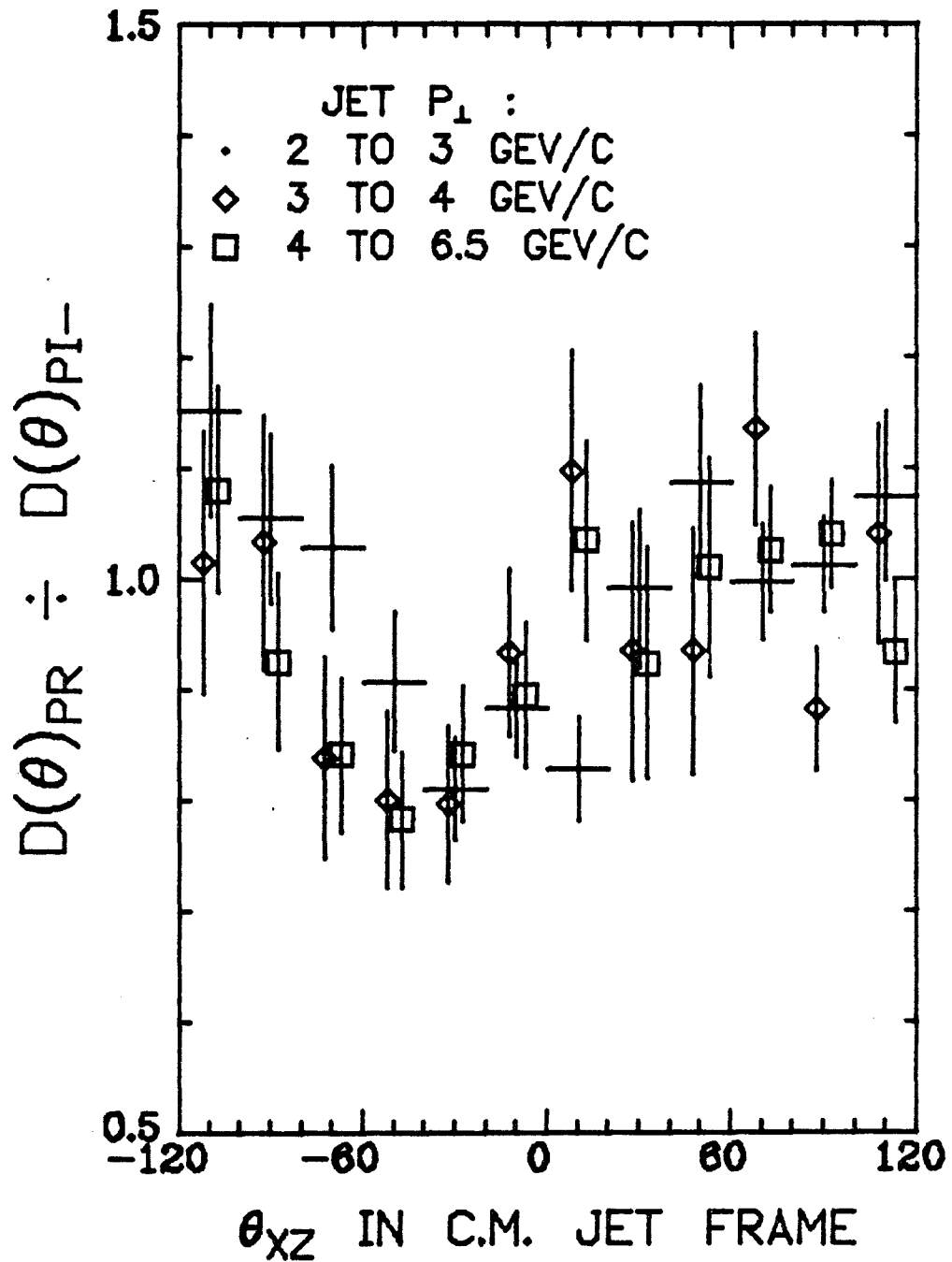
Fig. 6.10b Ratio of D(θ) for the proton beam over the π^- beam (aluminium target).

HYDROGEN TARGET JET
ALL CHARGES ON THE AWAY SIDE
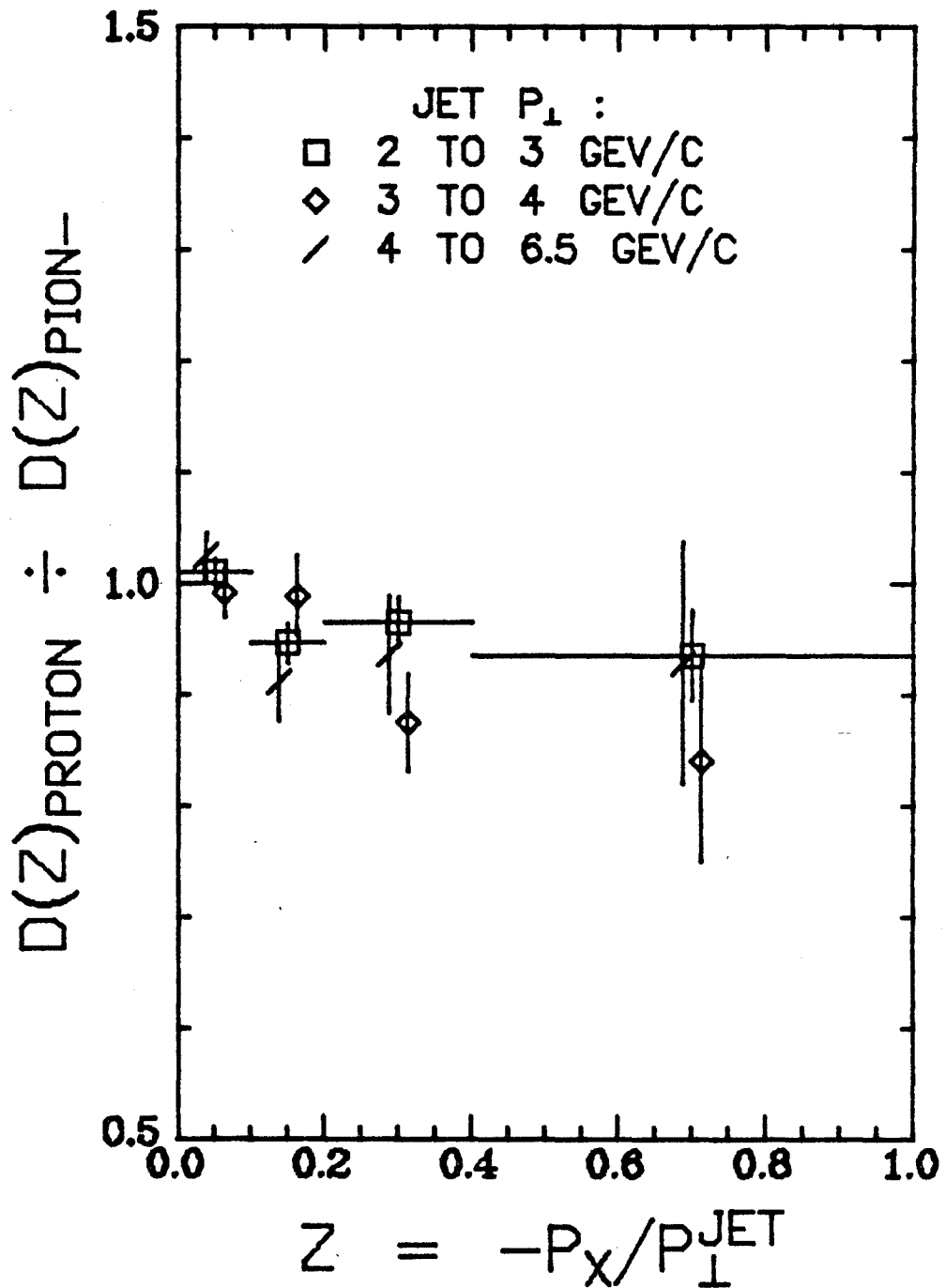
Figure 6.11a Ratio of D(Z) plot for the proton beam over the π^- beam on the away side (hydrogen target).

ALUMINIUM TARGET   JET
ALL CHARGES ON THE AWAY SIDE
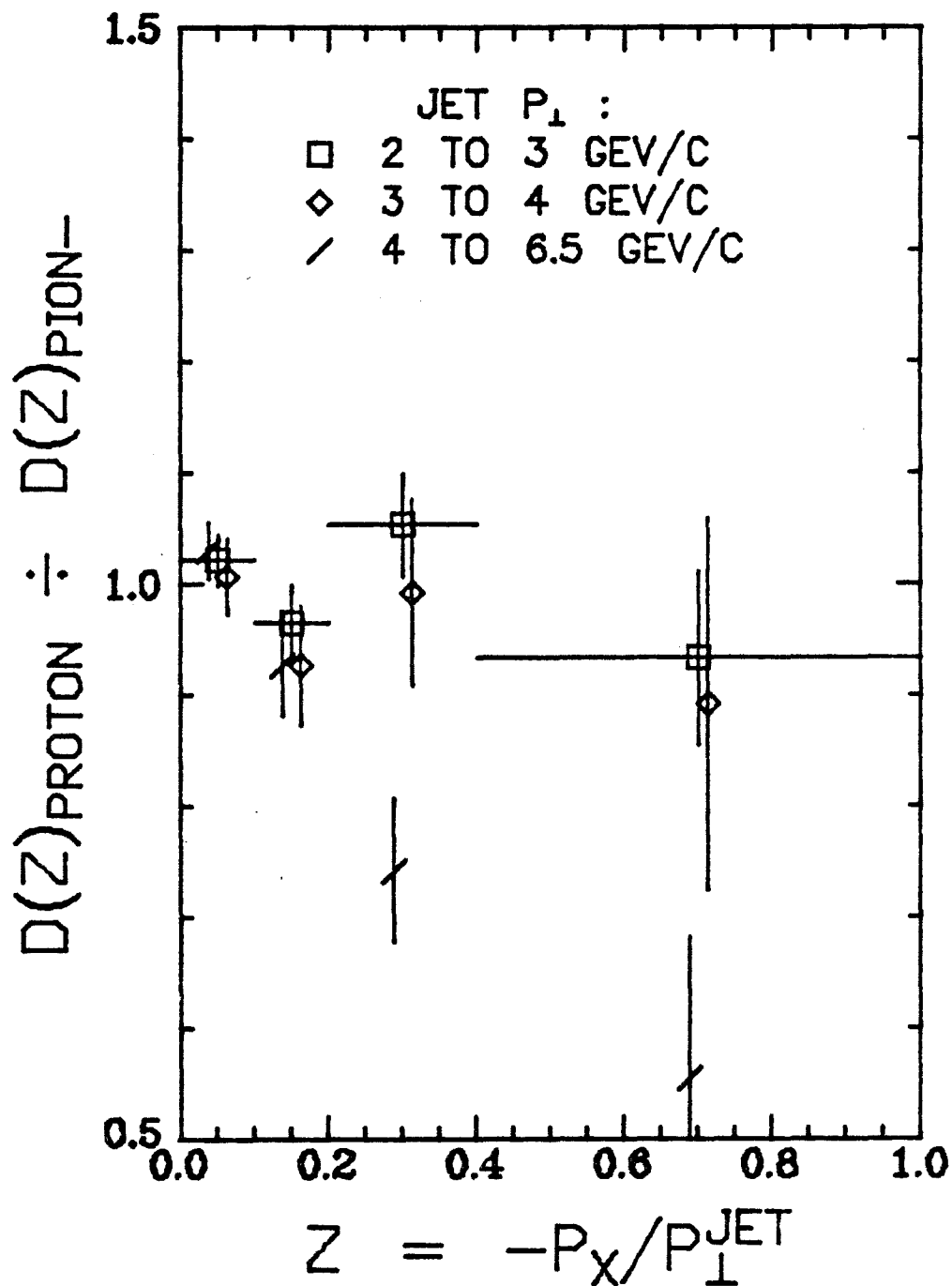
Figure 6.11b Ratio of $D(Z)$ plot for the

proton beam over the π^- beam on the away side

(aluminium target).
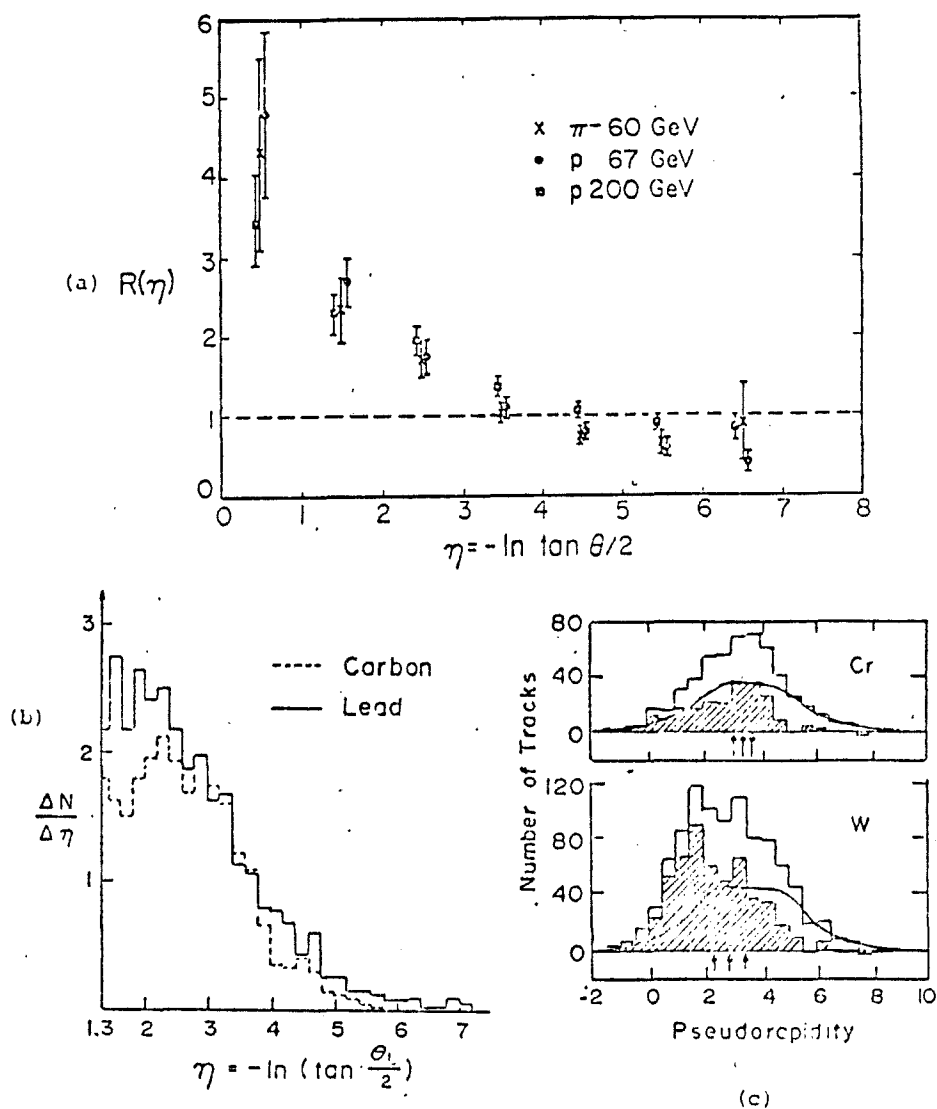
Fig. 11

Data on the A-dependence of leading particle spectrum.
a) Emulsion data. Ratio $R(\eta)$ of number of particles produced in heavy nuclei to that in hydrogen. Identification of target nucleus through parameter N_h discussed in text. Data compiled by Wolter.[41]
b) Spark chamber data of Abrosimov et al.[42] at 40 GeV.
c) Data obtained by Florian et al.[43] using metal pellets in emulsion.

Figure 6.12   Plots taken from page 583 of

the review paper by Wit Busza [1.18a] .

RAPIDITY DISTRIBUTION OF CHARGED PARTICLES ON BOTH SIDES

O   MINIMUM BIAS

······"UNIVERSAL CURVE"
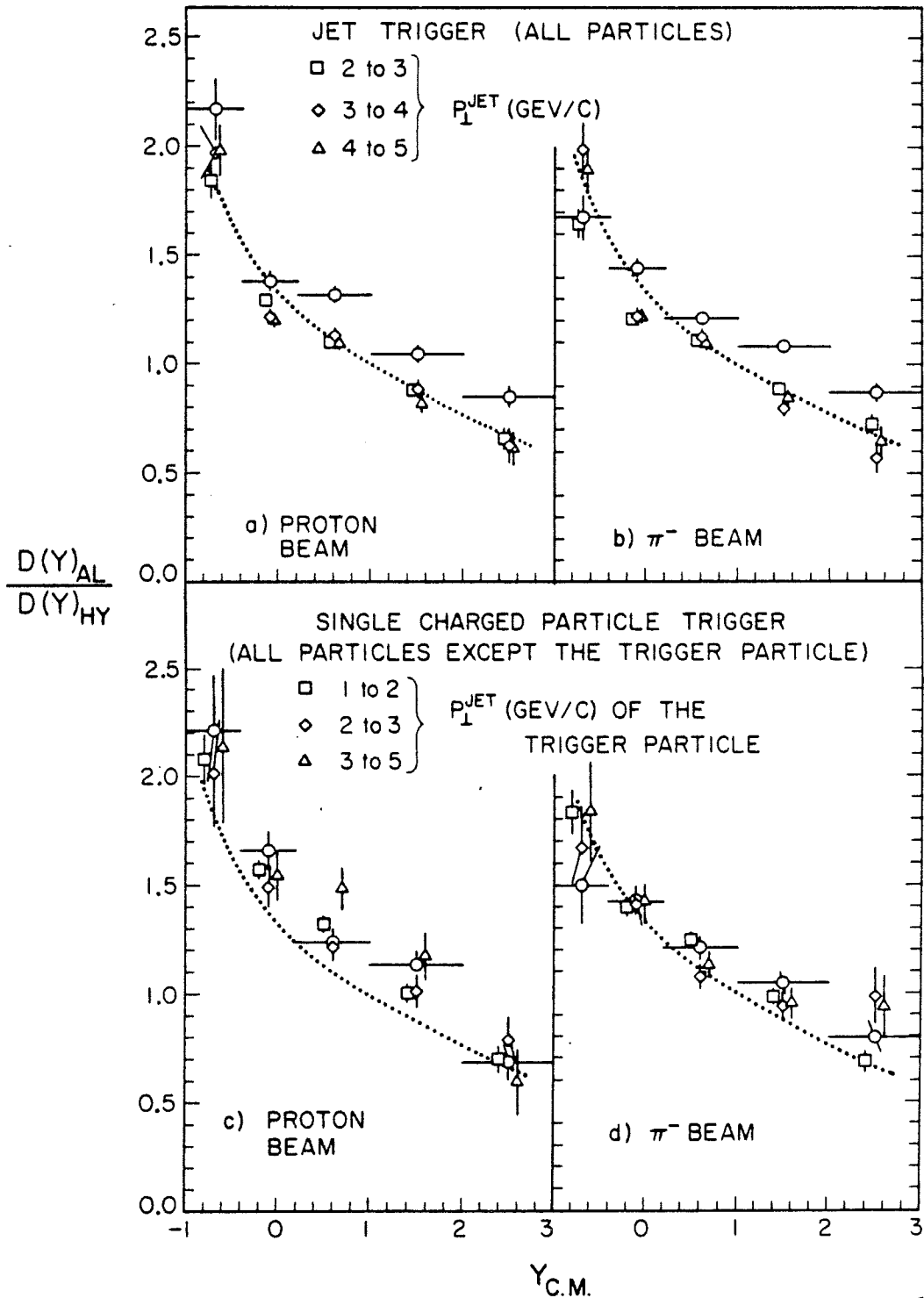
Figure 6.13 Ratio of D(Y) (aluminium over hydrogen) for charged particles on both sides(trigger particle excluded in the single particle trigger).

RAPIDITY DISTRIBUTION OF ALL CHARGED
PARTICLES ON THE AWAY SIDE

○ MINIMUM BIAS

···· "UNIVERSAL CURVE"
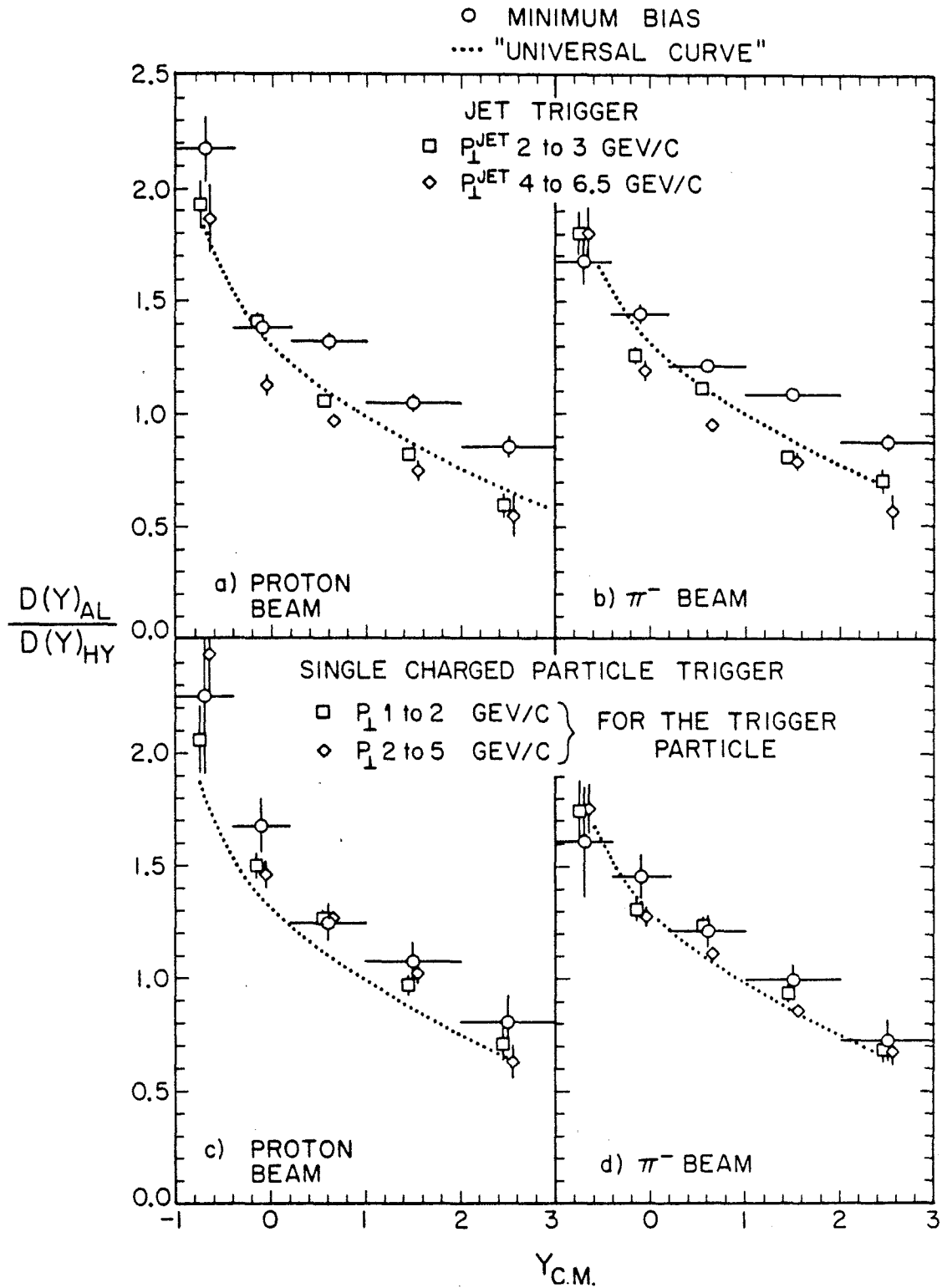
Figure 6.14   Ratio of D(Y) (.aluminium over hydrogen) for all charged particles on the away side.

Figure 6.15   D(Y) for the aluminium target

and for three different vertex regions of

the hydrogen target.

PROTON BEAM
$4 > PT_{TRG} \geq 3$
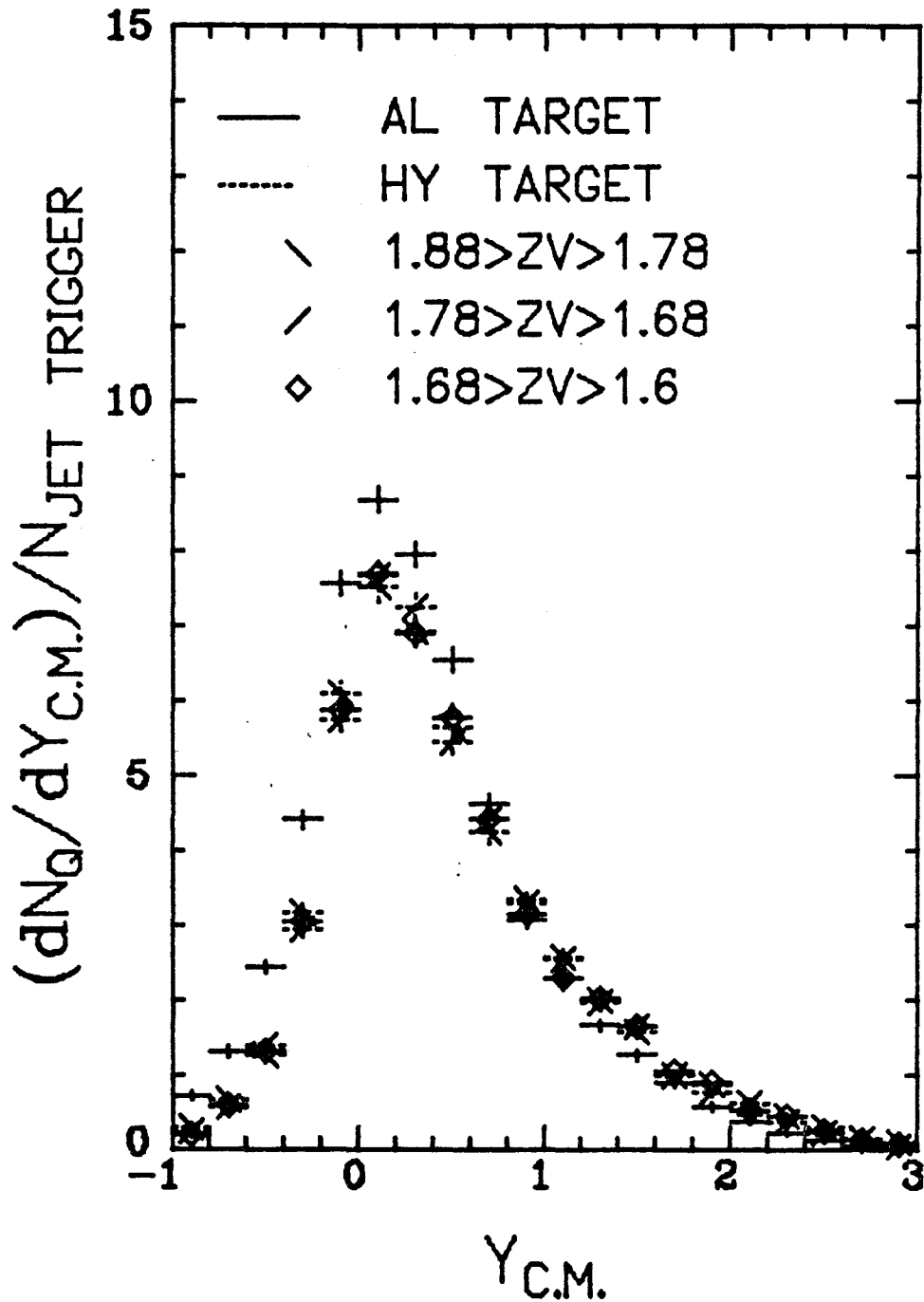
Figure 6.15a Proton beam; trigger jet $p_\perp$ between 3 and 4 Gev/c.

PROTON BEAM

$6.5 \geqq PT_{TRG} \geqq 4$
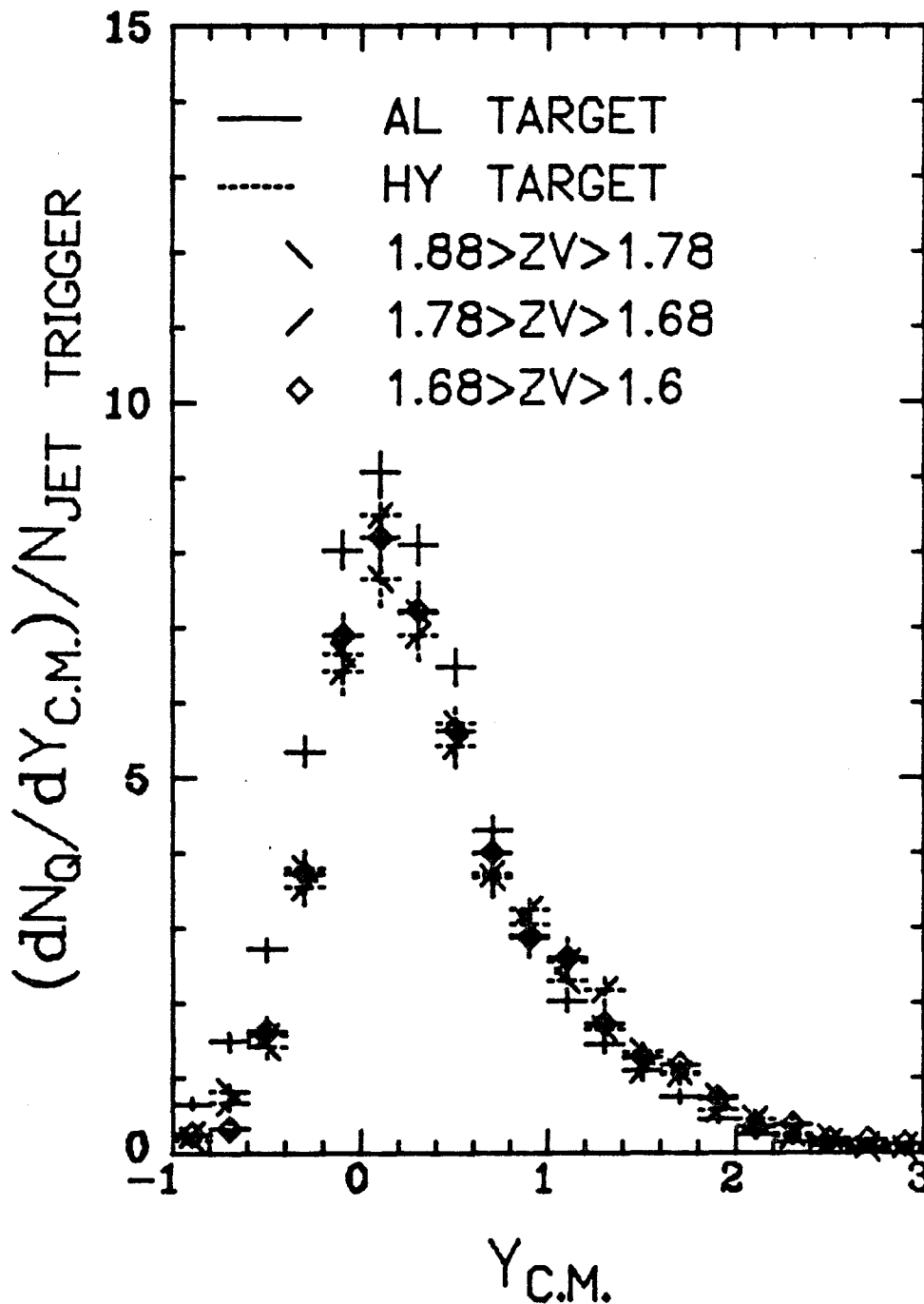
Figure 6.15b   Proton beam; trigger jet $P_\perp$

between 4 and 6.5 Gev/c.

π^- BEAM

$4 > PT_{TRG} \geqq 3$

Figure 6.15c π^- beam: trigger jet $p_\perp$ between 3 and 4 Gev/c.

π^- BEAM
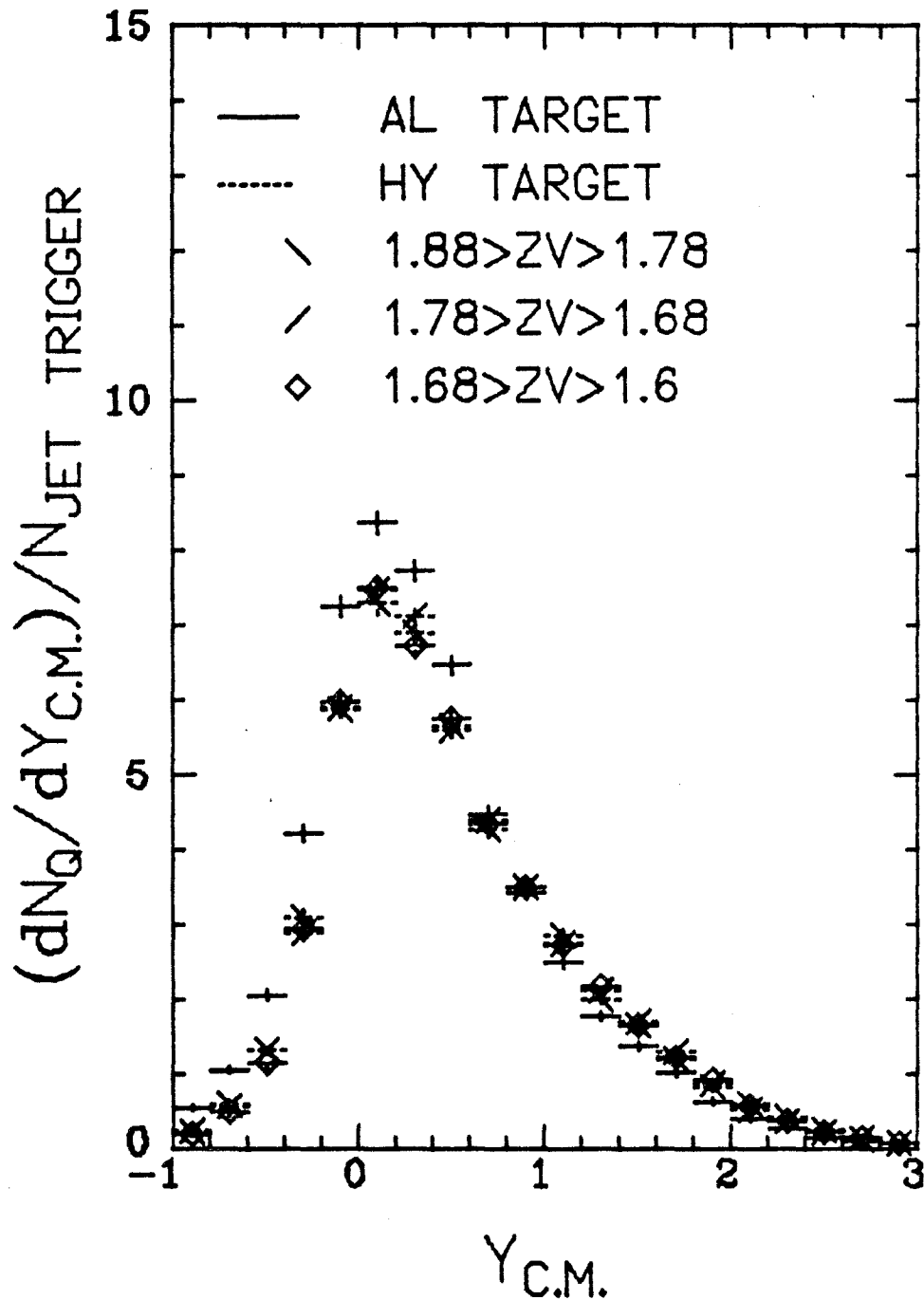
$6.5 \geq PT_{TRG} \geq 4$
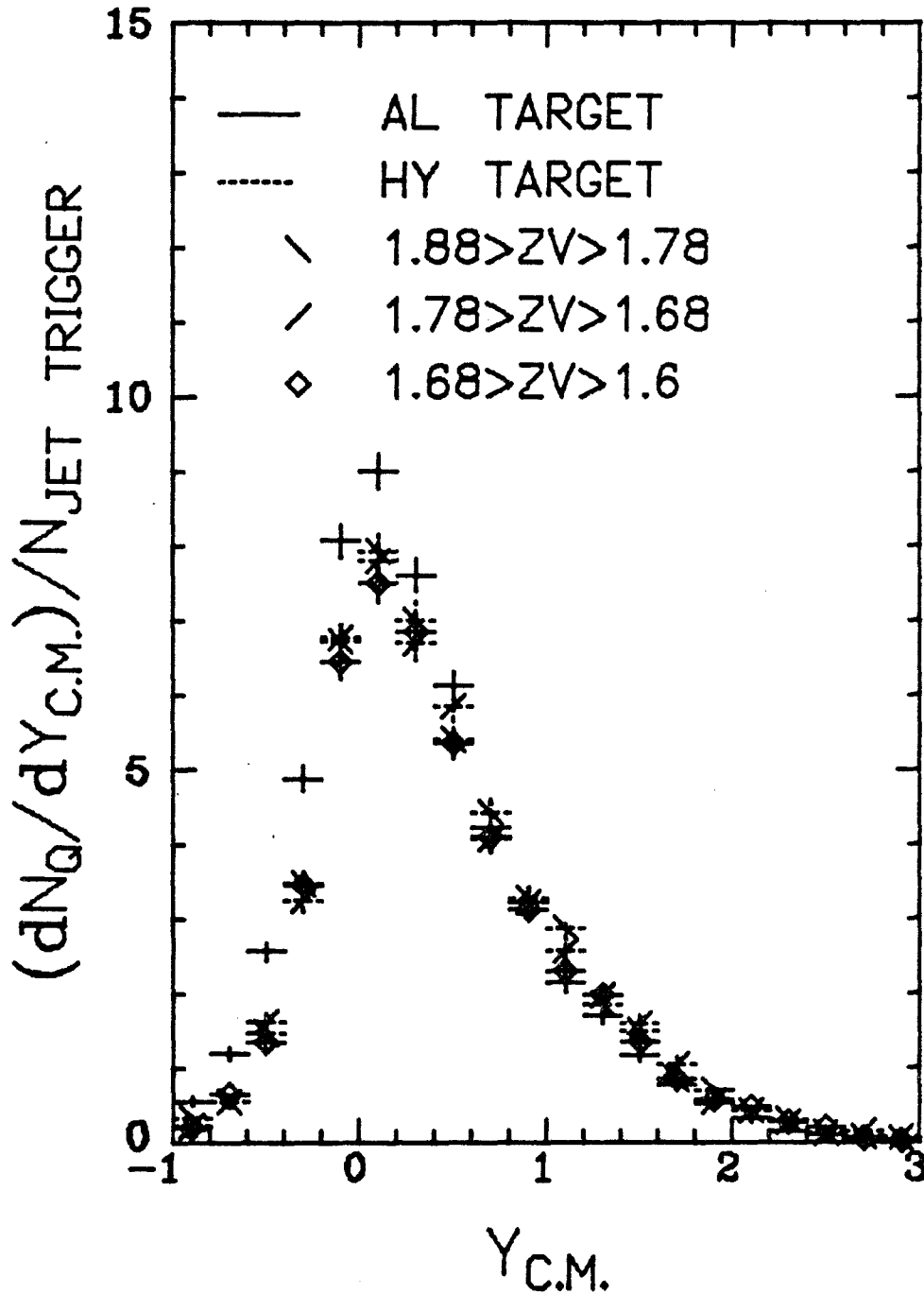
Figure 6.15d π^-beam; trigger jet $p_\perp$ between 4 and 6.5 Gev/c.

Figure 6.16 Ratio of D(Y) plots (aluminium

over hydrogen) for particles "outside the

2x2" and "affected by the 2x2" on the away

side for two different jet $p_\perp$ regions.
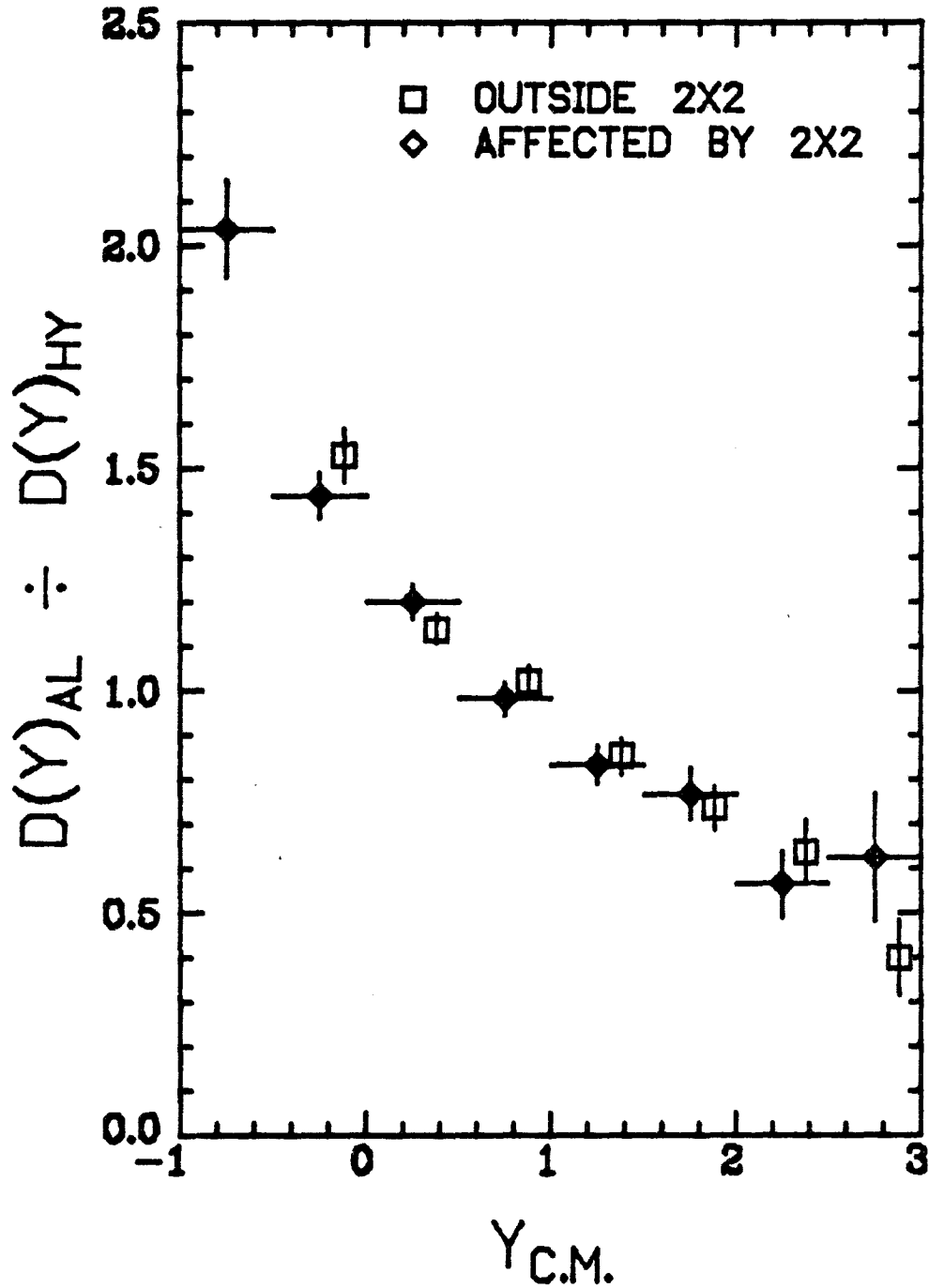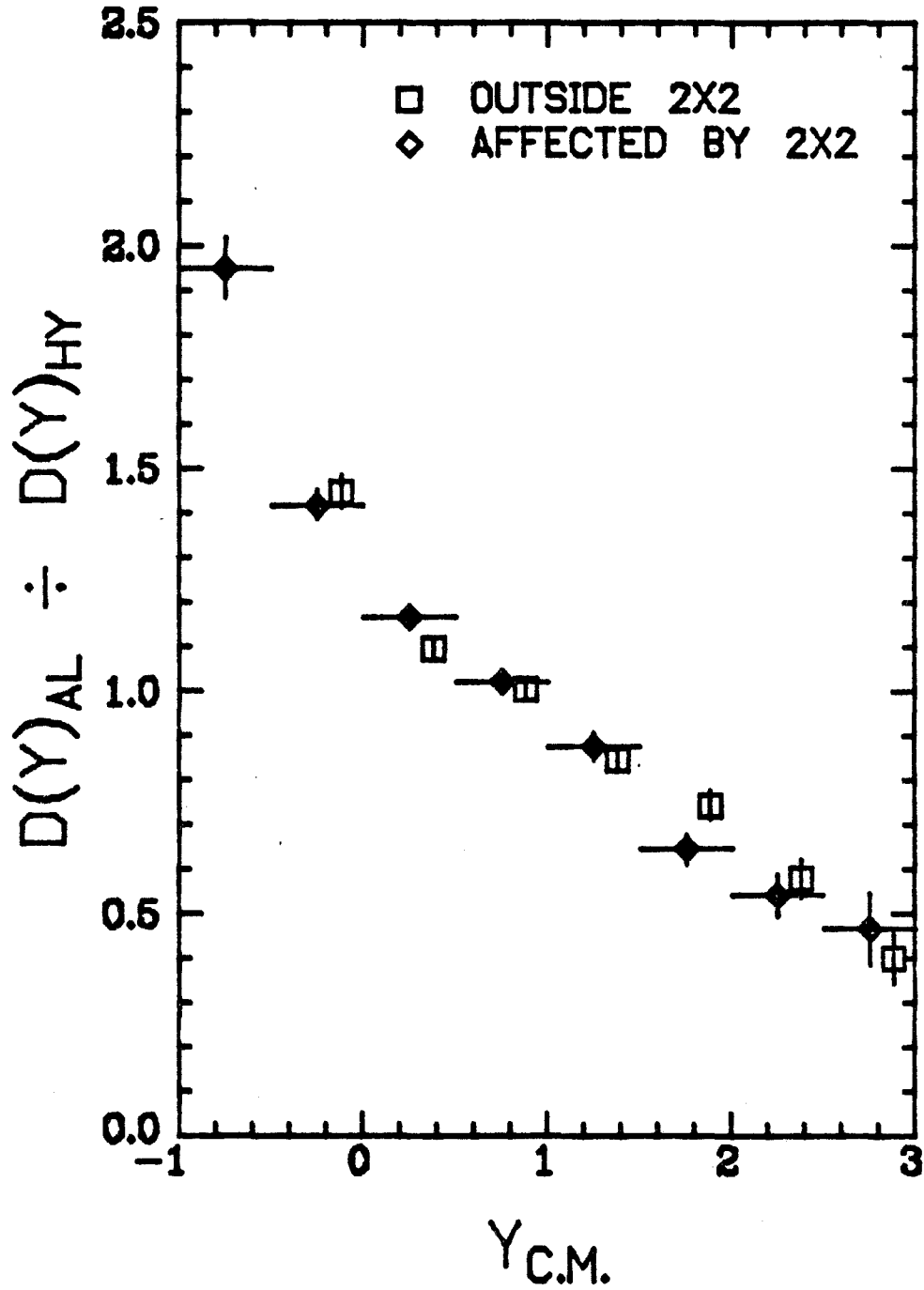
Figure 6.16a.

Figure 6.16b.

Z DISTRIBUTION OF ALL CHARGED PARTICLES ON THE AWAY SIDE
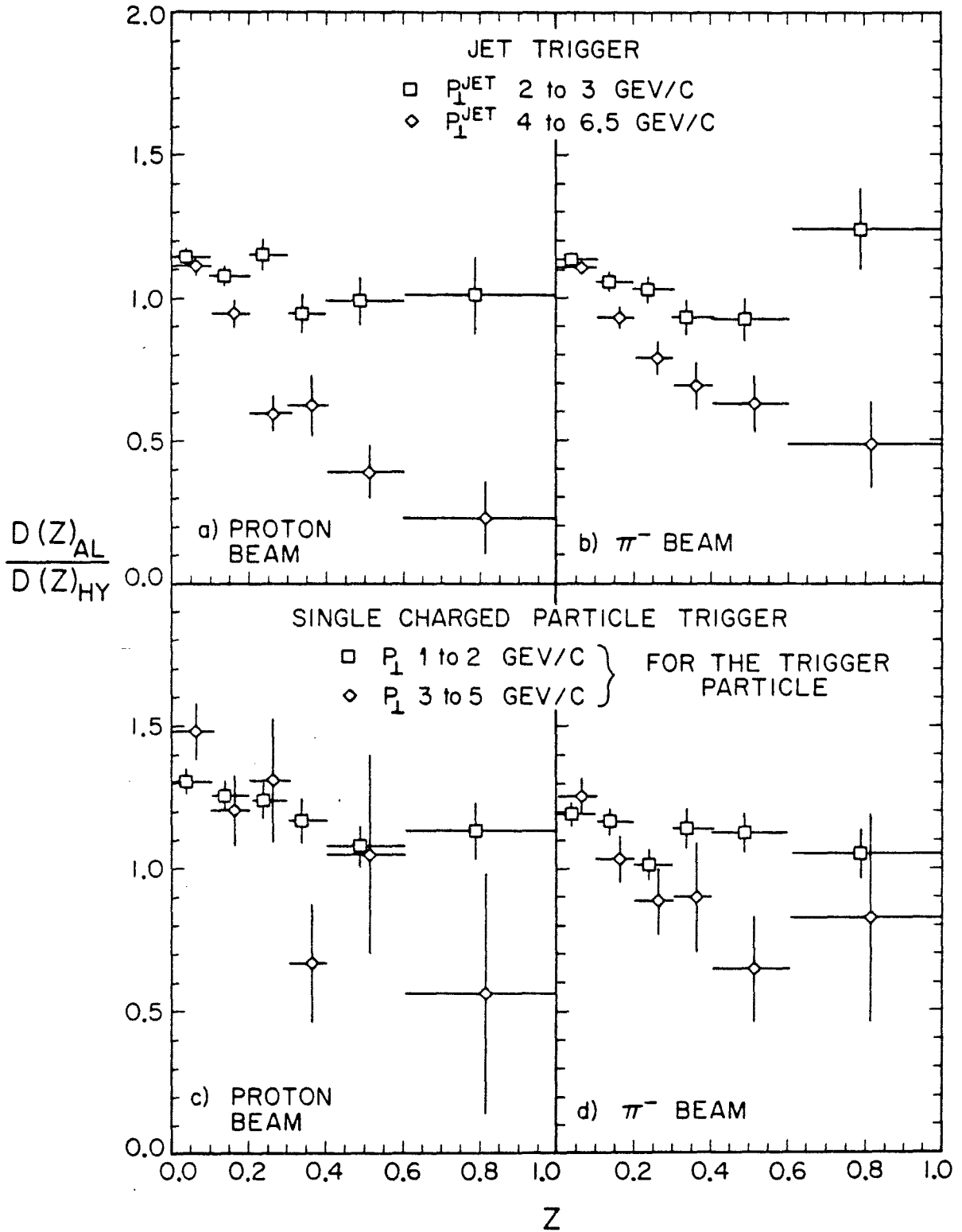
Figure 6.17   R(Z) distribution for particles on the away side.
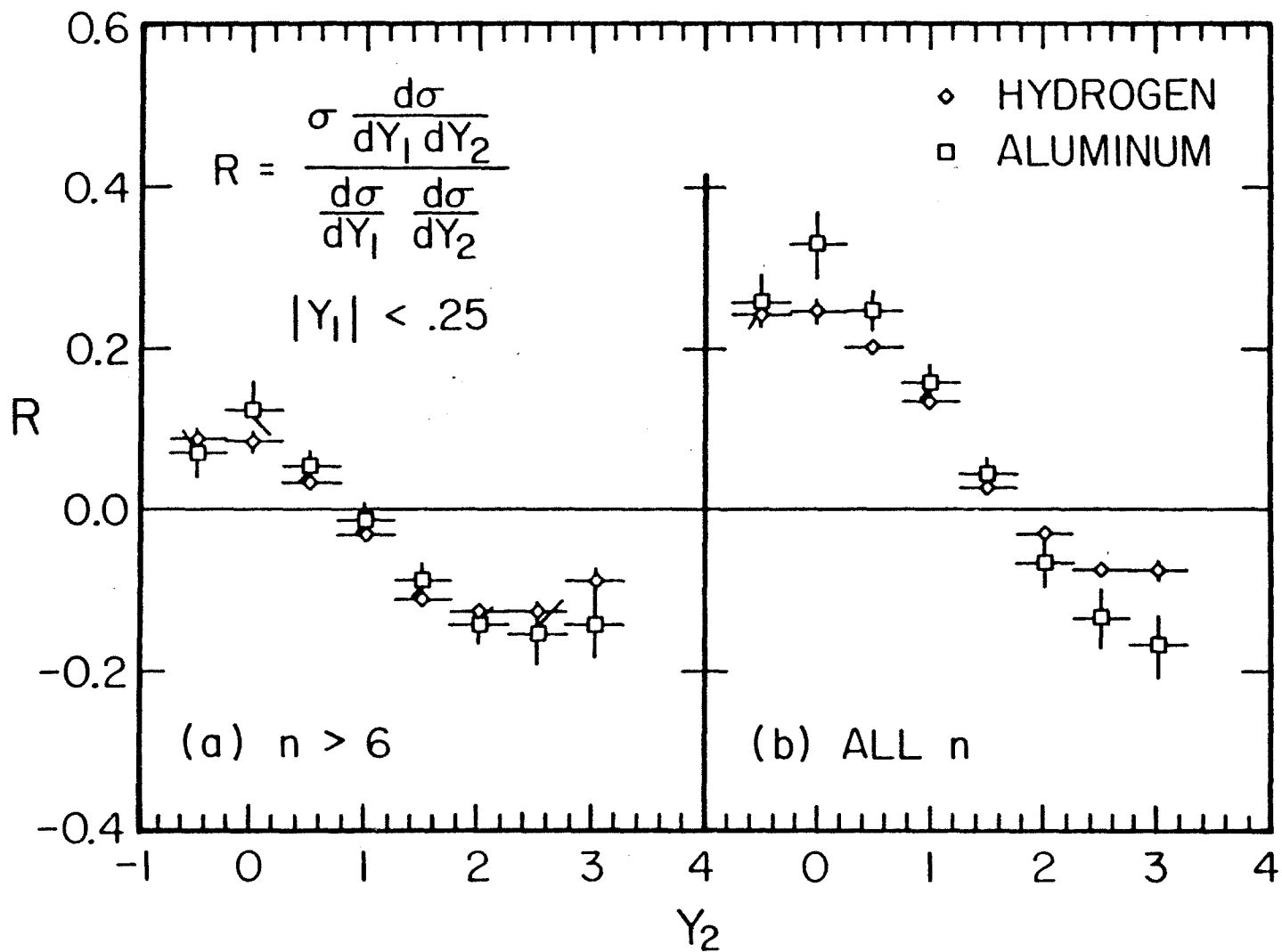
Figure 6.18   Correlation plots by Tse , see [6.17] for detail.

HIJET HYDROGEN
CHARGED PARTICLES IN JET
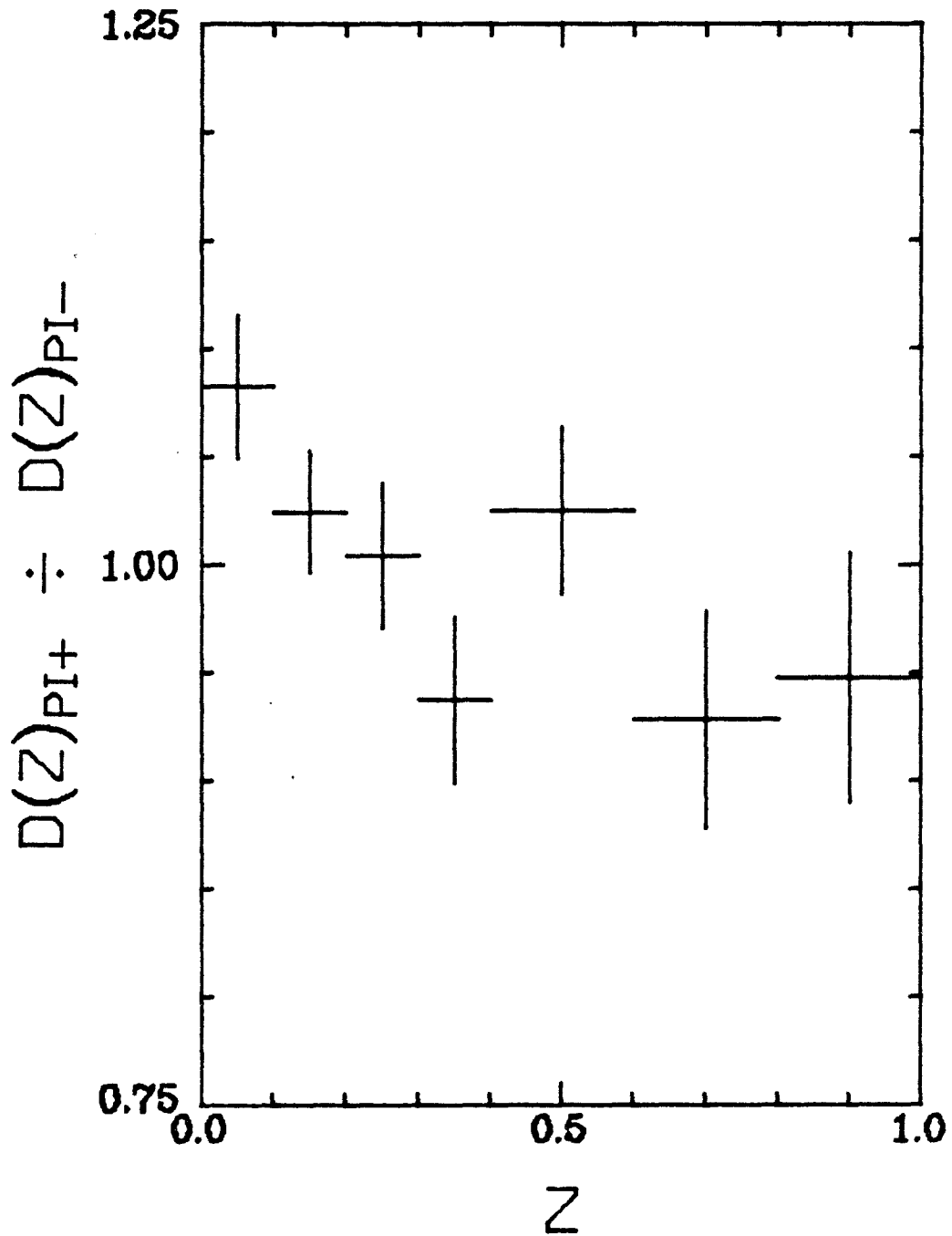
Figure 7.1a   Ratio of D(Ƶ) for particles in

the jet (π^+overπ^-, hydrogen target).

HIJET   ALUMINIUM
CHARGED PARTICLES IN JET
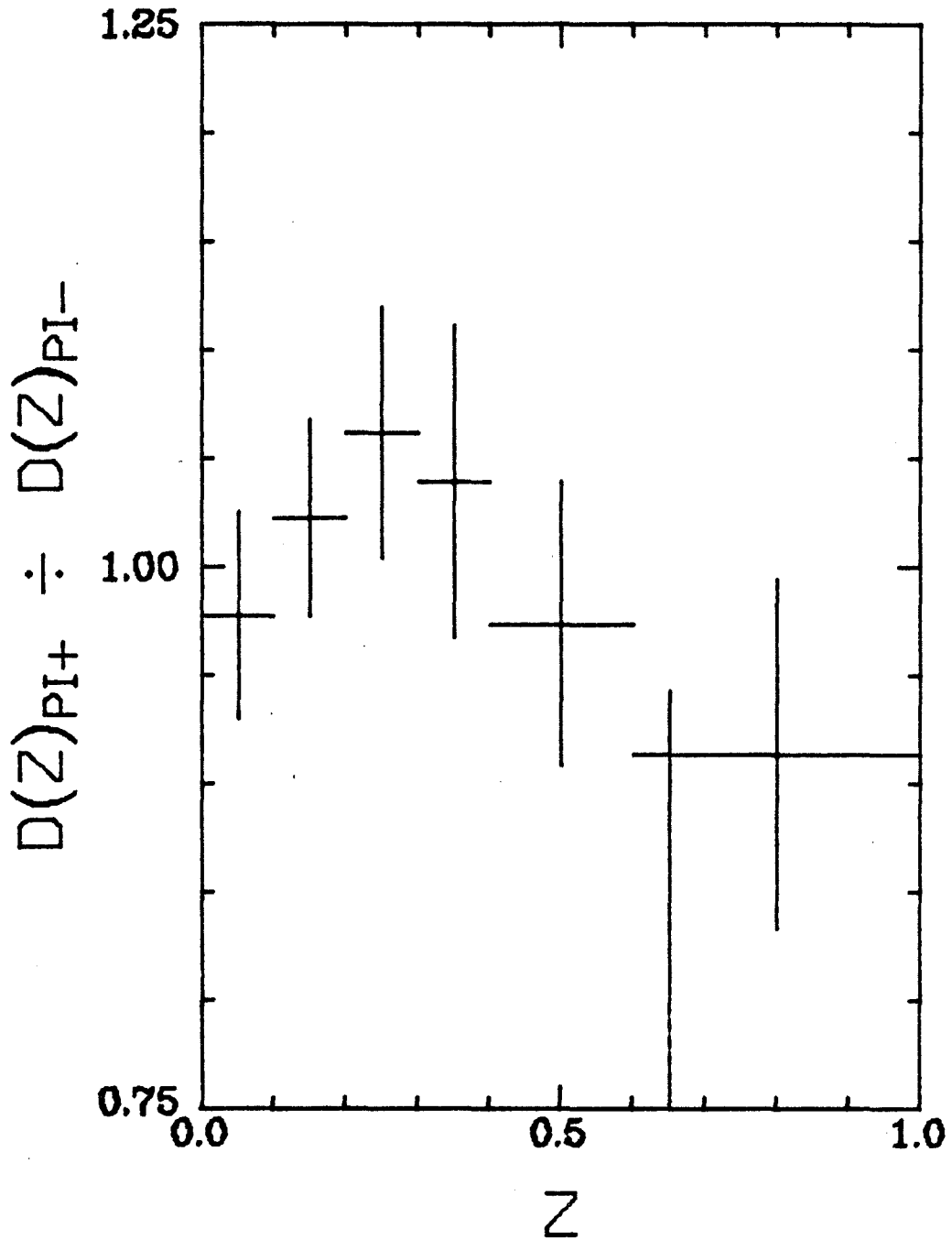
Figure 7.1b Ratio of D(Z) for particles in
the jet (π^+ over π^-, aluminium target).
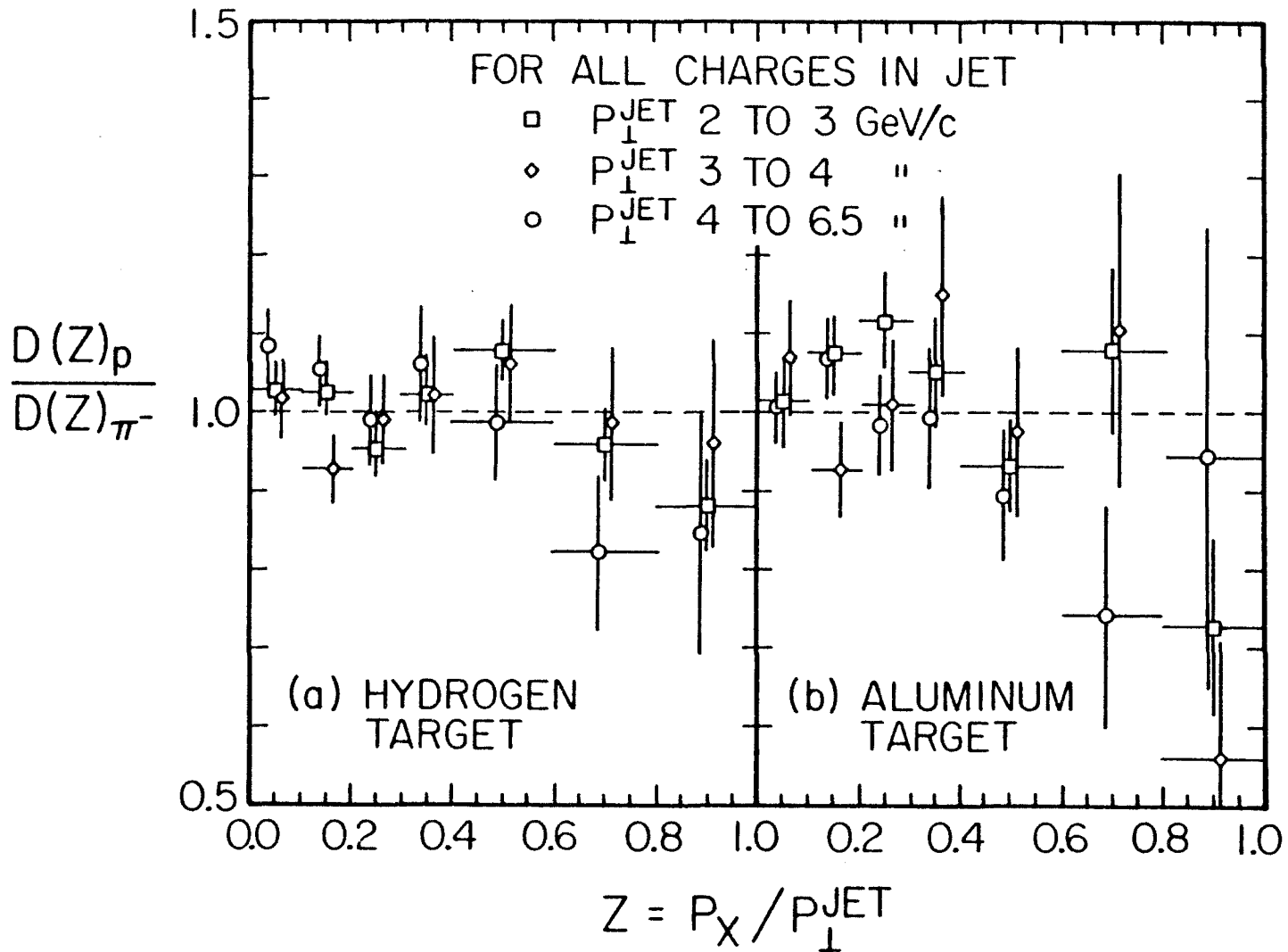
Figure 7.2 Ratio of D(Z) for particles in the jet (proton over π^-).
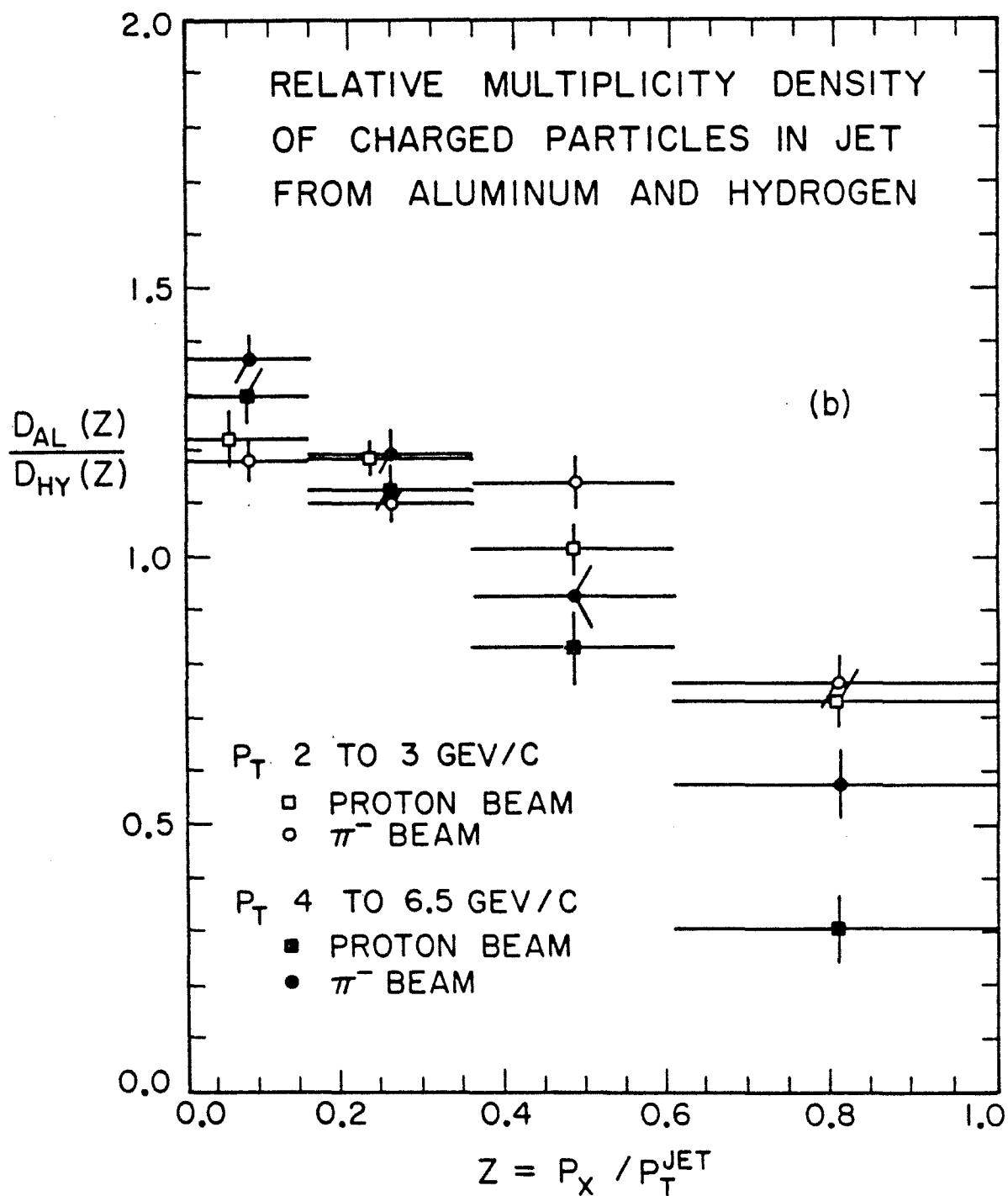
Figure 7.3   Ratio of D(%) distributions for

the aluminium target over the hydrogen target

D(%) is defined in the text.

Figure 7.4 & 7.5   Ratio of D($\&$Q) plots for
particles in the jet. The case "NO $\&$CUT"
means $\&$Q=$\&$. The definition of $\&$Q is defined
in section 7.2. The $\langle$ jet $P_\perp \rangle$ for these plots
are listed in Table 6.1.

HYDROGEN TARGET
HIJET
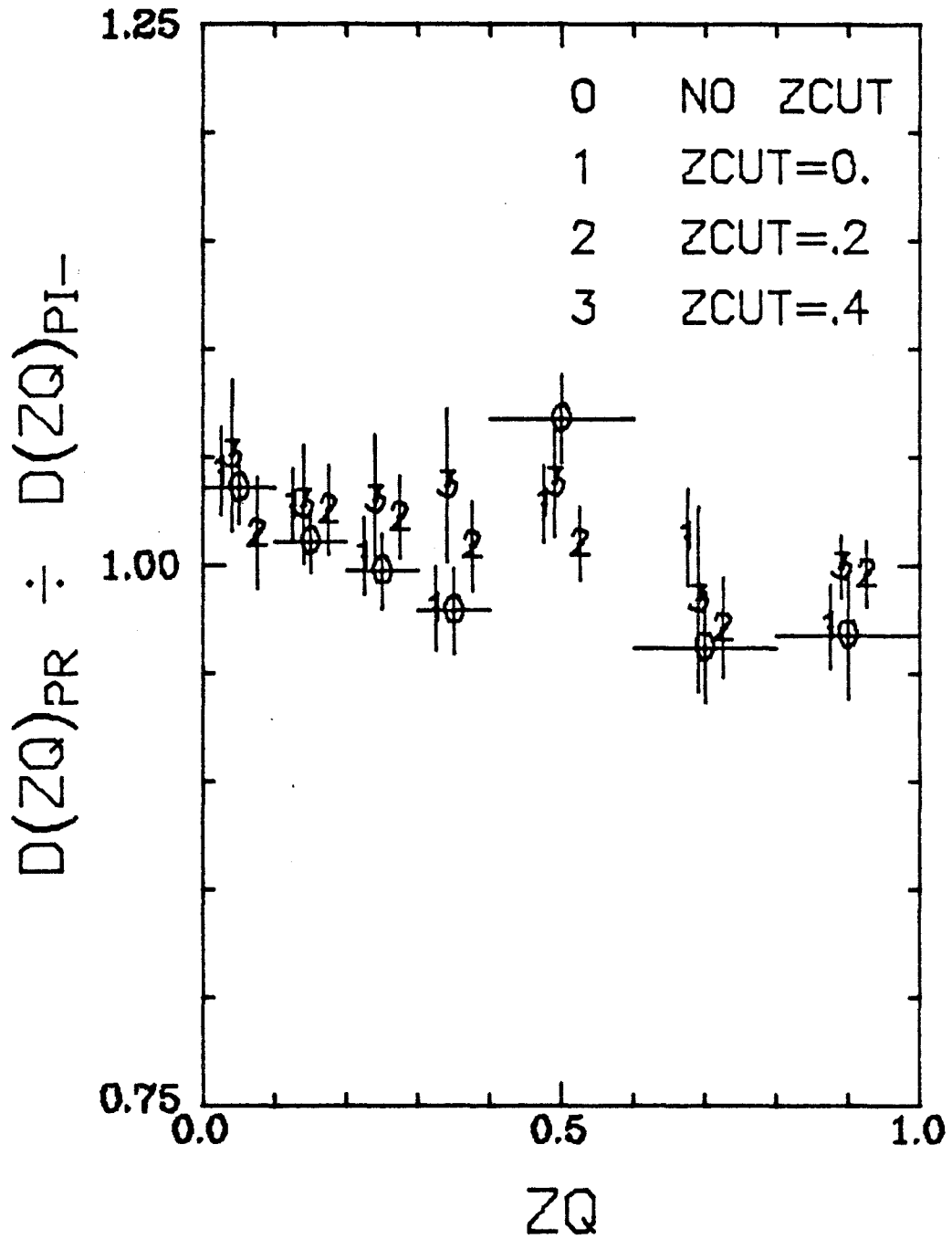
Figure 7.4a Proton over π^-, hydrogen target.

ALUMINIUM TARGET
HIJET
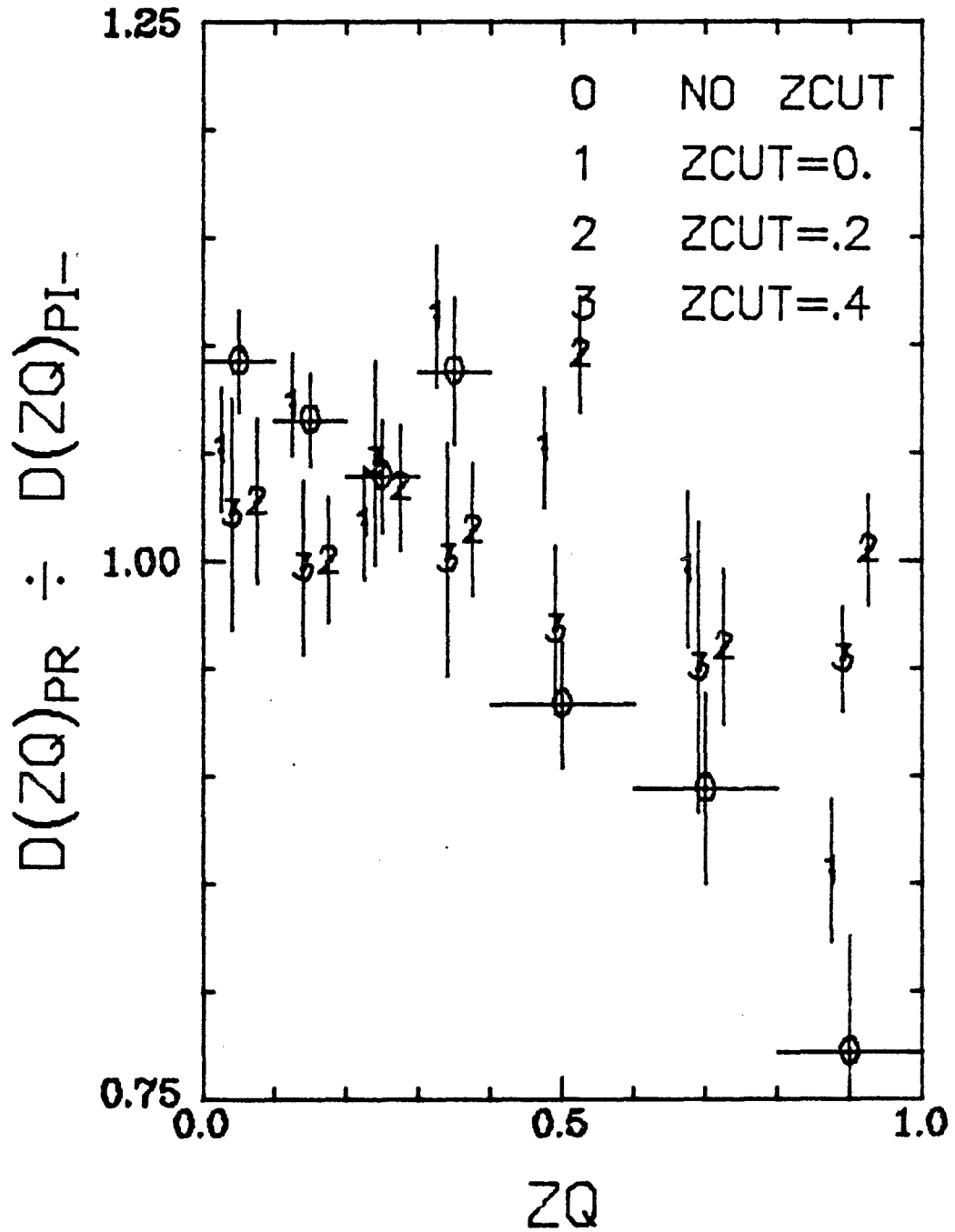
Figure 7.4b Proton over τ, aluminium target.
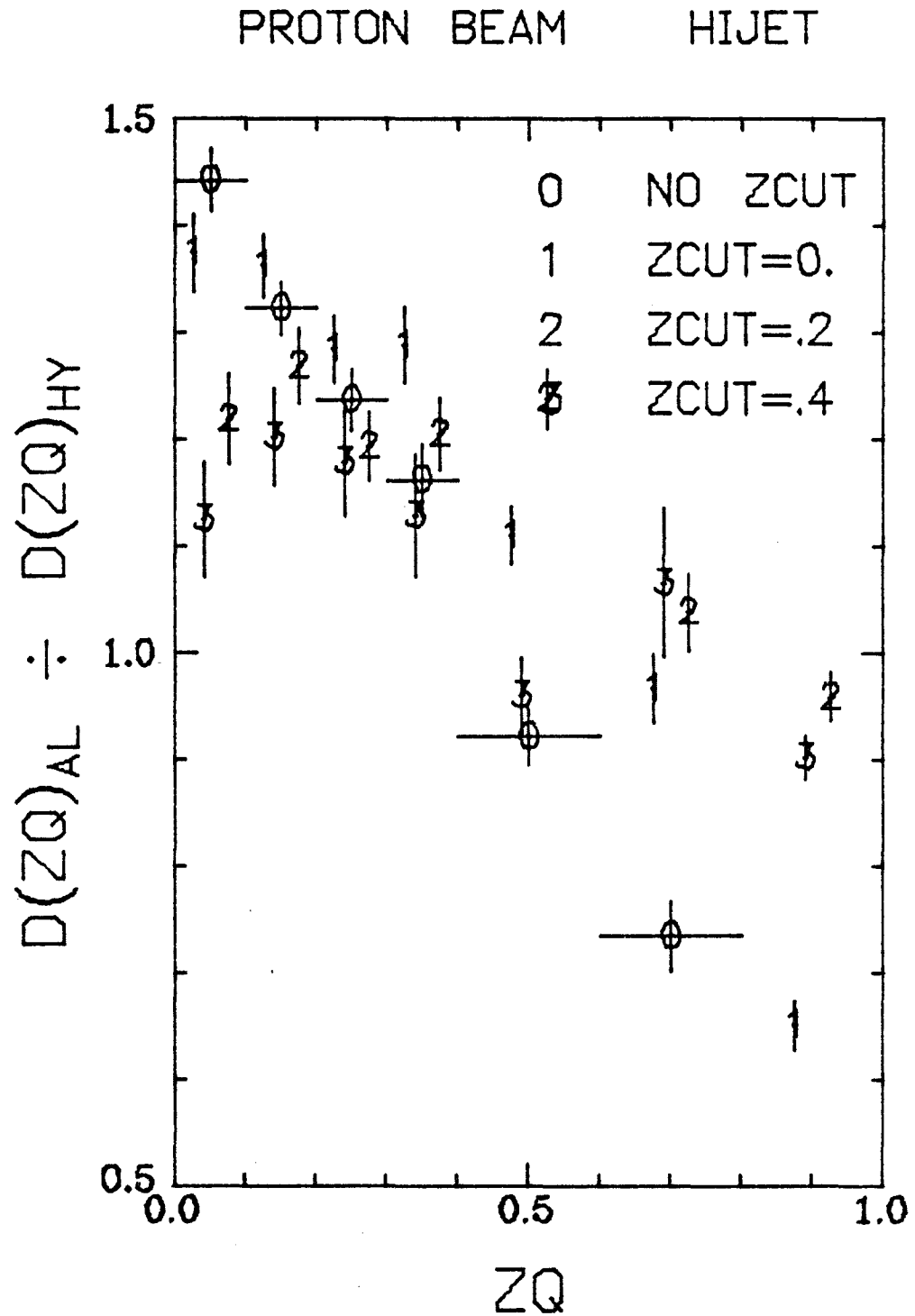
PROTON BEAM   HIJET

Figure 7.5a   Aluminium over hydrogen,

proton beam.

π^- BEAM   HIJET
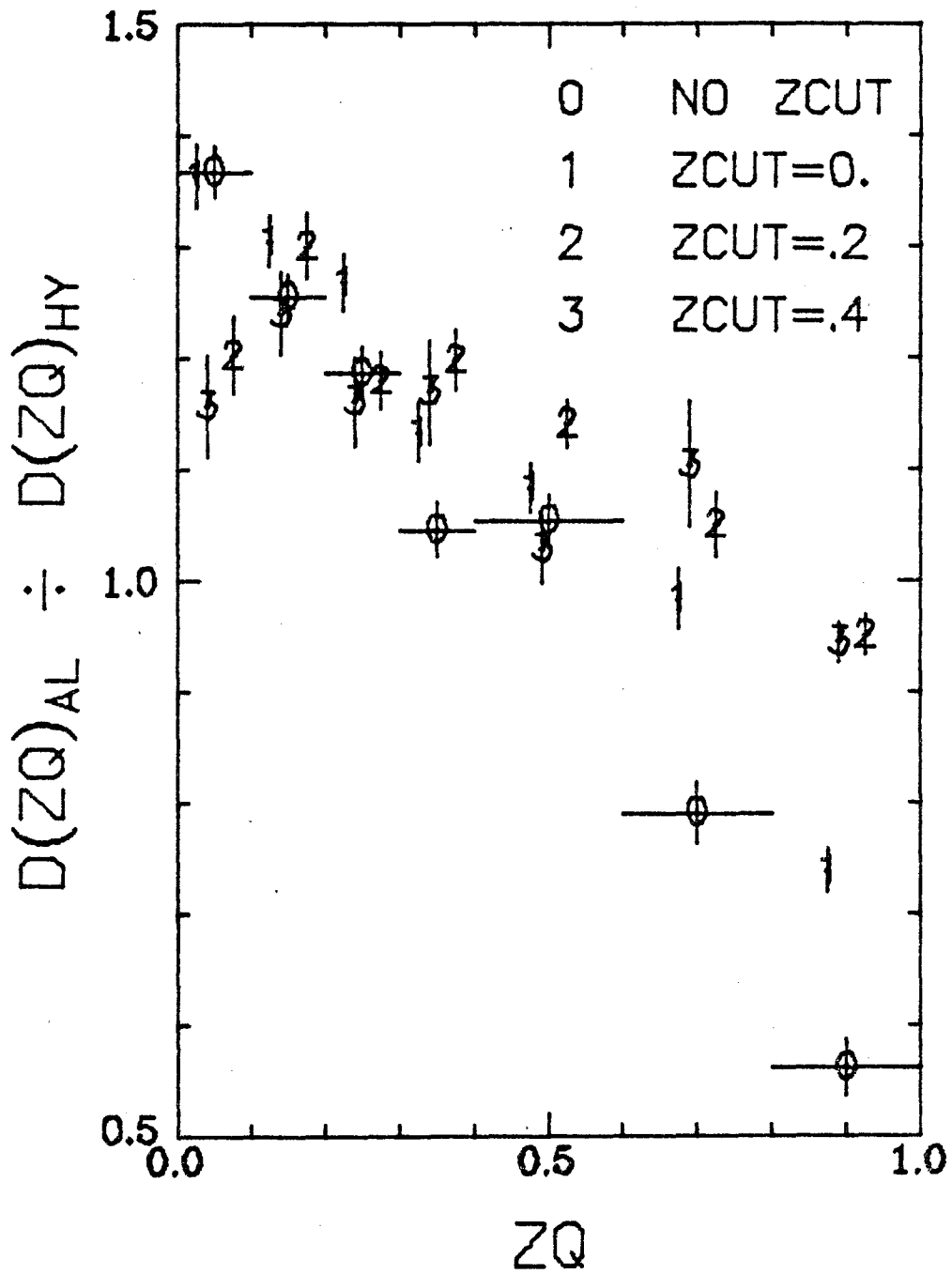
Figure 7.5b   Aluminium over hydrogen, π^- beam.